Development of a Multi-Channel Visible-Light Optical Coherence Tomography Platform for Investigating Fibrotic Disease Using Optical Scattering

By

Ryan C. Niemeier

A dissertation submitted in partial fulfillment of

the requirement for the degree of

Doctor of Philosophy

(Biomedical Engineering)

at the

UNIVERSITY OF WISCONSIN-MADISON

2020

Date of final oral examination: 07/22/2020

The dissertation is approved by the following member of the Final Oral Committee:

Jeremy Rogers, Assistant Professor, Biomedical Engineering

Paul Campagnola, Professor, Biomedical Engineering

Kevin Eliceiri, Professor, Biomedical Engineering

Kristyn Masters, Professor, Biomedical Engineering

Melissa Skala, Associate Professor, Biomedical Engineering

Nathan Sandbo, Associate Professor, Medicine

Abstract

Optical imaging and microscopy provide multi-dimensional information in both the laboratory and clinical settings. Novel imaging methods have leveraged several contrast sources in order to provide both qualitative and quantitative metrics. Optical coherence tomography (OCT) is a volumetric, micro-scale imaging modality which draws intrinsic contrast from the optical scattering of tissue. Visible-light OCT (VIS-OCT) increases the scattering contrast and is ideal for imaging thin layers of tissue with subtle changes to the optical scattering. The work contained in this dissertation is a modification of VIS-OCT to utilize simultaneous acquisition of multiple channels. Multi-channel VIS-OCT is capable of noise reduction, polarization sensitivity, and quantifying tissue optical scattering.

The multi-channel system was used in several imaging applications with relevance to translational medical care and bench-top research. The system was used to image the optical scattering changes in esophageal tissue before and after microwave ablation. Measurements of optical scattering helped to identify the boundaries of the ablation which can provide valuable information both during treatment and for microwave and radiofrequency ablation antenna design. By adding polarization channels, multi-channel VIS-OCT was capable of measuring birefringence in a mouse model of pulmonary fibrosis which is being used to test novel therapeutics for lung disease. Finally, a variation of this OCT system was developed to be used in a multi-modal system which combines and co-registers several other imaging modalities and is well-suited to study fibrosis in glaucoma and cancer. The sensitivity of this VIS-OCT system to optical scattering and polarization effects make it a valuable tool with which to study fibrosis. This dissertation describes the framework of this platform and several utilities which in future work will incorporate a lens-free probe for cost-effective *in vivo* imaging and other bench-top variations will enable higher resolution imaging capable of capturing dynamic processes in live cells.

Acknowledgments

"If I have seen further it is by standing on the shoulders of Giants." -Isaac Newton in a letter to Robert Hooke.

I have thought about these words often during graduate school. I am lucky to have had many Giants in during my time, several of a kind that I never expected. Prof. Jeremy Rogers has been a phenomenal mentor. His patience and willingness to teach a biochemist optics, coding, mathematics, and all manner of engineering are a testament to his dedication to mentoring and I could not be more thankful. Prof. Paul Campagnola for all of his feedback during lab meetings, his keen criticism and desire to cut directly the core of the matter have been an invaluable resource in both writing and how I conduct my work. Prof. Kevin Eliceiri and Prof. Melissa Skala for their willingness to collaborate and helping so much of our work flourish. Prof. Kristyn Masters for her dedication to keeping my work focused and providing a firm ground in the biological applications of my work. And finally Dr. Nathan Sandbo, for his enthusiasm in exploring all the potential avenues of our work together, despite the logistics of remote work towards the end.

I must also acknowledge the Giants that put me on the winding road that led me here. Prof. Craig Cady and Prof. Dean Campbell saw a curious student and gave me a chance to follow my curiosity and ignite a curiosity for research that persists today. Prof. Abhay Pandit and Dr. William Daly for giving me a wider perspective both in scientific research and my own life. Without my colleagues in the Rogers Lab and the Department of Biomedical Engineering, I definitely would neither have finished my degree, nor would I have so immensely enjoyed my time during graduate school.

Working at UW-Madison gave me the opportunity to work with several Giants and I am extremely grateful to those collaborators in several projects. Dr. Etöz conducted the ablation work in the Barrett's esophagus project and Daniel Gil performed the NIR-OCT imaging. Dr. Ksenija Bernau in the Sanbo group coordinated the animals in the lung study and organized a tremendous amount of data collection and analysis. Prof. Campagnola and his lab conducted the SHG microscopy imaging used throughout this dissertation, particularly in the lung study. Benjamin Robinson of the Campagnola and Rogers groups acquired the EBS data for the lung study. Dr. Michael Pinkert constructed the ultrasound and SHG microscopy of the multi-modal imaging

project. Dr. Pinkert and Dr. Bing Dai jointly developed the software and hardware integration of these modalities. Dr. Zach Simmons constructed the Enhanced Backscattering Spectroscopy and its integration. The work contributed by those mentioned here has been tremendously helpful and I cannot thank them enough.

Perhaps the most unexpected Giant was my friends and my family. I count myself beyond fortunate to have enjoyed the friendship and support of so many people: Aleksey (as well as his parents, Brent and Lana), Ben, Dr. Chloe, Eric, Evan, Jamie, Jeff, Kelsey, Matt, Pierre, Quincy, and too many others to mention here. My parents, Robert and Janelle, who have supported me every step, even if it didn't seem like the right one. My siblings, Jennifer and Robert, along with their spouses, Gordon and Joy, who have always motivated me and helped me to achieve more. My mother-in-law and father-in-law, Servet and Hasan, who always encouraged and supported me since the day we met. My nephews, Henry and Noah, who displayed no hesitation whatsoever in dictating that LEGOs were more important than anything I was working on. My family who are too numerous and competitive to list in any order here (see unlisted appendix).

Finally, I thank my wife: Sevde. Without her, I would surely not stand even half as tall as I do now. She has been my constant support during late nights of work and writing, the one who has motivated and pushed me to accomplish so many things, the light of my life, and my Giant. Thanks to you, I have seen so much.

Funding Sources

There are several funding sources which contributed to the work in this dissertation. I would like to take this opportunity to thank the following:

Retina Research Foundation Edwin and Dorothy Gamewell Professorship

NSF Grant 1240416 EFRI-BioFlex: Miniature, low-cost fiber-optics technology for measurement of tissue structure at sub-diffractional length scales: a platform for cancer screening

NSF Grant 1429045 MRI: Development of Multiscale Imaging Platform for Quantitative Analysis of Collagen Organization

NSF Grant 1845801 CAREER: Dynamic phase-sensitive optical coherenence microscopy to quantify activity in retinal cells

NIH Grant R01CA183101 Biophotonics to Couple Pancreatic with Upper GI Screening via Ultrathin Endoscopy

NIH Grant U01EY025477 Platform Technologies for Microscopic Retinal Imaging: Development & Translation

NIH Grant R21EB025513 Enhanced backscattering instrument for assessing optical biomarkers of glaucoma

Falk Medical Research Trust Catalyst Award: Targeting the Myofibroblast Epigenome for First-In-Class Treatment of Chronic Obstructive Pulmonary Disease, COPD

Contents

List of Figures

List of Tables

1 Introduction

The role of fibrosis and changes in the extracellular matrix (ECM) of tissue during disease development has become an area of increasing interest. Diseases such as cancer, glaucoma, idiopathic pulmonary fibrosis, and even the wound healing process are all hypothesized to be impacted by the ECM architecture and composition. Imaging technologies have advanced significantly in recent years to provide new and exciting opportunities in both the clinical and research settings. Physicians have cutting-edge optical imaging tools that are non-invasive, high-resolution, and capable of new contrast modalities. These modalities are capable of extraordinary data collection without the need for biopsy and can provide relevant diagnostic data in real-time. At the boundary of the research and clinic, these tools are being optimized to provide risk-stratification and classify high-risk patients before disease onset. The development of these optical methods in the laboratory has aimed to not only to diagnose disease but to also elucidate the mechanisms and biological processes in diseases.

Biological optical microscopy relating to disease has improved dramatically from histology stains and brightfield imaging of cells in a glass dish. The advents of fluorescent labeling, tunable and broadband lasers, high-speed electronics, high-sensitivity detectors, and computer technology have driven advances in the field to leverage several different physical phenomena as sources of contrast. Many physical phenomena such as autofluorescence and scattering form the basis of intrinsic contrast due to how the physical structure of tissue affects its innate optical properties. Utilizing these properties for contrast has allowed for the development of optical tools that are minimally invasive and minimally harmful but maximally impactful on the patient or sample. Rather than taking one or more biopsies, injecting a contrast agent, or designing cellular and animal experiments around time-point sacrifices or fixations, scientists can generate image data with high-throughput and minimal invasiveness.

Of particular interest is Optical Coherence Tomography (OCT), an interference-based imaging method which scans a lateral surface and produces volumetric images in depth. Similar to ultrasound, but on the micro-scale, OCT produces tomographic slices similar to histology without the need for tissue biopsy, sectioning, and staining. The optical design of OCT allows it to be operated as a scanning microscope, as is often used in the research setting, or incorporated into a rotary

endoscope or catheter for clinical use. Image contrast in OCT is based on the optical scattering of the tissue and is thus highly sensitive to changes in tissue architecture. First used to image the retina in the early 1990s, the clinical potential of OCT was quickly realized in both ophthalmology and in endoscopy where it is used to image the esophagus, atrial walls, trachea, and in the GI tract.

Due to the contrast of OCT images being dependent on optical scattering, image quantification and deliberate instrument design has allowed for new modalities for quantitative imaging. Polarization-based detection and control holds a great deal of potential in studying the ECM, particularly collagen. The ability of polarization-sensitive OCT (PS-OCT) to detect tissue birefringence and optical axis orientation has been applied to burn wounds, coronary plaques, and the anterior portion of the eye. These methods and techniques currently form the forefront of OCT research and hold great promise in clinical settings. Furthermore, when used in laboratory environments, these systems can be optimized to study bench-top models such as cell cultures, animal models, and excised tissue. The non-invasive nature of OCT allows for these studies to be run longitudinally with minimal impact on the subject. Not only does this hold ethical benefits, but the reduction of variability, high data volumes, and the maximization of the impact of each sample in a study are ideal.

To contribute to this expanding field, this dissertation describes the design, construction, and iteration of a visible-light OCT (VIS-OCT) system to study fibrotic disease. This system is demonstrated to be sensitive to optical scattering and incorporates a novel multi-channel detection scheme capable of noise reduction and adding polarization sensitivity. The work explores the use of visible light laser sources to maximize scattering contrast and explores the utility of a portable, cost-effective source. The multi-channel detection is used for a novel noise reduction technique that may potentially improve all supercontinuum light sources and the detection scheme is adapted for polarization-sensitive measurements. Finally, the use of this platform is assessed in biological applications for the esophagus, lung, and eye are investigated. In each of these, the change is tissue structure is visualized by the changes in optical scattering properties and correlated to other established methods.

2 Background

2.1 Fibrotic Disease

The extracellular matrix (ECM) is a vast meshwork of proteins and polysaccharide chains that provide the structure and support a plethora of for the cells of the human body [1]. In addition to providing physical structural support [2], the ECM can induce cell signaling by sequestering growth factors [3] and by mechanical transduction [4]. These signaling processes can control cell motility [5, 6], proliferation [6], and differentiation [7, 8]. These mechanical signal transductions have recently become widely studied for their hypothesized roles in several diseases [9, 10, 11]. The increase in ECM deposition is commonly referred to as fibrosis and results in the accumulation of connective ECM in a particular site such as injury.

The main structural component of the ECM is protein, specifically collagen [1]. While several forms of collagen exist, fibrillar collagens (type I-IV) are the most common form and accounts for up to 90% of the total ECM protein [12], and collagens as a whole represent approximately 25% of the total protein mass in mammals [1]. Collagen I is a fibrous protein consisting of repeating Gly-X-Y where X and Y are typically proline or hydroxyproline [12]. This repeating unit forms α-chains form with a left-handed orientation, as opposed to the typical right-handed α-helix [1, 13]. Three of these left-handed helices, called protocollagen strands, will form a right-handed triple helix to form a procollagen triple helix [13]. Procollagen N- and C-proteinases cleave the N and C terminus collagen propeptides directed the left-handed helix formation of the initial protocollagen strands, forming the tropocollagen triple helix [13]. The tropocollagens will then sef-assemble into a collagen fibril, which is crosslinked by lysyl oxidase to form the collagen fiber [13]. Collagen is typically produced by fibroblasts [12] which along with macrophages also play significant roles in its remodeling [14, 15]. The activity of these cells is regulated by several complex mechanisms and signaling pathways, several of which are activated during wound healing and various diseases [16, 17, 18].

The ECM and collagen in particular are constantly modified and remodeled in normal tissue function [19], but several diseases misregulate the process and lead to increased deposition or changes in structure [20, 21]. Diseases such as cancer [21, 22, 23, 24], idiopathic pulmonary fibrosis [25, 26, 27], and glaucoma [28, 29] all feature this activity. In these three cases, collagen remodeling has been demonstrated using second harmonic generation (SHG) microscopy [30, 31, 32],

a highly-sensitive micro-scale imaging method that can selectively image collagen directly [33]. However, the clinical translation of SHG presents significant challenges [34]. Collagen type I has been found to be of particular interest in these diseases both due to its significant role in disease progression and its potential as a biomarker using SHG microscopy [30, 33].

Collagen type I has recently been the subject of intense study from Eliceiri [35, 36], Campagnola [37, 30], and Keely [35, 36] for its structural change in cancer and at tumor boundary margins. The work of several groups have noted the ability of collagen fiber alignment and density in cell migration and proliferation [36]. The collagen organization at the tumor boundary has been shown to be a predictor of primary tumor cell metastasis and has been referred to as the tumor associated collagen signal (TACS) [36, 38, 39].

Similarly, increase in collagen content in idiopathic pulmonary fibrosis (IPF), a scarring condition of the lung, has also looked at collagen as a potential biomarker for prediction [25, 26, 27]. The fibrosis process leads to increased collagen deposition and decreased lung function [27]. Work from Brasier [40] and Sandbo [41] has explored the mechanisms of IPF and developed animal models in order to better understand disease progression, potential diagnostic biomarkers, and treatment strategies. The pathway of fibrosis generally involves fibroblast recruitment and increased macrophage activity which results in increased fibrotic tissue deposition [27, 41]. Diagnosis for IPF remains challenging since the most specific disease markers require invasive testing, such as hydroxyproline quantification in biopsy tissue, and less invasive routes, such as CT imaging, lack the specificity for diagnosis.

Finally, in glaucomatous disease changes in the intraocular pressure (IOP) contribute to the death of retinal ganglion cells (RGCs) and damage to the optic nerve, resulting in vision loss [42]. The increase and decrease in IOP has recently been correlated to changes in collagen architecture of the sclera, such as an increase in collagen density when IOP is elevated [43, 42]. While it is currently unclear whether the relationship is causal, or indeed which change is causal to which symptom, the association is present. A single point mutation of LTBP2 generates a model of glaucoma in felines has been developed by McLellan which allows the disease progression to be studied in a powerful animal model [44].

In the case of each of these fibrotic diseases, SHG microscopy has been a powerful contributor [30, 31, 32]. Collagen type I is non-centrosymmetric, meaning that it possesses a second-order

hyperpolarizability [33]. This allows collagen to absorb two photons and emit a single photon in a non-fluorescent process which is second harmonic generation. The resulting photon out is double the frequency and half the wavelength. The SHG NIR absorption band for collagen makes this a powerful tool for microscopy, as it can be tuned to illicit minimal autofluorescence [45] and can be adapted into a scanning two-photon microscope [33]. Due to the wavelength ranges involved, the need for high NA to provide sufficient focus for the multiphoton absorption, and the long image acquisition time needed for high SNR, SHG microscopy is difficult to translate into a scanning endoscopy method, but is feasible and remains an active area of research [46, 34]. It remains, however, an incredibly useful tool for bench-top research and provides valuable insight into collagen architecture.

The increase in collagen deposition in fibrotic diseases has been studied with SHG microscopy and revealed key points which may impact optical properties [47]. The first is that the increase in collagen density may increase the optical scattering due to the index contrast between fibers and the surrounding matrix [48]. The second is that the accumulation of birefringence due to the increased collagen density, particularly when the fibers are well-aligned. Collagen is a naturally birefringent material and the fiber formation leads to large form birefringence that only increases in tissue as the alignment of the fibers increase [49, 50]. Both of these properties offer the potential for a more endoscope-ready imaging method to be used to investigate these biomarkers. This method will require sensitivity to optical scattering, birefringence detection, the ability to be adapted to an endoscope, capable of imaging at the appropriate resolution and size scale for these diseases, and have an acceptable data throughput to investigate large tissue fields.

2.2 Optical Properties of Tissue

2.2.1 Optical Scattering

Optical scattering properties of tissue offer a more accessible metric for diagnosis and are altered by changes in collagen structure [48]. Optical scattering arises from discontinuities in tissue refractive index and composition [51, 52]. The heterogeneous structure of tissue leads to significant intrinsic optical scattering as can be readily observed in opaque tissue [53]. Changes in tissue structure, such as the remodeling of ECM or chromosome packing, can lead to substantial changes in optical

scattering, which has been investigated as a potential marker for disease progression [54].

In the simplest case, scattering can be described by a sphere of uniform refractive index contained within a media of differing refractive index. A plane wavefront of light traveling through the media will have an interaction with the oscillating electric dipole of the material of the sphere, or scatterer. The result of this interaction is a re-radiation or scattering of the light, which depends on the cross-sectional area of the scatterer, the difference in refractive index between the media and scatterer, and the wavelength and polarization of the incident light [51, 52].

The light scattered by this particle will have a change in phase (ϕ) and direction (θ, φ) relative to the incident wave-front [52]. The direction of scattering is based on the ratio of the cross-sectional area of the scatterer to the wavelength of the incident light [52]. For cross-sections much smaller than the wavelength, the familiar Rayleigh scattering is observed wherein the re-radiation of light is roughly equal in all directions θ and φ, this is sometimes called isotropic scattering. As particle cross-section increases to approximately the wavelength, Mie scattering becomes dominant with more forward-directed angles. As cross-sections become much larger, the surface of interaction becomes homogeneous again and instead of scattering, refraction occurs.

The direction and total occurrence of scattering are key points to understand and can be explored by various models. While a full exploration of these models is outside of this work, two brief conceptualizations may be offered. The first considers the incident light as a single photon traveling through stationary media and interacting with a scattering particle. The photon will interact with and scatter from the particle in some direction that is probabilistic based on the size relationships described previously. The probability that the photon scatters at some angle θ is described by the scattering phase function $p(\theta)$ of the particle for a given wavelength, which is not a description of the phase of the light wave. The scattering phase function can be modeled in several ways for a given particle cross-section (Henyey-Greenstein, Rayleigh-Gans-Debye) [52]. Another perspective for this phenomenon is to instead conceptualize the incident light as a plane wave which diffracts from the scatterer via the Huygens-Fresnel principle. Every re-radiating spherical wavefront can be integrated which will result in the scattering phase function $p(\theta)$. The distribution of $p(\theta)$ is well-described by the anisotropy, g see Eq. 1, which approaches 1 as scattering becomes completely forward directed and approaches 0 as scattering becomes uniform in all direction as in Rayleigh scattering [51]. Finally, the totally occurrence of scattering must be addressed. In the simple

case of spherical particles suspended in a medium, the total scattering that will occur is the total scattering cross section within the volume. This is expressed as the scattering coefficient μ_s with units of inverse length. Given a random distribution of particles in a medium, the average distance light travels before a scattering event, the mean free path, is denoted by l_s and is conveniently equal to μ_s^{-1} [51, 52].

$$g =< cos(\theta) > \tag{1}$$

Scattering in tissue takes on a much more complex form [53]. Rather than conceptualizing the process as discrete particles in a homogeneous medium, scattering can best be described using a continuous medium with variable refractive index [55]. The refractive index of the medium can be described as a function of spatial dimensions. The correlation of this function is the Fourier transform of the spectral density in the Born approximation. The spectral density is related to the differential scattering cross section per unit volume. This can be used to derive scattering properties of tissue and describe the tissue structure [53]. Critically, the ability of scattering to describe tissue and provide information on a variety of length scales makes it an attractive source of contrast, if it can be imaged reliably.

2.2.2 Polarization of Light

Optical polarization is a broad topic which has utility in several fields. Comprehensive treatments of its mathematics and physics can be found in several sources, this manuscript will restrict its treatment to a brief explanation of notation and the necessary components to assess tissue birefringence and is taken largely from text by Born and Wolf [56] and De Boer, Hitzenberger, and Yasuno [57]. The polarization of light is described by the vector decomposition of a wave into its orthogonal components, typically referred to as *horizontal* (H) and *vertical* (V) or x and y respectively.

Light polarization can be expressed using two main conventions. Both forms attempt to describe the complex electric field $E(z,t)$ of a light wave (see Eq. 2) where A is the amplitude and ϕ is the phase of the wave. A complete description of polarization can be achieved with four variables: $|E_x|$, $|E_y|$, ϕ_x, and ϕ_y. In this equation, angular frequency is expressed by $\omega = 2\pi c/\lambda$ and wavenumber

by $k = \omega N/c$, where $N = n + i\kappa$ is the complex refractive index [57].

$$E(z,t) = Ee^{i(kz-\omega t)} = \begin{pmatrix} E_x \\ E_y \end{pmatrix} e^{i(kz-\omega t)} \text{ where } E_x = A_x e^{i\phi_x},\ E_y = A_y e^{i\phi_y} \tag{2}$$

The first convention is the Jones formalism, which typically describes the phase and amplitude of light in the horizontal and vertical planes with respect to direction of propagation (e.g. the X and Y) where E is the input wave, J is the Jones vector describing any optical element, and E' is the transmitted wave Eq. 3 [57].

$$E' = \begin{bmatrix} E_x' \\ E_y' \end{bmatrix} = \begin{bmatrix} J_{11} & J_{12} \\ J_{21} & J_{22} \end{bmatrix} \begin{bmatrix} E_x \\ E_y \end{bmatrix} = JE \tag{3}$$

An optical system can be completely described by a multiplication of Jones matrices for each element with particular attention paid to the order in which the light propagates through each element as shown in Eq. 4.

$$E' = J_n J_{n-1} ... J_1 E \tag{4}$$

The second is by the Mueller Matrix or Stokes Vector, which describes the intensity, horizontal/vertical, diagonal, and circular polarization components of light, where S is the Stokes vector representation of the input wave, M is the Mueller matrix representation of any optical element, and S' is the resulting Stokes vector describing the output Eq. 5. I represents the intensity of the wave, Q is the horizontal (+1) or vertical (-1) component, U is the diagonal component (+1 for $+45°$ and -1 for $-45°$), and V encapsulates the circular component (+1 for right-handed and -1 for left-handed) [56, 52].

$$S' = \begin{bmatrix} I' \\ Q' \\ U' \\ V' \end{bmatrix} = \begin{bmatrix} M_{11} & M_{12} & M_{13} & M_{14} \\ M_{21} & M_{22} & M_{23} & M_{24} \\ M_{31} & M_{32} & M_{33} & M_{34} \\ M_{41} & M_{42} & M_{43} & M_{44} \end{bmatrix} \begin{bmatrix} I \\ Q \\ U \\ V \end{bmatrix} \tag{5}$$

Similar to Eq. 4, the Mueller description of an optical system is similar, shown in Eq. 6.

$$S' = M_n M_{n-1} ... M_1 S \tag{6}$$

Both notation systems fully characterize the polarization state of light and can represent the polarization effects of optical elements. A tissue sample can also be thought of as an optical element that has distinct effects on the polarization of light. If a system is carefully characterized, the Jones or Mueller matrix describing the tissue sample can be determined. This dissertation will focus primarily on tissue birefringence and the optical scattering in orthogonal polarization channels.

Birefringence can be characterized by the phase difference or retardance imparted on orthogonally polarized light, η in Eq. 7, and the angle of the optical axis relative to the incident beam polarization, $\theta_{(OA)}$ [57]. This phase difference is caused by differences in refractive index relative to the optical axis. These differences in refractive index can arise from the intrinsic structure of the medium (such as crystal structure or molecular asymmetry) or from a bulk property of the form of the material (a collection of fibers) or even from stress on the material [56]. The index as a function of angle about the axis is referred to as the index ellipsoid. The minor axis of the ellipse has refractive index n_o, and transmits what is referred to as the ordinary ray. The major axis of the ellipse has a greater refractive index n_e, and transmits what is referred to as the extraordinary ray. The difference between n_o and n_e is what gives rise to the phase difference, η.

$$\eta = \phi_x - \phi_y \tag{7}$$

2.3 Methods of Scattering Measurement

Biomedical imaging has recently begun to leverage tissue scattering as both a source of contrast and a metric of tissue state [53, 58]. The ability of scattering to describe tissue at different length scales and its implications in biological processes and disease make it a useful metric to consider. Furthermore, the ability to image scattering without the use of contrast agents makes scattering an ideal target in clinical translation.

Several methods exist which quantify scattering, such as goniometry [59, 60, 61], reflectance con-

focal microscopy [62, 63], spatial frequency domain imaging (SFDI) [64, 65], integrating sphere [66, 67], angle-resolved low coherence interferometry (a/LCI) [68, 69], enhanced backscattering spectroscopy (EBS) [70, 71], and optical coherence tomography [72, 73, 74]. As is often the case, each method possesses different advantages and disadvantages. Generally, these methods can be classified into two general categories: those which are solely a measurement of scattering and those which also form an image of the sample. A summary of these methods is provided in Table 2.1.

Method	Effective Resolution	Imaging Capable	Depth Resolution	Scattering Parameters	Sample Preparation
Goniometry	n/a	no	no	μ_s, g, $p(\theta)$ μ_b, g, μ_s'	thin slices
Reflectance Confocal	1 μm	yes	scanning	μ_b, μ_s, g, μ_s'	none
SFDI	10 μm	yes	no	μ_s', g, μ_s	none
Integrating Sphere	n/a	no	no	μ_s, g, μ_s'	thin slice
a/LCI	10 μm	pseudo	yes	μ_s, g, μ_s'	none
EBS	n/a	no	no	μ_s', μ_s, g, D	none
OCT	$5-10$ μm	yes	yes	μ_s, μ_b, g	none

Table 2.1: Several methods exist for measuring optical scattering properties. Each method involves some compromise between rigorous measurement of optical scattering, imaging capability, and sample preparation.

The non-imaging methods offer some unique features that are typically not found in imaging systems. Methods such as goniometry and integrating sphere are able to measure light at many angles, including the forward angles, which is difficult in clinical applications due to their tendency to be constructed in epi-mode [59, 61]. While these methods provide a more complete map of scattering and scattering as a function of angle, their sample requirements and instrument construction leave them unsuitable for clinical translation. However, their importance in scattering should not be understated as their wide angular field of measurement makes them uniquely qualified in better modeling scattering phase function which is a critical step in designing other instruments aiming to measure scattering in the clinic.

Other techniques which begin to branch into the imaging realm such as a/LCI, SFDI, and EBS also offer a mix of advantages and disadvantages. Each of these methods has been explored for potential use in the clinic and noted for their ability to be easily adapted to endoscope geometry. SFDI has shown potential in characterizing polyps in the colon via measurement of the reduced scattering coefficient but relies on an LUT and requires more complex illumination schemes [75, 76].

The use of a/LCI to detect dysplasia in Barrett's esophagus has been a growing topic of interest as well [77] and complements OCT instrumentation rather well owing to both instruments being interferometric. However its clinical development is still ongoing. EBS is an interesting technique which can be sensitive to changes in scattering caused by tissue ultrastructure on the scale of approximately 30 nm [78], however it is limited to sampling all scattering within the diameter of its illumination beam and it lacks imaging capability.

2.4 Optical Coherence Tomography

Optical coherence tomography (OCT) is a clinically-approved method of interferometric imaging which can acquire high-resolution volumetric images [79]. Introduced as the developed method in 1991 by the Fujimoto group, OCT uses backscattered light as its source of contrast, making it inherently sensitive to optical scattering in tissue [79]. Presented here is the development of a visible-light (VIS) OCT system to characterize optical scattering. The polarization and spectral dependence of optical scattering was assessed as a potential marker for monitoring fibrosis in animal models.

Briefly, Spectral-Domain OCT (SD-OCT) or Fourier-Domain OCT (FD-OCT) is a laser scanning microscopy technique which uses interference to recover a depth profile at each point in the scan. FD-OCT was described by Fercher in 1995 as spectral low-coherence interferometry [80], with the first retinal images being published from the Fercher group by Wojtkowski *et al* [81]. An excellent description of the development of OCT can be found in Reference [82] and Reference [83]. Several technical and mathematical aspects are well-described by Izatt and Choma in Reference [84], which is the second chapter of Reference [83]. Backscattered light from the sample interferes as a function of wavelength and is resolved using a spectrometer. The Resolved interferogram an be converted to a depth profile by use of a Fourier transform, see Eq. 8 where $I(k)$ is the interference intensity as a function of wavenumber, k ($k = 2\pi/\lambda$), and $I(z)$ is the resulting image intensity as a function of depth or optical path, z [85].

$$I(k) \xrightarrow{\mathscr{F}} I(z) \tag{8}$$

2.4.1 Theory of Fourier-Domain OCT

Spectral interference can be easily conceptualized using a Michelson interferometer with a pair of mirrors at identical distance, z_0. Briefly, a collimated light source with intensity I_0 is separated by a beamsplitter into two paths of equal length and with equal intensity ($1/2I_0$). At distance z_0, each beam reflects from a mirror back into the beamsplitter. The beams recombine and and interfere constructively since the mirrors are both at z_0, giving the resulting wave a maximum intensity of I_0. However, as the position of one mirror changes relative to the other, the interference changes. The distance of the stationary, or *reference*, mirror is still z_0 and the moving mirror, or *sample* mirror, changes by some z to have a final position $z_0 + z$. The result is that the waves will now be out of phase and will shift from destructive interference as the value of z approaches $\lambda/2$ (a half wave) where the maximum intensity of the interference is now zero. One can imagine that now any maximum intensity value between zero and I_0 can be achieved by shifting the sample mirror throughout a full wave of delay, or 2π radians. These can all be described, conveniently, by a sinusoid and denoted by a complex exponential in Eq. 9 where $\phi = z_0 - z$ in wavenumber, k [56].

$$I_{det}(\phi) = I_0 exp(-2i\pi\phi) \tag{9}$$

An oscillatory function can also be achieved by keeping the sample mirror stationary at some $z_0 - z$ and varying the wavelength. The physical separation of the mirrors will result in a different amount of phase depending on wavelength. For a pair of mirrors with 100 μm of separation, light with a wavelength of 500 nm will have a phase difference 200 cycles (or 400π radians) while light with a wavelength of 570 nm will have a phase difference of 175.5 cycles (or 351π radians). Imaged with a spectrometer and plotted as a function of k, interference for a single object at $z_0 - z$ produces a single sinusoid. The Fourier transform of this sinusoid produces a peak at value $z_0 - z$. Significantly, the use of the Fourier transform also allows interference signals (sinusoids) to be resolved for several objects as a function of z. This leads to Eq. 10, a more comprehensive form of Eq. 8 [84, 85].

$$I(z) = \mathscr{F}\big(I(k)\big) = \mathscr{F}\big(I_0 exp(-2i\pi\phi(k,z))\big) \tag{10}$$

As with any Fourier-based imaging method, the limits of Nyquist sampling still apply. In the case of FD-OCT, the source bandwidth determines the axial resolution, δz, and the resolution of the spectrum on the detector, $\delta\lambda$, determines the axial range of imaging, Δz [84, 85]. Based on these factors, an ideal FD-OCT source will use a large bandwidth source which is dispersed over a large detector with small pixels. Axial resolution can be well-described by the coherence length of the source, Eq. 11, where λ_0 is the source center wavelength and $\Delta\lambda$ is the FWHM of the source intensity across wavelength [84]. The axial range of imaging can be determined from either the axial resolution multiplied by the number of pixels used on the spectrometer or by the coherence length of a single pixel based on the bandwidth binned into a given pixel m, $\delta\lambda_m$ [84]. The latter is expressed in Eq. 12, where for a spectrometer with a reasonable resolution of 0.10 nm/pixel with $\lambda_{0,m} = 500$ nm the full axial range of imaging will be approximately 1.1 mm [84]. However, this value must be divided by 2 since the Fourier transform produces a symmetric function about 0, which in the case of FD-OCT produces a complex conjugate image that is not used in imaging. This means the maximum one-sided imaging depth for this example system will be approximately 0.55 mm.

$$\delta z = \frac{2ln(2)}{\pi}\frac{\lambda_0^2}{\Delta\lambda} \tag{11}$$

$$\Delta z = \frac{2ln(2)}{\pi}\frac{\lambda_{0,m}^2}{\delta\lambda_m} \tag{12}$$

As an example of these properties, an example spectrum is demonstrated in Figure 2.1. In the top panel, the real component of our interferogram intensity, $I(k)$, is displayed and its corresponding Fourier transform, $I(z)$, is shown in the bottom panel with an independent axis of depth in microns. Note the symmetry of the resulting Fourier transform, which has been documented extensively elsewhere. For OCT signal processing, only the real portion of the signal is considered and the conjugate is removed by a simple processing. Signal in OCT imaging is displayed in dB units and is discussed further in Section 2.4.2.

Finally, since FD-OCT is also a laser-scanning method of imaging, the lateral resolution, δx, and field of view, FOV_x, can be characterized. These follow from conventional limits on laser-scanning microscopy. Lateral resolution follows the Abbe limit of diffraction, Eq. 13, where NA is

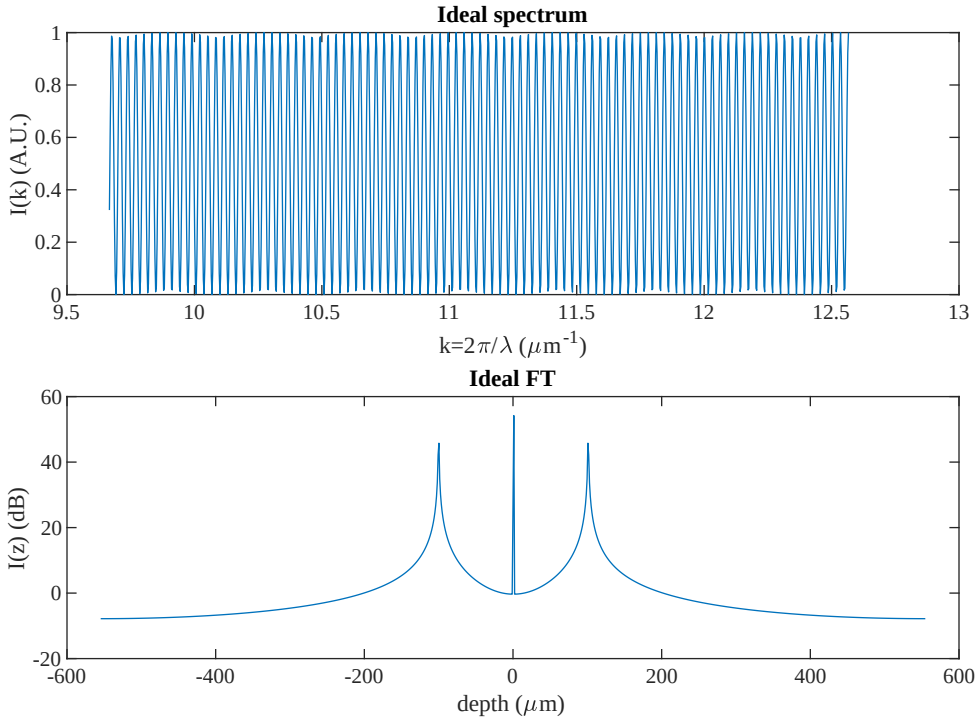

Figure 2.1: Top: A synthetic interference intensity, $I(k)$, for an optical path difference between the sample and reference arm of 100 μm. Bottom: The resulting Fourier transform with the redundant images.

the numerical aperture of the objective [84]. For a laser scanning microscope objective, the NA follows from convention, Eq. 14, where θ is the acceptance angle. Typically, θ is based on the objective aperture and focal length, however, in this case it is based on the diameter of the galvo mirrors which drive the scanning, Eq. 15.

$$\delta x = \frac{1.22 \times \lambda_0}{2 \times NA} \tag{13}$$

$$NA = nsin(\theta) \tag{14}$$

$$\theta = tan^{-1}\left(\frac{d_{galvos}}{f}\right) \tag{15}$$

The lateral field of view is theoretically restricted by the clear aperture of the objective. However, galvo voltage range, range of motion, and aberrations of the objective lens are typically the

leading factors. A typical OCT system is capable of imaging 1000-2000 diffraction-limited spots within its field of view to proved a lateral scale on the order of millimeters.

2.4.2 Signal Digitization and Sensitivity Limits

Image reconstruction in OCT is a mosaic of Fourier transforms of spectral interferograms which are imaged with a spectrometer consisting of a dispersive element such as a grating or prism, a lens, and the detector [84, 85]. The interferograms are often recorded with line-scan detectors which have a compact $1 \times m$ row of pixels that can be read out at kilohertz rates for rapid image acquisition. The construction of the spectrometer and detector are both critical to take into account when designing an OCT instrument. All instruments developed as a part of this thesis used a transmission grating for the dispersive element.

The digitization of the signal of the signal must be carefully considered in OCT [84]. A detector will bin wavelengths into discrete pixels, which have a set size, maximum bit-depth, and read noise. The size of the pixels has a direct relationship with the Fourier processing of the interferogram as discussed previously in Section 2.4.1. Additionally, the integrative nature of the Fourier transform also implies that with a larger number of pixels used, a greater amount of total optical power may be collected to fill the available bit-depth. The bit-depth of the detector will also impact the signal and noise levels of the resulting OCT image. A simple conceptualization of these phenomena is for a single interface, which produces a single frequency in the interferogram. This oscillating wave form produces a pair of conjugate peaks in the Fourier transform, only one of which is used for the real image. This peak intensity relative to the noise floor of the A-line forms the basis of OCT SNR, which is described by Eq. 16. In this equation, it should be noted that the resulting units will be decibels and that $20 \times log_{10}(signal)$ is used rather than the conventional $10 \times log_{10}(signal)$ [84]. This is due to the detected optical intensity being proportional to the detector voltage, meaning that the square of intensity is proportional to the detector power [84]. Thus, the additional factor of 2 when converting to decibels. While other conventions exist, this manuscript will use the $20 \times log_{10}(signal)$ definition when units of decibels are used for more appropriate comparisons to

other authors in the literature.

$$SNR_{OCT} = 20 \times log_{10}\left(\frac{P_{signal}}{P_{noise}}\right) \tag{16}$$

Wavelengths from the grating are focused onto discrete pixels by the lens. This process will bin a range of wavelengths based on the grating, lens, and pixel size. Ideally, a lens will be chosen which produces a diffraction-limited spot roughly equal to the pixel size of the detector. This can be determined similarly to the objective spot size using Eqs. 13, 14, and 15, however the focal length here is of the spectrometer lens rather than the objective. Using a visible light source and a focal length of approximately 100 mm will produce a spot size of approximately 15 μm for a beam with 5 mm diameter. All instruments developed as a part of this thesis use detectors with pixel sizes of 14 μm and have a bit depth of 12. To briefly summarize these points, simulated interference signals and their corresponding Fourier transforms are shown in Figure 2.2. The key takeaway in these plots is that the OCT signal intensity and SNR performs best with more optical power incident on and collected from the sample. The maximum fringe intensity will give the highest SNR for the given arrangement. Extracting this fringe contrast will be discussed further in Section 2.5.1.

It can be observed in both Figure 2.1 and Figure 2.2 that the noise floor of the OCT signal is not constant. Rather, there is a smooth roll-off in depth which is typically referred to as $1/f$ noise, or pink noise. This noise is intrinsic to interferometric detection and several methods have been used to explore its removal. The presence of noise is particularly problematic when addressing other sources of intrinsic signal fall-off. OCT suffers from two sources of intrinsic fall-off: spectrometer sensitivity roll-off [86, 87] and the confocal point spread function (PSF) [73, 84, 86]. These two sources of signal fall-off reduce signal intensity with depth according to the physical parameters of the spectrometer and imaging objective, respectively. The spectrometer sensitivity fall-off has been well-characterized [86] and describes the decrease in interference fringe contrast with increasing fringe frequency and is characterized by Eq. 17, where ζ is z/z_{max} (recall from Eq. 12 that $z_{max} = \Delta z/2$), $\delta\lambda$ is the maximum resolution of the spectrometer, and $\Delta\lambda$ is the sampling of the spectrum on the detector (i.e. the actual resolution achieved).

$$f(z) = \left(\frac{sin(\zeta)}{\zeta}\right)^2 exp\left(-\frac{\left(\frac{\delta\lambda}{\Delta\lambda}\right)^2}{2ln(2)}\zeta^2\right) \tag{17}$$

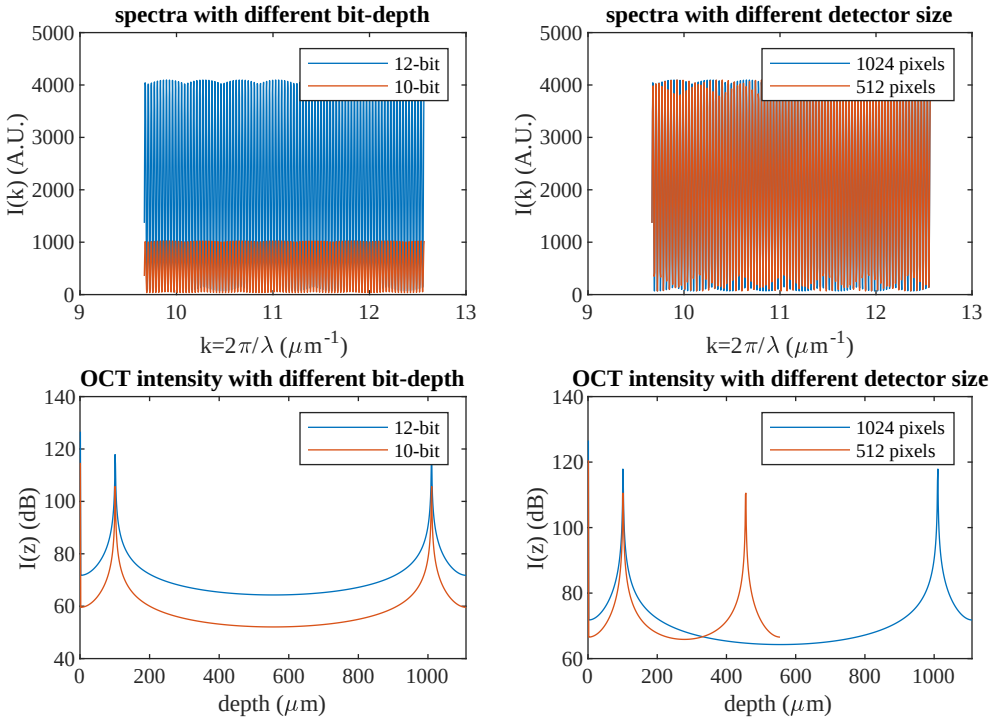

Figure 2.2: Top right: Interference spectra with different bit depths of detector, 12-bit (blue) and 10-bit (red). Top right: Identical spectra with the same bandwidth over a different detector size (effectively halving the spectral resolution), 1024 pixels (blue) and 512 pixels (red). Bottom left: The corresponding Fourier transforms of spectra in the plot above appear different at first glance but the peak to noise distance is equivalent for 12-bit (blue) and 10-bit (red). Bottom right: The corresponding Fourier transforms for the plot above which demonstrate the impact of wavelength sampling on the Fourier transform where the finer sampling (1024 pixels in blue) has a greater bandwidth/depth range compared to poorer sampling (512 pixels, red)

The confocal PSF has also been explored previously and accounts for the depth of focus (DOF) of the objective [73, 84, 86]. The DOF of an objective is inversely related to the square of the NA, meaning that the DOF exponentially decreases as the NA increases. Keeping Eq. 13 in mind, increasing the NA of an objective creates a focal volume that is increasingly fine. Typically, volumetric imaging leverages both the decrease in DOF and finer lateral resolution to achieve high resolution results and minimize the collection of scattered light when axial scanning is used in conjunction with a confocal pinhole or other method of optical sectioning [62]. However, because OCT collects axial information without scanning, i.e. a collection of all depth information during a single exposure to the camera, a large DOF is, in fact, very useful for even illumination of the sample. A low-NA objective is not only useful for extending the illumination intensity over the

sample in depth but also for rejecting light scattered from outside the focal depth, owing to the small collection angle of the NA. A typical OCT instrument will use an objective with NA below 0.1 which can be used to calculate DOF according to Eq. 18. For a visible light system with an NA between 0.1 and 0.025, the DOF will range from 125 μm to 2 mm.

$$DOF = \frac{0.565\lambda}{sin^2\left(\frac{sin^{-1}(NA)}{2}\right)} \tag{18}$$

The depth-dependent fall-off from the confocal PSF characterizes this effect well and is described by Eq. 19 [73, 86], where z_0 is the axial position of the focal plane, n_{smp} is the refractive index of the sample, and z_r is the Rayleigh range of the beam. The Rayleigh range is roughly equivalent to the DOF as calculated in Eq. 18.

$$h(z) = \left(\left(\frac{z - z_0}{n_{smp} z_r}\right)^2 + 1\right)^{-1} \tag{19}$$

Finally, the two sources of depth-dependent signal fall-off, Eqs. 17 and 19, can be multiplied to describe the total intrinsic signal fall-off in the OCT system [86]. The inverse of the resulting function provides a restoration filter which can be used to more accurately represent the OCT intensity signal, see Eq. 20. Care must be taken, however, to remove as much noise as possible in the image before restoration, since the noise values at the greatest depths can be magnified beyond reasonable limits. A plot of the two sources of fall-off and their combination can be observed in Figure 2.3. Each line of the plot shows the one-sided FWHM of the intensity as a function of depth, which can be used to characterize the common -6 dB range characteristic for an OCT instrument. This value for the yellow curve in Figure 2.3 can be estimated as 225 μm, where the signal falls to half the maximum value.

Several design choices can be made which leverage Eqs. 17 and 19 to the advantage of the user to minimize the intrinsic system fall-off. These will be discussed in detail for the systems used in this dissertation in the appropriate sections (Sections 3.2.2 and 6.2.4).

$$F(z)_{restoration} = \big(f(z) \times h(z)\big) \tag{20}$$

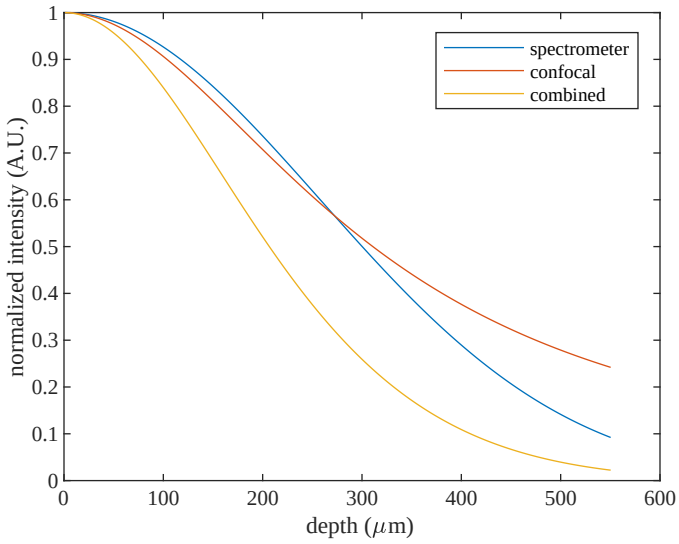

Figure 2.3: Depth-dependent fall-off of the OCT signal due to the spectrometer sensitivity (blue), confocal PSF (red), and the combination of the two (yellow).

2.5 Scattering and Fibrosis Sensitivity in OCT

2.5.1 Determining Optical Properties from OCT Signals

Since OCT images backscattered light directly, its contrast is rooted in the scattering properties of the sample [73, 79]. With careful analysis, OCT images can be used to quantify optical scattering. The signal intensity of OCT can be well-described by starting with the equations describing the detected intensity (I_{det}) of interference, see Eq. 21, where E_r is the amplitude from the reference arm, E_s is the amplitude from the sample arm, and * denotes the complex conjugate [56].

$$I_{det} = |E_r + E_s|^2 = E_r E_r^* + E_s E_s^* + E_r E_s^* + E_s E_r^* \tag{21}$$

Here, the terms can be described as the autocorrelation of the reference and sample arms, $E_r E_r^*$ and $E_s E_s^*$ respectively, and the cross-correlation of the reference and sample arms which produce the fringes of interest, denoted by I_{cross}. The contribution to the cross terms can be conceptualized as the interference between the reference amplitude and the amplitude contributed at each depth in the sample. This can be described mathematically by Eq. 22, where I_R is the intensity from the

reference arm and I_S is the intensity from the sample arm.

$$I_{cross} = E_r E_s^* + E_s E_r^* = \sum_{n=1}^{N} \sqrt{I_R I_S}\Big[exp\big(i2\phi(k,z)\big) + exp\big(-i2\phi(k,z)\big)\Big] \tag{22}$$

These intensities can be well described by Eq. 23 and Eq. 24, where I_0 is the source intensity.

$$I_R = I_0 R \tag{23}$$

Here, R is the reflection coefficient of the reference surface, typically glass.

$$I_S = I_0 \mu_b(z) exp\big(-2zn\mu_s(z)\big) \tag{24}$$

Where $\mu_b(z)$ is the backscattering coefficient as a function of depth within the sample, $2zn$ is the total round-trip optical path of light traveling into and out of the sample, and $\mu_s(z)$ is the scattering coefficient as a function of depth within the sample. In the case of OCT, only the backscattered light returns to the system and is interfered with the reference arm, so the signal intensity becomes proportional to μ_b and decays exponentially with depth according to the extinction equation for a wave propagating through a given medium [52, 73].

As was discussed in Section 2.4, the OCT signal is the Fourier transform of the interferogram. Using Eq. 8, we can observe that the impact of scattering coefficients, μ_s and μ_b are outside of the Fourier kernel and are thus independent in the transform (Eq. 25 and a simple substitution shows that μ_s acts as an exponential decay term in the signal (Eq. 26) [73, 88].

$$I(z)_{OCT} = \mathscr{F}(I(k)_{cross}) = 2\sqrt{I_R I_S} \tag{25}$$

$$I(z)^2_{OCT} = 4I_0^2 R \mu_b(z) exp\big(-2zn\mu_s(z)\big) \tag{26}$$

In the case of a homogenous scatterer, the intensity as a function of depth is a smooth exponential decay which can be readily fit to determine the bulk scattering coefficient [73, 88, 86]. With proper detector characterization and input power monitoring, the backscattering coefficient can also be readily determined. However, due to the signal being sensitive to scattering and backscat-

tering as a function of depth, the local optical properties can be determined with a sufficiently high resolution image [86].

2.5.2 Leveraging OCT Data for Fibrosis: Polarization and Spectral Dependence

Fibrosis in tissue consists of several nano-scale and micro-scale changes in ECM architecture [25, 31, 41]. These changes can include the size, density, and collective orientation of collagen fibers [31, 11]. To best measure fibrosis using OCT, instrument design and data analysis must be optimized for sensitivity to changes in contrast caused by fibrosis. The intrinsic and form birefringence of collagen has been well-studied with other optical methods which have produced valuable data in understanding collagen deposition and organization in several diseases [31, 11, 35]. Polarization effects and birefringence can also be measured with OCT and several active areas of research exist to advance both a bench-top and clinical polarization-sensitive OCT (PS-OCT) devices [89, 90, 91]. See Section 2.2.2 for the full explanation of notation of polarized light.

Polarization-sensitivity can be easily incorporated into the optics of most OCT systems [57, 83]. Briefly, the source polarization is refined to some pure linear polarization upstream of the Michelson interferometer. The reference arm of the OCT will contain the necessary waveplates to convert the input polarization state to a linear $\pm 45^{\circ}$ polarization after reflection. The sample arm is converted to a form of circular polarization to ensure even illumination of the sample regardless of the orientation of the optical axis, θ_{OA}. The critical change in the instrumentation is now in the detection. The recombined light will interfere with some unknown polarization. The OCT detector must now separate the signal into orthogonal polarization components which are detected simultaneously. Several methods exist to accomplish this task and one may chose which best suits existing constraints on detector geometry.

The separated polarization states interfere at the detector and produce two signals typically referred to as $I_x(z)$ and $I_y(z)$ or $I_h(z)$ and $I_v(z)$. Two key considerations must be prioritized in the detection of these signals. The first is that the reference arm achieve an equal magnitude of the detected polarization states. This will ensure that all signal from the sample is interfered equally. The second is that the detection of the two spectra be carefully calibrated for qualitative use. This can be done using identical detectors or directing both signals onto the same detector.

At the fundamental level, the difference in refractive indices results in a differing pathlength for

the orthogonal polarizations, $\Delta n = n_e - n_o$ and is described by $\delta_s(z)$ in Eq. 27. For a constant Δn in depth, this will produce a linear accumulation of path difference or phase retardation between the two orthogonal polarization images.

$$\delta_s(z) = \Delta n z \tag{27}$$

The phenomenon of this small increase in optical path length is described clearly in work by Gotzinger [92] (which is based on earlier work from Hee *et al* in the Fujimoto group [93]) as a low-frequency signal which modulates the image intensity. This carrier frequency is equal to the envelope of the analytic signal in the Fourier domain, or the FD-OCT image as shown in Eq. 28. The Fourier transform, $I(z)$, of the real-valued interferogram, $I(k)$, is complex-valued and is thus a complete analytic signal. The envelope of the analytic signal is then retrieved by taking the absolute value, which for Eq. 28 yields $A(z)$. This is, conveniently, the FD-OCT image. The phase information of the Fourier transform can also be readily determined using the arctangent to obtain $\Phi(z)$.

$$\mathscr{F}\big(I(k)\big) = \tilde{I}(z) = A(z)exp\big(i\Phi(z)\big) \tag{28}$$

Work from Fujimoto[93] and Hitzenburger [91] has demonstrated that the envelope of the image, $A(z)$, can be used to obtain the accumulated retardance, $\delta_s(z)$, from orthogonally polarized OCT images by expressing the envelope using the sample reflectivity, $R(z)$, according to Eq. 29. If the FD-OCT images are reconstructed properly, the $R(z)$ component between them will be identical as it is a sample-dependent property. By adding a polarization-diverse elements such as a beamsplitter to the detection arm, two orthogonally polarized OCT signals may be detected. These signals are referred to here as x and y rather than horizontal and vertical since their requirement is only that they are orthogonal and need not be exactly the horizontal or vertical states.

$$\begin{aligned} |I_x(z)| = A_x(z) &= \frac{\sqrt{R(z)}}{2\sqrt{2}} cos\big(\delta_s(z)\big) \\ |I_y(z)| = A_y(z) &= \frac{\sqrt{R(z)}}{2\sqrt{2}} sin\big(\delta_s(z)\big) \end{aligned} \tag{29}$$

Due to $R(z)$ being sample-dependent, a division of the signals will eliminate the factor of $R(z)$ and leave only the components caused by sample birefringence leading to an accumulation of retardation between the polarization states, $\delta_s(z)$ [91, 93]. Conveniently, due to the 90° phase shift between the orthogonal states, the remaining terms are this sine and cosine of the accumulated retardance. This means that their ratio would the tangent of their argument and it follows that the arctangent of the ratio would give us directly the accumulated. This process is summarized by Eq. 30 [92, 91, 93]. Two technical details should be noted at this point. First, due to the processing of the arctangent function, there is an ambiguity when a phase shift of $\pi/2$ radians is achieved where the function appears to decrease [57]. This can be dealt with by assuming *a priori* knowledge of the sample structure or by using advanced methods which will be discussed further in Section 3.3.2. Second, the measured quantity is the accumulated retardation in depth, $\delta_s(z)$, which would increase linearly for a material with constant birefringence. The implication of this is that the delay introduced by any pixel in depth is equal to the local derivative, and thus the true birefringence of the sample $(n_e - n_o)$ is equal to this retardation divided by the pathlength of one pixel [57]. All measurements presented in this manuscript will either express the accumulated retardance, $\delta_s(z)$ or make clear when the per pixel retardance is displayed.

$$\delta_s(z) = tan^{-1}\left(\frac{A_y(z}{A_x(z)}\right) = tan^{-1}\left(\frac{sin(\delta_s(z)}{cos(\delta_s(z)}\right) \tag{30}$$

The angle of the optical axis, θ_{OA}, can be derived from the phase difference $(\Delta\Phi = \Phi_x - \Phi_y)$ between the Fourier images and adjusting for the 90° phase shift from the orthogonal polarizations, see Eq. 31 [92, 91, 57]. The phase of the Fourier images is readily available as the arctangent of the complex-valued Fourier signal, as discussed above, which returns the argument of a complex exponential.

$$\theta_{OA} = \frac{\pi - \Delta\Phi}{2} \tag{31}$$

Optical scattering exhibits a substantial dependence on wavelength presents a valuable source of information [88, 94]. Spectral scattering has been identified as useful data to estimate higher-order optical properties of tissue such as the anisotropy of scattering, g, and the so-called fractal dimension, D, which is a measure of tissue self-similarity over length scales [88, 54, 55]. Spectroscopic

characterization can be developed synergistically with OCT since both benefit from expanding bandwidth. Spectroscopic OCT and related techniques operate by using windowing filters in the spectral domain to smoothly downsample the interferogram into several overlapping bins. These new spectra can be subjected to identical OCT processing to produce OCT images with poorer axial resolution but which can be leveraged to characterize spectral behavior. Work from others has demonstrated the utility in applying this method for spectral behavior of scattering and polarization. A representation of this method can be found below in Figure 2.4. The number of bins and the amount of overlap between windows can be adjusted and benefits from having a large available bandwidth. Independent signal processing allows for independent adjustment of chromatic dispersion and identification of polarization mode dispersion [88, 95].

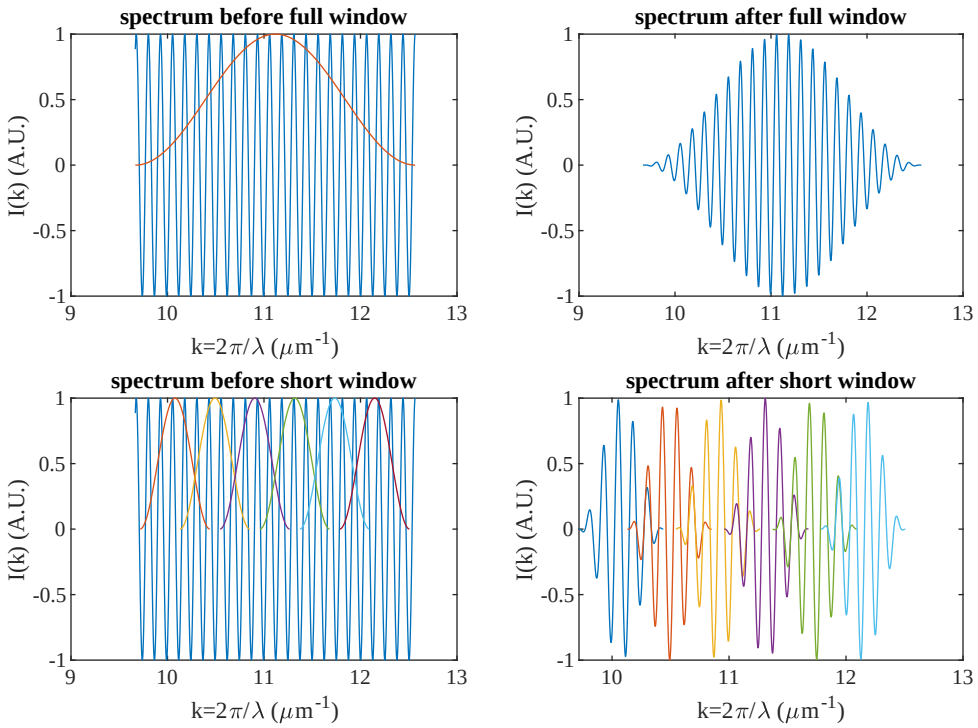

Figure 2.4: Top row: The spectrum before and after its multiplication with a single Hanning window. Bottom row: The spectra produced by using multiple narrow Hanning windows with some overlap. The resulting multiple spectra can each produce an OCT image which can be used to calculate optical scattering properties.

It should be noted that this technique has great potential in the visible regime. In part, this is due to the dependence of scattering on wavelength meaning that greater contrast would be seen

between bins compared to a NIR source. The other aspect which makes this method attractive is the superior axial resolution available to visible light sources (see Eq. 11). The difference in coherence length for a source centered at 750 nm versus 500 nm will be greater than a factor of two, if bandwidth is equal. Thus, a visible source can afford to incorporate this shortwave technique to use only half the available bandwidth per window and still have equal axial resolution to the NIR source.

3 Development of the Optical Coherence Tomography Platform

3.1 VIS-OCT Instrument Design

OCT can be thought of as a combination of a laser-scanning microscope and a Michelson interferometer. The lateral resolution and field of view are dictated by the optical design of the scanning microscope and the interferometer encodes the axial information as interference. This information is then decoded by the spectrometer where a Fourier transform produces the image.

The instrument was constructed based on a free-space Michelson interferometer and follows the diagram in Figure 3.1. A broadband source was coupled into a reflective collimation package and directed to a beamsplitter. The beamsplitter separates the light into the reference arm and sample arm. The reference arm consisted of a dispersion compensator matched to an imaging objective. An adjustable aperture is used to match the beam diameter to the scanning mirror diameter, and neutral density filters to attenuate the intensity. A piece of reflective glass used to produce a reference reflection at the same phase position as the sample. The sample arm consisted of a pair of galvo scanning mirrors and a laser scanning microscope objective. The scanning mirrors and objective focus light onto the sample and allow for two-dimensional scanning across the sample.

Backscattered light from the sample is collected by the low-NA objective and de-scanned through the mirrors where it recombines with the reference reflection at the beamsplitter. The recombined light interferes as it is directed to a transmission grating. The grating separates the light spectrally before it is focused by a lens onto a camera resulting in an interferogram as a function of wavelength. A Fourier transform of the spectrum as a function of wavenumber ($2\pi/\lambda$) reconstructs the image in depth at each scanned point in the sample.

The laser sources used for this instrument were broadband supercontinuum sources from NKT photonics. The SuperK Xtreme and SuperK Kompact were used in various applications of this instrument. Both sources were filtered to select the visible regime before being fiber-coupled into the instrument. The bandwidth available was approximately 475 nm to 675 nm; however, the intensity at the ends of the spectrum was too low to be sufficiently utilized and the effective bandwidth of the system, $\Delta\lambda$, was 500 nm to 650 nm with a mean wavelength, λ_0, of 575 nm which was used to calculate the system parameters.

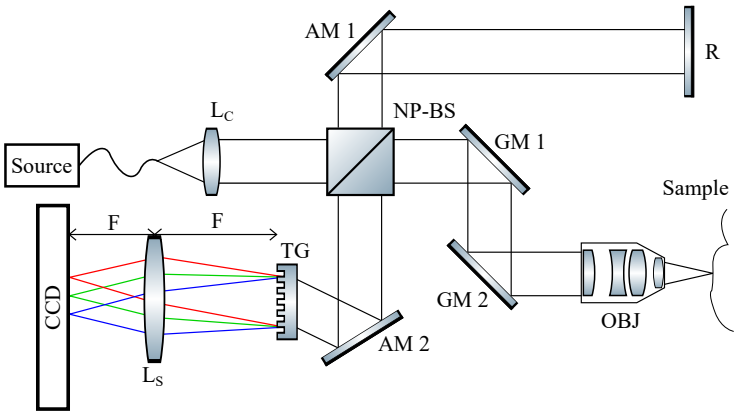

Figure 3.1: A source is collimated by a collimation package (L_c) before being separated by the non-polarizing beamsplitter ($NP\text{-}BS$). The reference reflector (R) is at a nearly identical distance as the sample and is aligned with the sample beam by the adjustment mirror ($AM\ 1$). The light in the sample arm is scanned by two galvo mirrors (GM) across the back aperture of a laser scanning objective (OBJ). The beams recombine and are directed by an adjustment mirror ($AM\ 2$) to a transmission grating (TG). The spectrally separated light is focused by a spectrometer lens (L_s) onto the camera (CCD).

3.1.1 Optical Design

The scanning optics were designed to produce a large field of view with minimal aberrations. In this case, a laser scanning microscope objective coupled with a pair of 5 mm galvos was used. In typical microscopy applications, high resolution is achieved through high NA, which decreases the beam lateral waist while also minimizing depth of focus (DOF). For volumetric imaging techniques which possess innate optical section or which use some physical method of sectioning, a low depth of focus is ideal. In OCT, however, the full range of the axial image is acquired all at once meaning a low depth of focus is undesirable. Depth of focus is a function of approximately NA^{-2} (see Eq. 18) while lateral resolution is a function of NA^{-1} (see Eq. 13) meaning that the depth of focus will increase at a greater rate than airy disk radius [84]. This allows a compromise to be made where the depth of focus can be sufficiently large to provide an even illumination over the sample depth without the lateral resolution becoming too poor as to be useful to the application. This system was constructed with a 39 mm effective focal length laser scanning objective (Thorlabs LSM03-VIS), which provided an effective NA of 0.06 when paired with the 5 mm galvo mirrors. From Eq. 32, the system depth of focus was approximately 350 μm. From Eq. 33 the lateral resolution

was approximately 6 μm. These equations are reprinted here for convenience from Eqs. 13 and 18 in Sections 2.4.1 and 2.4.2 respectively where they are introduced and discussed more fully.

$$DOF = \frac{0.565\lambda_0}{sin^2\left(\frac{sin^{-1}(NA)}{2}\right)} \tag{32}$$

$$\delta_x = \frac{1.22 \times \lambda_0}{2 \times NA} \tag{33}$$

The spectrometer was designed based on the Fourier properties of the image reconstruction as discussed in Section 2.4.1. To briefly summarize the bandwidth, $\Delta\lambda$, of the spectrum determines the resolution of the Fourier transform, the image space. Conversely, the sampling rate of the spectrum determines the field of view of the image space. Spectrometer design was varied using different transmission gratings and different focal length lenses to image the spectrum onto the detector. The resolution of the spectrometer was also limited by the beam diameter, which in turn limits the number of lines illuminated on the grating. In the case of this instrument, beam expansion was not used to minimize complexity, footprint, and aberrations. Thus, the 5 mm diameter of the galvos determined the resolution for each grating. In these studies, 600 line pairs/mm, 830 line pairs/mm, and 1200 line pairs/mm gratings were used in the system. A 100 mm focal length lens was used to focus the dispersed spectra on a detector. The pixel size was the final consideration of the spectrometer design. Two detectors were used to construct OCT spectrometers, both of which possessed identical pixel sizes of 14 μm, the only substantial difference being the number of pixels and their arrangement on the detector. These detectors are discussed further in section 3.1.2. Below in Table 3.1, the spectrometers resolution, pixel sampling rate of the detector, and axial field of view for several gratings are shown. The 830 line pairs/mm grating was used in most studies due to its high efficiency and sufficient field of view.

Grating period (line pairs/mm)	Spectrometer Resolution δλ(nm)	Pixel Sampling Rate δn (nm)	Axial Field of View (μm)
600	0.192	0.219	370
830	0.139	0.148	550
1200	0.096	0.083	980

Table 3.1: Properties of OCT instrument designs based on available gratings.

Axial field of view can be easily altered in OCT spectrometer design allowing the instrument to be modified for imaging needs. However, the actual depth of imaging within a sample will be dominated by the depth-dependent signal fall-off, which is discussed in more detail in section 3.2.2. Briefly, sample-dependent attenuation, the depth of focus of the objective, and spectrometer performance will govern the depth of imaging achievable in a given OCT instrument. Sample attenuation of light will be based on the absorption and scattering properties of the particular tissue. Hemoglobin and melanin are the main chromophores in tissue which have non-negligible absorption coefficients. In the biological applications discussed in this thesis, hemoglobin and melanin content are minimal, leaving scattering as the main source of attenuation. As was discussed in section 2.2.1, light scattering in the visible regime is generally high in tissue on the order of 100 cm^{-1} and with a mean free path of 100 μm. The depth of imaging in a sample in OCT is typically limited to approximately 2-3 times the mean free path depending on the position of focus and the system sensitivity. With this length in mind, the depth of focus of the objective will provide highly uniform illumination over this range. Spectrometer performance can be optimized for the desired depth of imaging, however, extending the axial field of view by increasing the spread of the spectrum will result in less power per pixel, requiring higher source intensity. As a final note, large axial field of view can also be desirable for ease of system alignment, imaging of irregular surface profiles, and imaging of low-scattering materials.

The optical design of an OCT system will have significant consequences on system performance. Several aspects of the OCT design are inherently linked and thus it is almost impossible to alter one parameter alone. Despite this interdependence, once an application or target tissue has been determined, the design may be optimized for maximum signal intensity over the desired depth range of imaging. Given the high scattering of tissue, a system with a lower axial range of imaging was constructed to reduce the number of pixels used in the spectrometer which reduces the amount of power needed from the light source to attain high signal levels. As will be discussed further in Section 3.2.2, the system was optimized to image over a range of approximately 400 μm in tissue.

3.1.2 Hardware Interfacing and Image Acquisition

Advances in high-power, broadband sources and ultra-fast detectors have allowed OCT to become a powerful technique due to the high frame-rates which can be achieved. Typically, FD-OCT

incorporates a line-scan or small area camera. A single row of pixels is sufficient to produce a single A-line depth profile of a sample. A mosaic of A-lines comprise a volume, meaning that the rate of imaging is limited by the scan-speed of the optics, the frame-rate of the detector, and the throughput of the system/source power. The systems presented in this dissertation were designed with only *ex vivo* use in mind, so optical power incident on the sample was limited only to amounts which would not cause thermal damage to the samples.

To maximize FD-OCT frame rate, a high-speed camera was ideal. Two high-speed line cameras were used in the construction of all instruments in this dissertation: a true line-scan e2v em4 (Aviiva) and a small-area Teledyne Dalsa Piranha (HS-82-04K80, Teledyne-Dalsa). Both cameras had the same pixel size of 14 μm and were compatible with a Camera Link interface. To manage data throughput, a Frame Grabber card was necessary for use with each camera. To maximize frame-rate and bit-depth, the Camera Link medium configuration was used for 12-bit image encoding.

When using a Frame Grabber, a custom camera configuration file was required for operation. The configuration file set several parameters and is typically used to minimize on-board processing or data operation before read-out to computer RAM. Settings such as the area of interest on the sensor, gain, hot pixel correction, and integration time were either turned off or minimized in order to maximize frame-rate. Exposure time was increased when necessary to allow for greater signal intensity from the sample arm.

Image acquisition was performed in Matlab (Mathworks) via the Image Acquisition Toolbox. The Matlab interface was chosen due to its compatibility with other hardware and ease of access for users with little to no programming experience. The interface with the camera configuration file allowed for several parameters to be adjusted once the camera was initialized in Matlab. A custom GUI and image acquisition script was written to allow for several key functionalities. Memory pre-allocation, scan dimension, exposures per scan, and scan direction were all directly controlled within the custom Matlab GUI without requiring the camera to be re-initialized. Additionally, serial commands could be sent to the camera from Matlab to temporarily adjust certain parameters in the configuration file, such as exposure, without the need to halt acquisition and re-initialize the camera. The Matlab GUI was also capable of the necessary image processing and image display detailed in Section 3.2.

Scanning was achieved by a pair of galvo mirrors and a laser scanning microscope objective. The

galov mirrors adjust their angle based on an input voltage from a DAQ (National Instruments). Initial configurations changed the voltage by discrete values corresponding to multiples of the diffraction-limited spot size. In this configuration, the camera was triggered at each new position to acquire an image. To decrease mechanical wear on the mirrors, increase image speed, and preserve this lateral sampling, a sinusoidal scanning wave was implemented. In this configuration, the camera was programmed to take a set number of frames and triggered at the start of the sinusoid. The sinusoid was modified such that each successive frame at a constant exposure was separated by no more than half the diffraction-limited spot size, according to Nyquist sampling. The result is an image which is elongated at the either end of the scanning waveform but is sufficiently oversampled and can be easily corrected. Additionally, it was found that the central region of the sinusoid was nearly linear and required little in the way of image correction. Finally, the waveform was also modified to include a "zero-padding" delay on either end in order to facilitate data readout, mechanical movement of optical components, or other processing steps.

3.2 OCT Image Processing and Reconstruction

A Fourier transform of the interferogram produces an intensity profile in depth for the point at which the backscattered light is collected, which is referred to as an A-line. A reconstruction of interferograms for a one-dimensional scan of the sample leads to a two-dimensional image referred to as a B-scan and is analogous to a conventional ultrasound tomograph. Finally, a reconstruction of each interferogram in a two-dimensional scan provides a full volumetric image of the sample, referred to as a c-scan.

The use of the Fourier transform to recover depth information is not without its complications. The first consideration is the units of the function before the Fourier transform. The Fourier transform produces a function of inverse units compared to the initial function. Thus, to obtain units of distance for the Fourier transform into object space, the function in frequency space must possess units of inverse distance. This can be accomplished by converting λ to k where $k = 2\pi/\lambda$. Due to this transformation being nonlinear however, the first of many challenges in OCT image reconstruction is presented: precise spectral calibration. The second challenge is to account for the spectral shape of the source used, which will contribute greatly in the low-frequency components of the Fourier transform. These pixels can be removed from the final image, however, the contributions

of the source shape will interfere with further processing in sections 3.2.1 and 3.3.2.

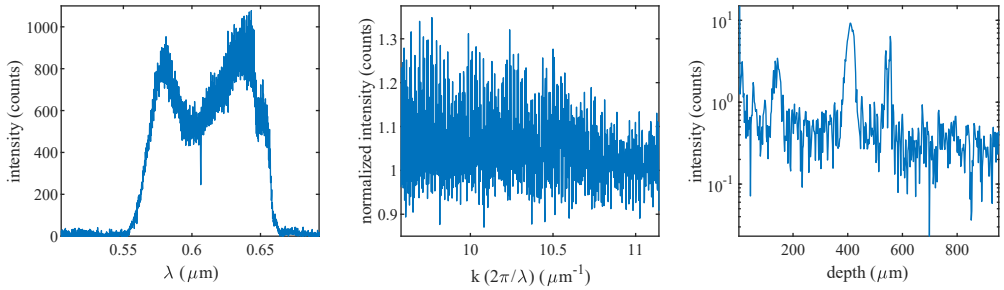

Figure 3.2: Left: Interference fringes as a function of wavelength. Middle: The fringes after correcting for spectral shape and interpolating into wavenumber. Right: The intensity as a function of depth, the result from the Fourier transform of the center plot.

3.2.1 Dispersion Compensation

A full description of a light wave contains a signal amplitude and complex phase, see Eq. 2. However, using a CCD or CMOS detector to measure interference will only yield a real signal of the form in Eq. 34. The complex signal can be conveniently restored using a Hilbert transform, which will a real part equal to the original (cosine) function and an imaginary part equal to the 90° out of phase equivalent (sine) function. The utility of this transform is that the absolute value of it generates the envelope of the function, A_0, and the angle of the function (the arctangent of the ratio of the imaginary to the real portions) is equal to the phase, ϕ.

$$E_{det} = A_0 cos(i\phi) \tag{34}$$

Determining the phase of the OCT interferogram has a number of uses, including determining the birefringence (see Section 2.5.2), OCT angiography, and dynamics. Another common use of the Hilbert transform and phase determination is in dispersion compensation [83]. At a minimum, the scanning objective of the OCT sample arm will contain a thickness of glass that will introduce dispersion into the beam that is not present in the reference arm. Typically, physical dispersion compensation is performed by placing a piece of glass with equal thickness and no focusing power in the reference arm. While this will mitigate most system-dependent dispersion, the scanning of the sample must also be considered. Liquid immersion and the sample itself will introduce dispersion that will ideally be corrected for to maximize image contrast.

Chromatic dispersion has been well-characterized previously and follows the general form of Eq. 35, where the ideal phase $\phi(z,k)_{ideal}$ for a single reflector is a linear function with k for a given z [96, 97]. This is confirmed conceptually where a single reflector produces a single sinusoid in the interferogram which accumulates constant phase. Dispersion, $a_{1,2}$, introduces non-linearities into the phase and produces a blurred image. Several approaches exist to estimate the dispersion of a system and it can be seen in the most straightforward way by imaging a single glass/mirror reflector. A fit of $\phi(z,k)_{disp}$ provides an estimate of $a_{1,2}$, however these will only account for the system dispersion. Currently, determining and mitigating sample-dependent dispersion is an area of constant research and falls outside the scope of the work presented in this dissertation. Simply, a custom GUI interface was developed in Matlab to allow for manual estimation of sample dispersion from user feedback of images. Estimated parameters were stored and could be retrieved and applied to several samples to ensure repeatability and consistency during analysis.

$$\phi(z,k)_{disp} = \phi(z,k)_{ideal} + a_1 k^2 + a_2 k^3 \tag{35}$$

These effects are encapsulated in Figure 3.3, which shows the impact of dispersion on the accumulated phase of a single reflector, the corresponding interferograms, and FD-OCT images with and without dispersion.

3.2.2 Correcting the Depth-dependent Signal Fall-off

This system was designed to optimize the imaging over a short range in tissue of approximately 400 μm. A grating with 830 line pairs/mm was selected to give a sufficiently large axial range of imaging while still being compatible with 1 inch diameter optical components and the camera. A 1200 line pairs/mm grating was found to disperse the spectrum beyond the edges of a 1 inch lens and required 2 inch diameter optical components in the spectrometer which presented worse chromatic performance. When used with a 100 mm focal length lens to focus onto the camera, this combination produced a spot size roughly equivalent to the camera pixel size. The resulting sampling of the spectrum by the lens and camera was closely matched to the grating resolution, providing the reasonable depth-dependent fall-off (see variable ζ in Eq. 17). The 830 line pairs/mm grating also produces a reasonable fall-off when used with the 5 mm galvo mirrors and 0.06 NA

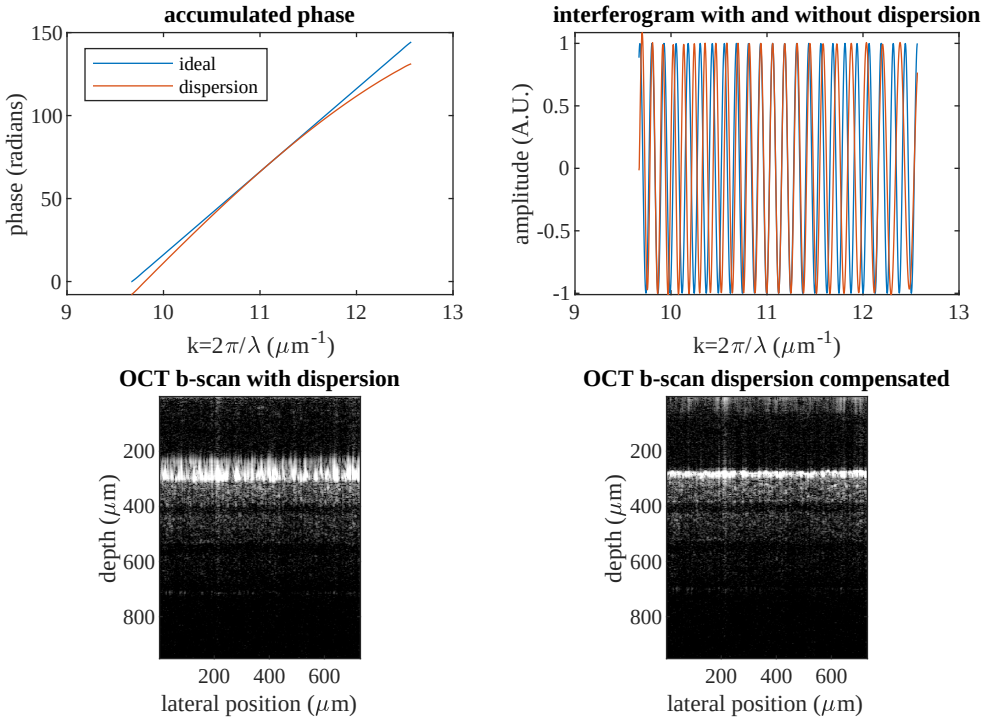

Figure 3.3: Top left: The accumulated phase in the interferogram without (blue) and with (red) dispersion included. The inclusion of dispersion produces a nonlinear function of $\phi(z,k)$ for a single reflector (fringe frequency). Top right: The interferogram fringes without (blue) and with (red) dispersion, generated from the accumulated phase in the top left panel. Bottom left: An OCT B-scan of layered take with dispersion. Bottom right: The same image after dispersion compensation.

objective. The depth of focus for the objective was approximately 300 μm on one side, which appears inefficient until the focus is moved into the sample, which allows more even illumination.

These parameters are best summed up by Figure 3.4, which reproduces Figure 2.3 for the case in this instrument when the focus of the objective is at zero phase delay. More importantly, Figure 3.4 also includes the case for the focus of the objective being placed approximately 250 μbelow the top of the image space. This is ideal in VIS-OCT due to the presence of the autocorrelation image (the interference of the sample with itself) which is typically a corrupting factor when high signal intensity from the sample is achieved and when the sample has higher scattering. The attenuation of this image is, in fact twice the optical scattering coefficient of the real OCT image, and thus attenuates below the noise floor much more quickly. As can be seen, the intrinsic depth-dependent fall-off in this system is acceptable over a depth of almost 400 μm, making this system ideal for the studies proposed in this dissertation.

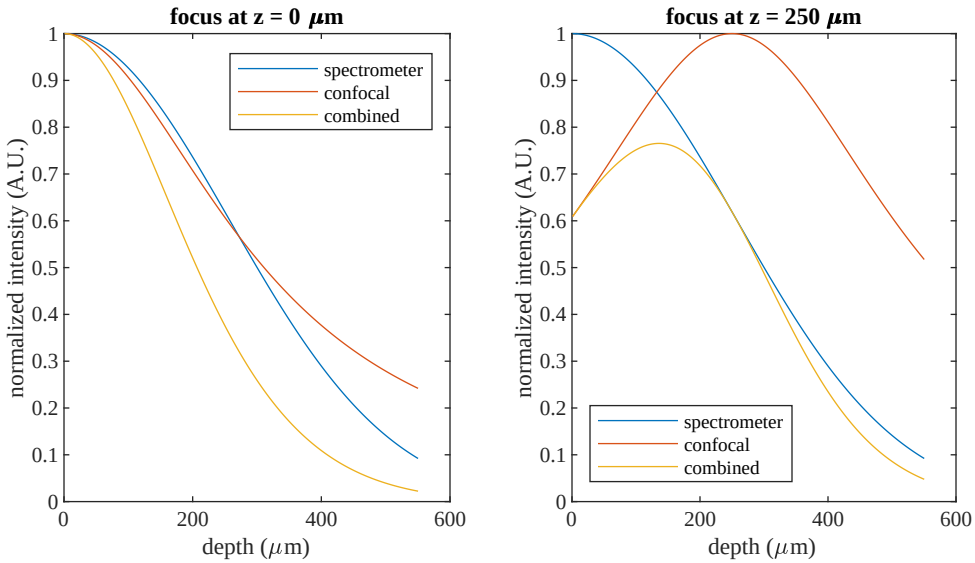

Figure 3.4: Similar to Figure 2.3 which was for a hypothetical system, here we see the same equations applied to the actual VIS-OCT system. Left: Depth-dependent fall-off when the focus at 0 phase delay. Right: For focus at 250 μm.

3.2.3 Determination of Optical Properties in VIS-OCT

Scattering of the sample can conveniently be determined by fitting the decay in the intensity as a function of depth, as shown previously in Section 2.5.1. Reprinting Eq. 26 here as Eq. 36 and expanding demonstrates more directly how the FD-OCT signal can be fit to determine μ_s.

$$\begin{aligned} I(z)^2_{OCT} &= 4I_0^2 R\mu_b(z) exp\big(-2zn\mu_s(z)\big) \\ ln\big(I(z)^2_{OCT}\big) &= ln\big(4I_0^2 R\mu_b(z)\big) + \big(-2zn\mu_s(z)\big) \\ \mu_s(z) &= \frac{ln\big(I(z)^2_{OCT}\big) - ln\big(4I_0^2 R\mu_b(z)\big)}{-2zn} \end{aligned} \tag{36}$$

Fitting may be performed easily in either the log-space with a linear fit for the familiar form $y = mx + b$ or with an exponential function in linear-space of the form $y = a \times exp(-bx)$. However, in either case, it is critical that noise be removed and depth-dependent fall-off be corrected before fitting. Other considerations exist in the image processing such as detecting the image surface to create a flat profile, lateral and axial averaging of pixels, and noise suppression/thresholding. Surface location was best performed in linear-space using a derivative of the image and an intensity

threshold. The derivative of the image is greatest at the transition from low intensity noise values to high intensity values from the surface of the tissue. The use of a threshold which sets low noise values to some arbitrarily low noise floor (on the order of 10^{-9}) further increases the slope. Lateral averaging of pixel values can reduce the noise and prevent streaks from specular reflection

3.3 VIS-OCT Improvements: Noise and Polarization Sensitivity

Several improvements and functional additions were incorporated into the VIS-OCT instrument to enhance its ability to interrogate tissue optical properties. The noise correction process described in Section 3.3.1 was developed with the help of Dr. Zachary Simmons and was published in [98].

3.3.1 Noise and Multi-Channel Detection

Typically, FD-OCT is designed to fill the complete width of the detector to maximize spectral resolution and bandwidth. While vis-OCT is capable of large bandwidth, its high scattering reduces the axial range of imaging. This, in turn, limits the number of pixels needed on a detector to approximately 1200. Recent advances in high-speed line-scan technology have led to the development of multi-line line-scan cameras. These detectors consist of between 24 and 48 rows of 2048 or even 4096 pixels that can be read out in an area mode or in a time-delay and integration (TDI) mode. The Piranha series from Teledyne Dalsa is capable of up to 110 kHz line rates in TDI mode, or approximately 2 kHz in area mode. The unique geometry of this detector allowed for multiple spectra to be recorded simultaneously. Multiple spectra of over 1000 pixels could be recorded along the same row or separated across multiple rows depending on the desired integration time and optical configuration. Depending on the spectrometer design and system alignment, up to 16 spectra could be recorded simultaneously.

The first implementation of this multi-channel technique was used to reduce noise in a slow repetition-rate supercontinuum source. Supercontinuum sources are ideal for OCT in that they generate a milieu of wavelengths with each pulse for as of yet unmatched bandwidth [99]. However, the spectral broadening is dependent on the duration of the pulse, which leads to the generation of relative intensity noise (RIN) which scales proportionally to intensity [100, 101, 102, 103]. Ideally, OCT systems are shot noise-limited to maximize SNR since shot noise will scale proportionally to the square root of intensity [101, 102]. The total noise in OCT is described by Eq. 37, where the

read noise does not scale with source intensity [101]. This definition of noise shows that for a shot noise limited system, increasing intensity by a factor of 2 will increase the SNR ratio by a factor of $\sqrt{2}$ [101, 102]. However, for a system which includes RIN, the increase in intensity will not increase the SNR [101, 102].

$$\sigma_{total} = \sqrt{\sigma_{read}^2 + \sigma_{shot}^2 + \sigma_{RIN}^2} \tag{37}$$

Conventionally, FD-OCT uses superluminescent diodes (SLDs) since they can offer bandwidth of approximately 60 nm in the NIR range and are an approximation of a continuous source, meaning they are shot noise limited. However, few options exist in the visible regime that have sufficient bandwidth to take advantage of the high potential resolution of the visible regime. Supercontinuum sources offer high bandwidth and power, but possess the aforementioned RIN [104, 105, 106].

Typically, RIN is mitigated by increasing source repetition rate and/or camera exposure to increase the number of pulses acquired in each frame. However high repetition rate sources can have significant cost and typically have a large footprint. As an alternative to high repetition rate sources, a low-cost and compact supercontinuum source with a low pulse rate of 20 kHz was used to illuminate a single pulse per frame acquisition of the fast frame-rate Piranha. To reduce the RIN component, a secondary reference spectrum was used to normalize the pulse-to-pulse variations in the supercontinuum source, referred to as the normalization spectrum to alleviate confusion with the FD-OCT reference arm used for interference. In order to acquire a second spectrum on the detector, the vis-OCT system in Figure 3.1 was modified in two separate ways. The configurations shown in Figure 3.5 allowed the normalization spectrum to be displaced along the dispersion axis of the grating such that the spectra were along the same row of pixels or perpendicular to the direction of dispersion such that the spectra were on two separate rows of pixels. Validation experiments were performed with no sample present, meaning the FD-OCT reference spectrum was compared only to the normalization spectrum. While both schema were capable of noise reduction, scheme A was preferred due to ease of alignment and a more rigorous matching of grating and lens angle and focus.

Spectra could be aligned roughly using shape features of the spectrum, including sharp drop outs and peaks in intensity across wavelength. This alignment was performed with a combination of

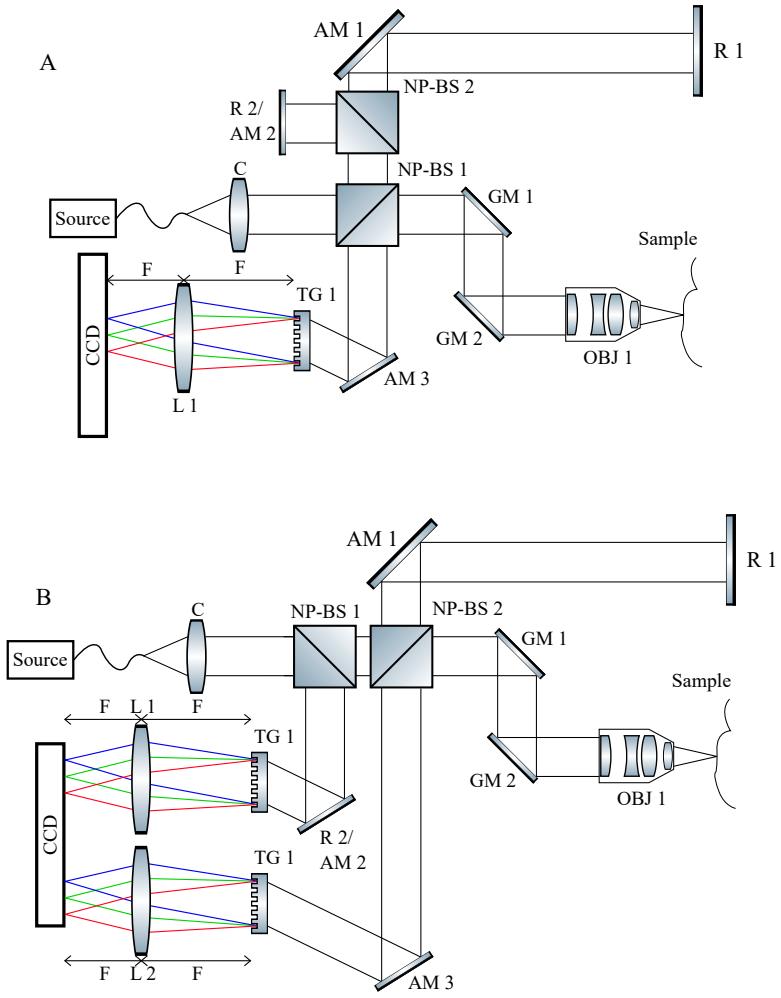

Figure 3.5: Normalization spectra can be collected in two ways. In (A), a second nonpolarizing 50:50 beamsplitter (NP-BS 2) is inserted into the reference arm, and double reference mirrors provide separation of normalization and reference spectra orthoganal to the spectral line for collection using an area sensor. In (B), a 90:10 nonpolarizing beamsplitter (NP-BS 1) upstream of the interferometer is used to direct light to a duplicate identical spectrometer for lateral separation of normalization and reference spectra using a single line scan detector.

manual alignment on the center and digital calibration of spectra to correctly match pixels between spectra. Once the rough alignment was complete, the correlation of matching pixels over a series of frames was determined. Shot and read noise will be uncorrelated between frames, while the RIN will be correlated between spectra so long as the spectral sampling (or binning into each pixel) is equal. Sub-pixel alignment, while difficult, can be achieved and high correlation values for each

pixel pair were achieved. This process is visualized in Figure 3.6, where the intensity of a single pair of pixels is shown for each frame and the correlation across the full spectrum is shown. To validate the correction procedure, data was acquired in the NIR in an identical band to an available SLD centered at 860 nm (SuperLum, Carrigtwohill, Ireland). To compete the comparison in both the NIR and visible regimes, an 80 MHz supercontinuum source was also used at long integration times. While not suitable for imaging *in vivo*, the long integration times of 1-2 ms allowed sufficient integration for the 80 MHz supercontinuum to average out all RIN.

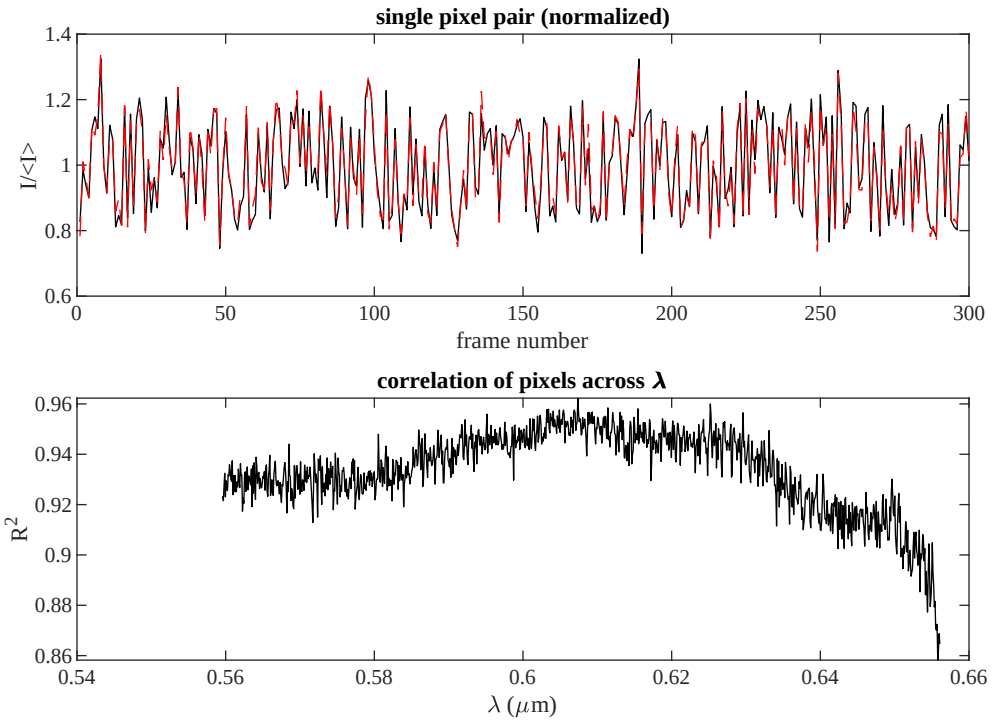

Figure 3.6: Top: Normalized intensity of a single pixel from each of the spectra corresponding to the same wavelength bin and generated by a single pulse captured in each frame. Bottom: The correlation of intensity for each matching wavelength bin in the spectra.

Noise characterization of sources was performed using a photon-transfer curve (PTC). A PTC plots the log_{10} of the noise (standard deviation) against the log_{10} of the mean signal over a number of frames (or pixel readouts). The slope of the PTC can thus readily describe the noise characteristics of the camera when the source is shot noise limited. The same plot can also be used to describe the noise characteristics of a non shot noise limited source if the camera parameters are known. Figure 3.7 (left panel) includes a PTC of the SLD and both supercontinuum sources, the slow

repetition rate source with one pulse per image and the fast repetition rate where the RIN has been averaged out. The RIN and shot noise are apparent in the slopes of the log-log-scale plots, where the slope is equal to the exponent. The shot noise limited sources (the SLD and 80 MHz) have a slope equal to roughly 1/2, indicating the noise is proportional to the square root of intensity. Meanwhile, the 20 kHz source has a slope approximately equal to 1, indicating the presence of RIN. The right panel of Figure 3.7 demonstrates the noise of each pixel according to wavelegnth. This demonstrates that the noise is not wavelength dependent and how it impacts the FD-OCT signal, as it contaminates the interferogram and reduces the maximum fringe SNR.

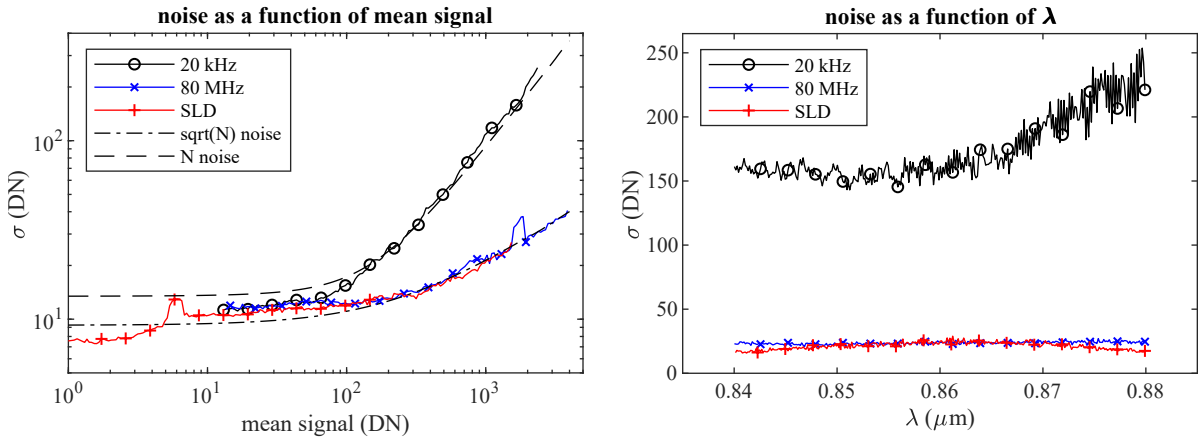

Figure 3.7: Left: The PTC of the supercontinuum 20 kHz (black), supercontinuum 80 MHz (blue), and SLD sources which demonstrate the presence of RIN (slope of approximately 1 on a log-log scale) in the 20 kHz but only shot noise (slope of approximately 1/2 on a log-log scale) in the 80 MHz and SLD sources. Right: The noise as a function of wavelength for each source which demonstrates how the OCT spectrum may be impacted by the presence of noise.

The RIN was mitigated in the 20 kHz source by creating a correction factor using the normalization spectrum. Dividing the normalization spectrum by its mean in time created a function which oscillates about unity that indicates, for a particular frame, if the pulse intensity was higher or lower for each pixel in the frame. Dividing the FD-OCT reference spectrum by this correction factor eliminates the frame-to-frame variations without impacting the overall signal intensity. Ideally, this method would leave only the shot noise and read noise in the signal, but there will be an additional factor of 2 in the shot noise since this method divides one signal by another. This method

is summarized by Figure 3.8, which shows the FD-OCT reference and normalization spectra for a single frame, the derived correction factor for that particular frame, and the results of using the correction factor.

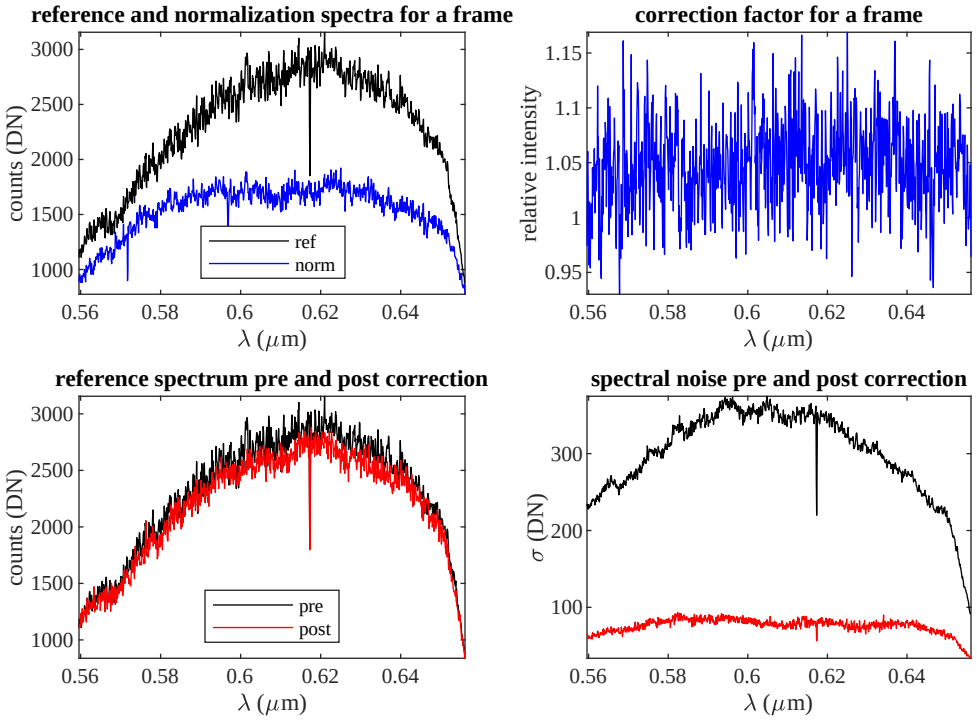

Figure 3.8: Top left: Pulse correction is performed by first isolating the reference (black) and normalization (blue) spectra. Top right: The normalization spectra is used to compute a correction factor by dividing each frame by the mean in time for all frames collected, which yields a signal oscillating about unity. Bottom left: the reference spectrum (black) is then corrected (red) for the pulse-to-pulse variations between frames. Bottom right: the noise from the uncorrected (black) and corrected (red) spectra across the bandwidth used for VIS-OCT imaging. The noise is reduced by nearly a factor of 5 across nearly the full range of the spectrum.

Looking at the correlation of pixel pairs, only sources with RIN present possessed meaningful correlation. This agrees with theory in that shot noise and read noise are not correlated. Shot noise is the result of discrete random digitization errors and is an independent event for a given pixel, meaning it will have no correlation to another element in the detector. Indeed, when comparing the correlation of all sources, the data suggests that the presence of RIN leads to the correlation. Furthermore, it is hypothesized that the driving force in this method is the temporal correlation of RIN. Greater correlations directly showed increasing efficacy of the normalization method as the initial noise, σ_i, decreased by a factor of nearly 5 at the highest correlations (see Figure 3.9).

It was also observed in the PTC that this correction method lead to a significant noise reduction and, in fact, approached the theoretical limit (shot noise divided by shot noise). These findings, detailed in Figure 3.9, demonstrate the viabilty for this method to eliminate RIN by using single-pulse imaging. The performance of the pulse correction method was superior in the visible regime, which was attributed to the spectral resolution of the visible system. Shifting the optics to the NIR worsened the resolution of the grating (see see discussion of Eqs. 13, 14, and 15 in Section 2.4.2) which increases cross-talk between channels.

Finally, this correction method was applied to FD-OCT imaging of a single layer of tape as shown in Figure 3.10. The sample arm was reintroduced with a single tape layer mounted on a glass slide. Images with VIS-OCT were taken with both the 80 MHz and 20 kHz sources and the correction method was applied identically as described above. The noise reduction is noticeable in the 20 kHz image and in the mean intensity plots of the image. An apparent increase in OCT image SNR is apparent due to the lowering of the noise floor while maintaining signal intensity, rather than an overall signal and noise decrease. Images are displayed on an identical dynamic range for optimal comparison. While not at the level of a shot noise limited system, this multi-channel technique of noise reduction required very few optical components and was able to significantly improve the performance of a cost-effective, portable visible-light supercontinuum source. Furthermore, because the correction method is based on correlation, and the correlation is generated by RIN, there is potential for this method to be applicable to the 80 MHz source when operated at short integration times.

Significantly, the resulting study [98] demonstrated the utility of multichannel detectors and provided the groundwork for using a similar detection scheme in polarization-sensitive FD-OCT. Rather than establishing a secondary channel for noise reduction, polarization-diverse optics were used to establish orthogonal polarization imaging channels on a single detector.

3.3.2 Polarization

Polarization-sensitive FD-OCT (or PS-OCT) relies on detection of diverse polarization states in order to characterize the sample. Several schema exist to accomplish polarization-diverse detection [107, 91, 93, 57] but almost all are based on a polarization-discriminating element such as a beamsplitter. The vertical and horizontal components are redirected from the beamsplitter to ei-

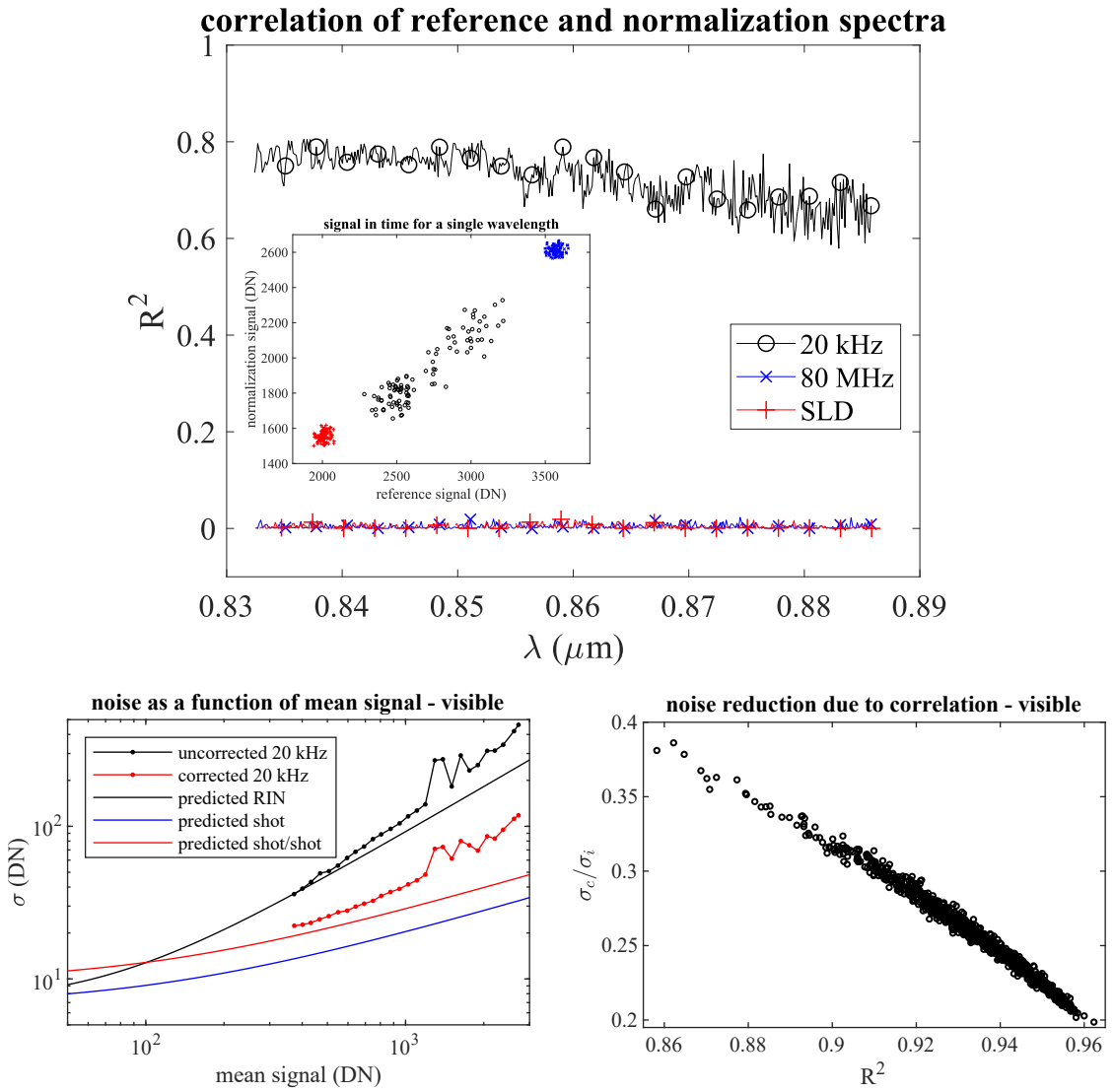

Figure 3.9: Top: The correlations across the bandwidth from the 20 kHz (black), 80 MHz (blue), and SLD (red) demonstrate correlation only in the 20 kHz source, which agrees with the lack of temporal correlation in shot noise. Bottom left: The PTC of the 20 kHz source before (black) and after (red) correction. Real vaues of the PTC are plotted along with the theoretical RIN, shot noise, and the predicted value for one shot noise limited signal divided by another shot noise limited signal which was the theoretical maximum correction which could be performed. Bottom right: The noise correction as a function of correlation demonstrates that as correlation increased, there was a greater reduction of noise.

ther identical detectors, a pair of balanced photodetectors, or the same detector. This dissertation presents a novel variation of this scheme which not only uses the same detector, but also a common transmission grating and lens with a highly common path and does not rely on frequency encoding

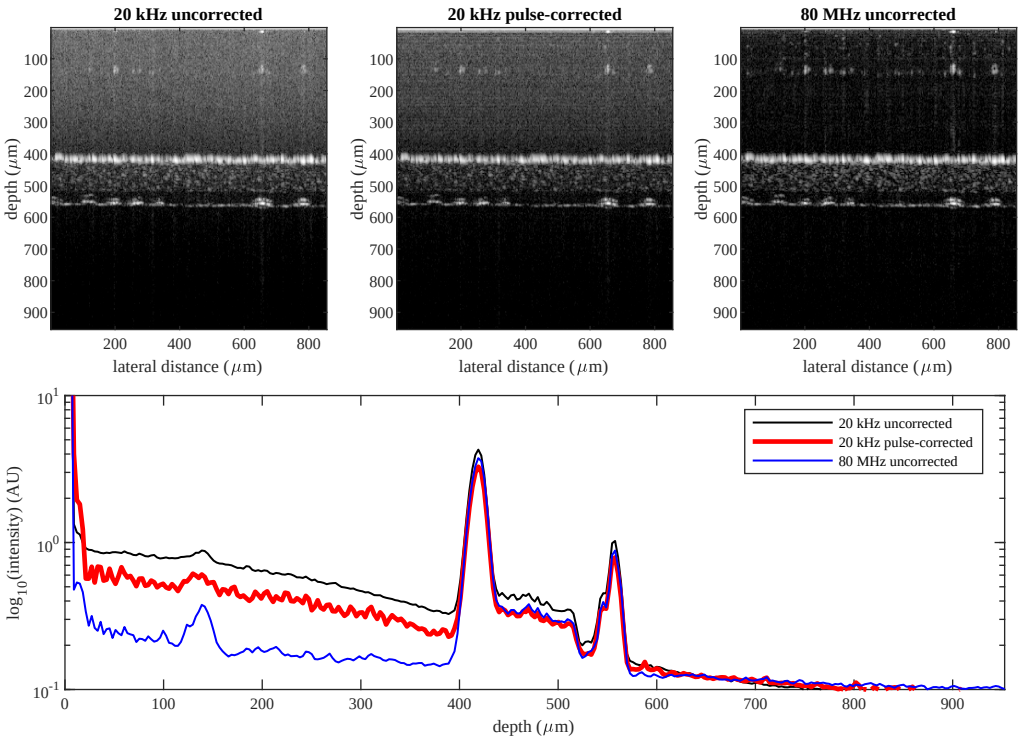

Figure 3.10: Top row: VIS-OCT B-scans of a single layer of tape on a glass slide. From left to right: the 20 kHz image without pulse correction, the 20 kHz image with pulse correction, and the 80 MHz image which served as a shot noise limited image for the camera settings used in this study. Bottom, mean A-line profiles for each image which show the 20 kHz without pulse correction (black), the 20 kHz with pulse correction (bold, red), and the 80 MHz shot noise limited (blue). The pulse correction clearly decreases the noise floor without significantly impacting the image intensity.

to separate the images [107].

Modifying the system configuration of Figure 3.5A, a pair of polarization-sensitive beamsplitters were incorporated between the Michelson beamsplitter and the transmission grating of the spectrometer to create the system shown in Figure 3.11. The use of fold-mirrors and the second beamsplitter allowed the beams to be displaced orthogonal to the direction of dispersion by the grating and to be focused onto two rows of pixels on the Piranha detector. This has the benefit of both balancing the signal amplitude and more easily matching the spectral sampling. Spectral sampling can be matched by assessing the pixel-pair correlation outlined in Section 3.3.1 and operating the laser at an integration time with RIN present.

Input polarization was controlled by a Glan-laser prism which acted as a linear polarizer in a rotation mount. The axis of the Glan-laser was set to 45° so that the reference arm would not need

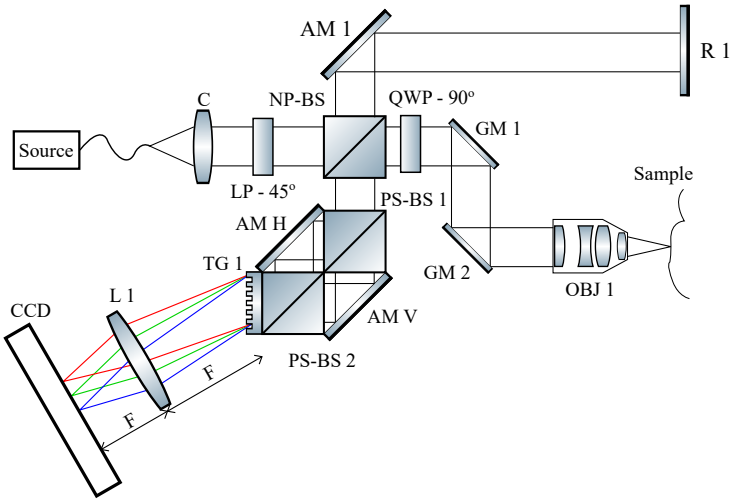

Figure 3.11: The multi-channel OCT system was converted to include polarization-diverse detection. Similar to Figures 3.1 and 3.5, light is coupled into the collimation package (*C*) before being linearly polarized by a Glan-laser polarizer (*LP*) oriented at 45°. The reference consists of an adjustable mirror (*AM 1*) and a reference reflector (*R 1*), which in this case was a piece of wedged glass. The only modification to the sample arm was a quarter-wave plate oriented at 90° to produce circularly polarized light which is scanned by the galvo mirrors (*GM 1* and *GM 2*) across the objective (*OBJ 1*). Polarization-diverse detection was achieved on a single detector by using two polarization sensitive beamsplitters (*PS-BS 1* and *PS-BS 2*) with an adjustable mirror to steer the horizontally and vertically polarized spectra (*AM H* and *AM V* respectively) through a single transmission grating (*TG 1*) and spectrometer lens (*L 1*) to displace the spectra orthogonal to the direction of dispersion on the detector (*CCD*).

additional optics. In the initial setup, the sample arm contained a quarter-wave plate oriented at 90° in order to convert the linear 45° polarization to circular. Circular polarization was chosen first as it has been show to increase penetration depth and when given thought to integration in systems that will be discussed in Section 6.2 which require circular polarization input. Polarization diverse detection was achieved using multiple rows and the area mode of a Piranha camera.

Polarization analysis was initially performed as described in Section 2.5.2. As brief reiteration, the complex-valued Fourier transform was preserved and its absolute value determines the envelopes $A_x(z)$ and $A_y(z)$, the arctangent of the ratio of these envelopes directly provides the accumulated retardance, $\delta_s(z)$, provided the Fourier-based reconstruction is performed correctly. The optical axis of the sample is determined by the phase difference of the orthogonally polarized complex-valued Fourier transforms, which can be retrieved directly by taking the arctangent of each. These

data are not immediately useful because, at low image intensities, noise will dominate the behavior of these functions and render values with no physical meaning. Therefore, an intensity threshold of the OCT image was used to filter out these pixels.

Accumulated retardance and optical axis values were determined in chicken breast, see Figure 3.12. These data demonstrate the ability of the instrument to measure polarization properties of tissue, but there were technical limitations and some caveats. The main limitation was the alignment on the spectra. Aligning the spectra and recovering two images were not sufficient to cancel out the $R(z)$ terms in Eq. 29. The sub-pixel alignment, interpolation into k-space ($2\pi/\lambda$), and dispersion compensation all needed to be performed precisely to recover the correct value of $R(z)$ in each polarization channel. Misalignment and poor reconstruction of images will contribute to the noise of the accumulated retardance and optical axis images. Finally, when the precise alignment is obtained, the accumulated retardance and optical axis values obtained are ambiguous at values of $\pi/2$ and π respectively. These ambiguities are due to the operations which retrieve their values. Methods will be discussed below which use a more complex dual-input polarization to remove this ambiguity.

Initial instrument design showed little birefringence signal in tape phantoms. However, the accumulated retardance of tape is low over less than 5 layers. In order to demonstrate birefringence measurement equivalent to that of other groups, chicken breast muscle was used as a soft validation. Chicken breast is sufficiently birefrignent to cause a 90° phase shift within 100 μm, which allows for multiple oscillations between 0° and 90° to be observed over the approximately 300-400 μm of imaging depth. Optical axis measurements must be performed very carefully since the ambiguity in phase due to processing may distort the true optical axis value. Furthermore, it is well established that the determination of the optic axis is only unambiguous for the first birefringent layer of tissue. Beyond the first layer, a more sophisticated analysis must be used in order to resolve the true optical axis orientation. The soft validation of chicken breast demonstrates this well by the optical axis appearing to change with depth due to artifacts in processing the phase of the complex Fourier transforms. Due to this limitation, optical axis is typically only measured quantitatively when careful *a priori* knowledge of the sample or controlled conditions are used. These data are demonstrated in Figure 3.13 which shows the triangle waveform from the ambiguous determination of accumulated retardance, $\delta_s(z)$ and the difficult to isolate optical axis, $\theta_{OA}(z)$.

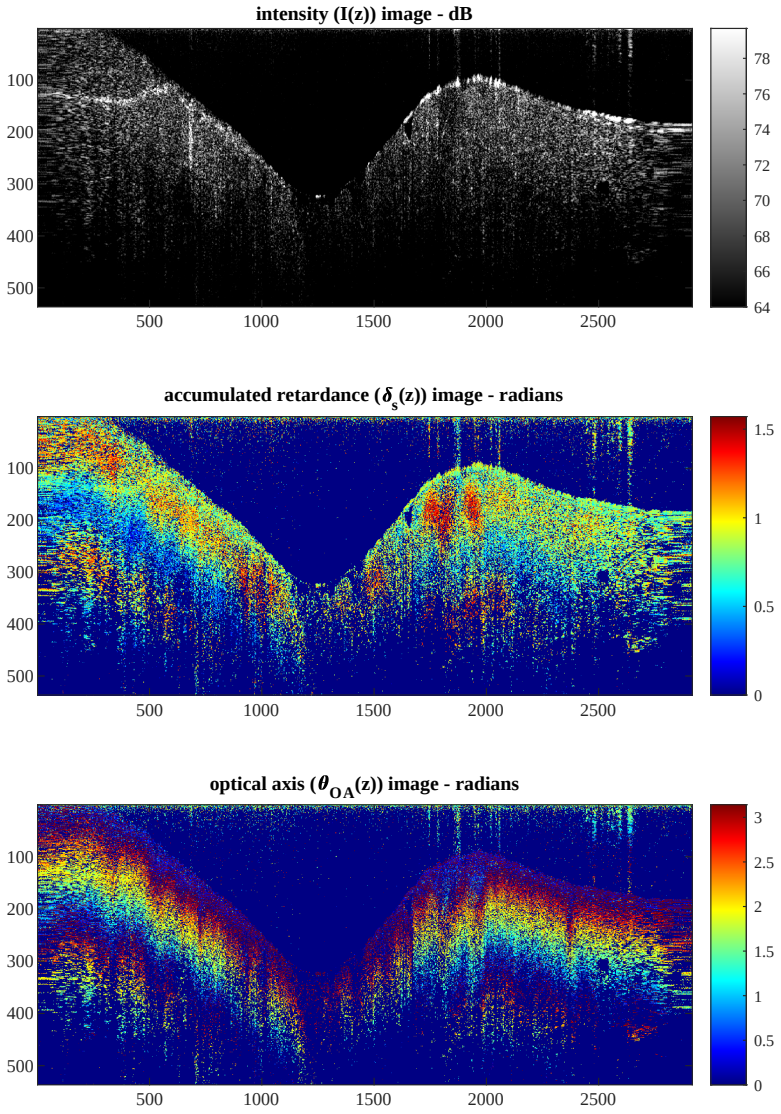

Figure 3.12: Top: Intensity image of chicken breast which shows a fairly homogeneous structure. Middle: Accumulated retardance image showing the birefringent properties of the tissue. Bottom: Optical axis orientation image which contains several banding artifacts due to multiple oscillations in the accumulated retardance. These artifacts present the optical axis as constantly rotating, which cannot be the case in tissue, thus without a more precise validation method, this measurement presents little use.

As discussed in Section 2.5.2, the accumulated retardance can be converted into the retardance per pixel using the local derivative. These values will be noisy, due to the inherent noise of the

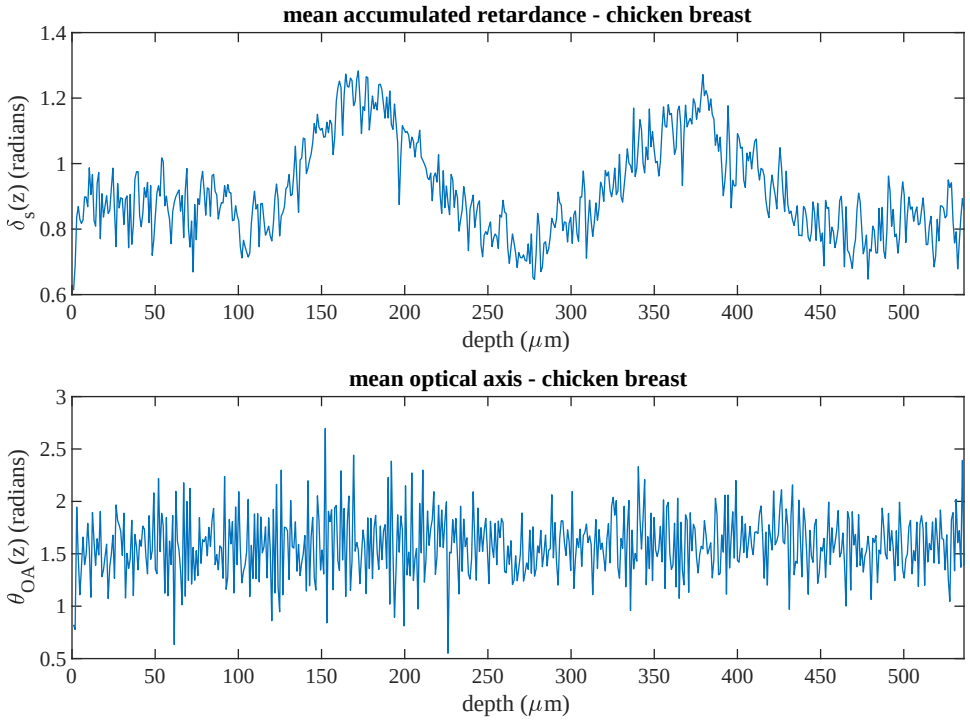

Figure 3.13: Top: Accumulated retardance. Bottom: Optical axis orientation. Data are taken as a lateral average of values in Figure 3.12 beginning at approximately 1900 μm and spanning across approximately 50 μm.

image. Careful use of blurring, however, can reduce the noise at the cost of resolution in the image but can yield meaningful results. In the case of chicken breast, the derivative of the accumulated retardation image was blurred and used to provide color to the OCT intensity image and an intensity threshold mask was used to further reduce the impact of noise. The result, shown in Figure 3.14, provides an pixel intensity image of the OCT B-scan with color indicating the per pixel retardation. This processing is able to reveal features that are not as apparent in either the intensity or accumulated retardance images.

Using this method, the sensitivity of accumulated birefringence will depend on the achievable SNR of the polarization-diverse images. The ratio of the images provides the argument of the tangent function and its result gives the accumulated birefringence. This ratio will achieve its maximum and minimum at the peak signal intensity and the noise floor of each image. The noise floor will be limited by read noise, shot noise, any relative intensity noise in the source, and speckle [108, 109, 110]. The signal peak intensity will be related to the system sensitivity.

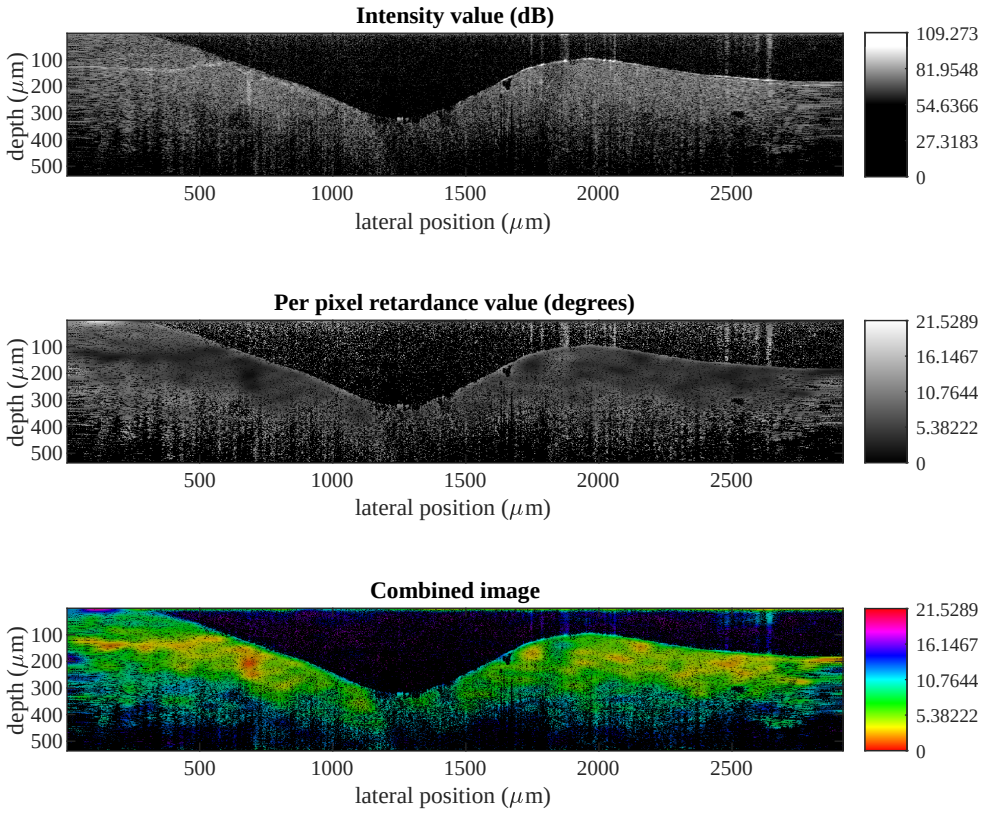

Figure 3.14: Top: OCT intensity image in decibels which is used for pixel intensity. Middle: Per pixel retardance image which is used to generate hue/color. Bottom: The OCT intensity image with the per pixel retardance mapped as color.

The smallest detectable change in signal level has previously been discussed to be dependent on speckle. A chief method to mitigate speckle is to average A-line or B-scan images during acquisition and is a common technique in OCT image acquisition [111]. Using an averaging method that ensures that the speckle fields are uncorrelated, the minimum detectable retardation is on the order 0.06 $^{\circ}/\mu m$ [111].

An alternative method of determining the polarization properties of a sample has been developed extensively Bouma, Tearney, Villiger, Vakoc, and Suter [89, 112, 113, 114]. This method relies on having two input polarizations on the sample which are orthogonal on the Poincaré sphere, a spherical coordinate system which describes the Stokes vector of a wave where the 3 axes of the coordinate system are the Q, U, and V values of the Stokes vector. Simply put, the input

polarizations must have a positive or negative unity value for one of the three values and zero for all others. Conveniently, this can be accomplished easily with a simple modification to the sample arm to flip an equivalent quarter-wave plate at 45° in to the sample path to replace the 90° quarter-wave plate. This can be achieved by modifying the scanning galvo waveform to include a pause before flyback to allow the differently oriented quarter-wave plates to be moved into or out of place. This will produce a co-registered scan of an identical area with orthogonal input polarizations. While this method may be slower than an EOM or other polarization control method, it has the benefit of not manipulating the reference arm and keeping the dispersion between the reference and sample arms constant, allowing the use of a single set of dispersion compensation coefficients to be used for both polarization states.

This dual-input method uses the differences in the input states to compute the accumulated birefringence and the optical axis orientation with no ambiguity. This method can be further refined using a windowing process in the spectral domain similar to the method presented in Sections 2.5.2 and 7.1.2 to account for polarization mode dispersion across wavelength. Typically, this solution is employed in fiber-based systems to account for the change in polarization mode due to the movement of the fiber optics during imaging. Identical processing is used here but without spectral binning, as it was found to increase noise without improving performance. Application of the dual-input method to the same chicken breast images results in a similar map of per pixel retardance (see Figure 3.15) and a degree of polarization (DOP) image which expresses the uniformity of the tissue polarization properties, a higher value indicates more uniform tissue polarization.

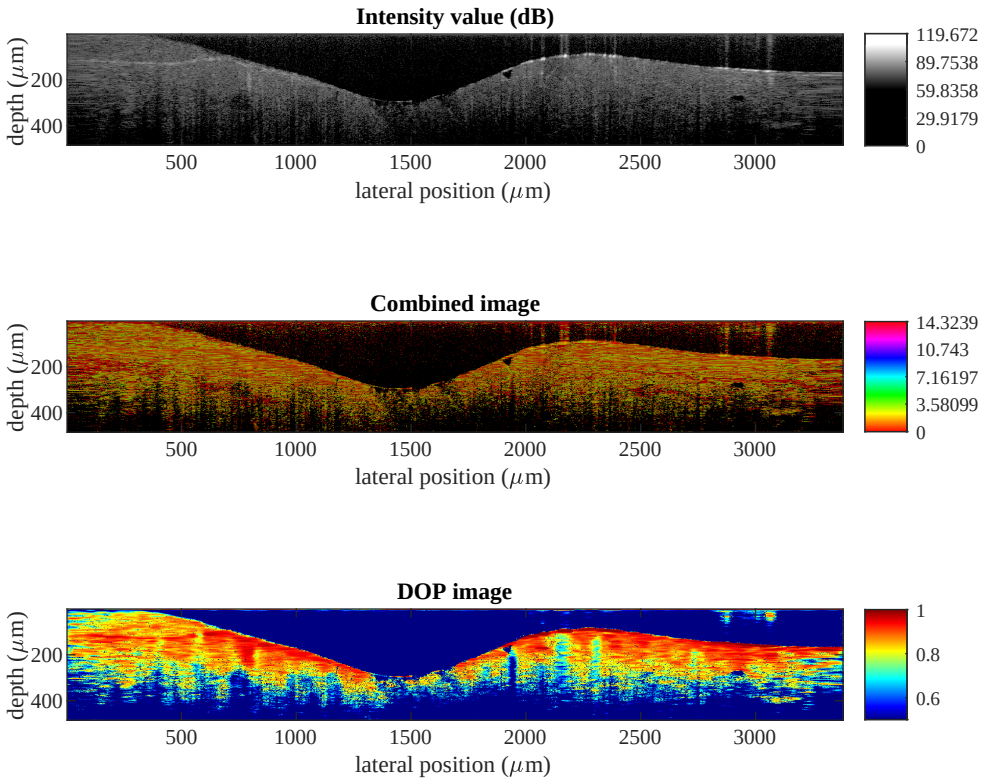

Figure 3.15: Top: OCT intensity image in decibels. Middle: OCT intensity image with the per pixel retardance as the color channel. Bottom: The degree of polarization (DOP) image which measures tissue uniformity.

4 Instrument Validation and Measurement of Scattering in Thermal Ablation

The work presented in this chapter is taken largely from a collaboration with Dr. Sevde Etöz from Prof. Chris Brace's lab and Daniel Gil from Prof. Melissa Skala's lab. The text and figures are adapted from the resulting publication [115].

4.1 VIS-OCT Scattering Quantification: Validation with Liquid Phantoms

Once the initial instrument construction was complete, the sensitivity of scattering measurements needed to be validated and assessed. Optical scattering phantoms are the subject of intense research

due to the utility of optical scattering quantification [73, 86]. The optical properties of phantoms can be predicted based on Mie scattering calculators developed by others which use the characteristics of the media and the scatterer —citematzler2002matlab. The media spectral refractive index and the scatterer size, concentration, and spectral refractive index will dictate the refractive index contrast and the scattering cross-section per unit volume as described in Section 2.2.1. The calculators will then determine the optical scattering as a function of wavelength for a given set of input parameters.

Several varieties of phantoms were investigated, including a solid, shelf-stable phantom composed of poly-dimethylsiloxane polymer (PDMS). While solid phantoms are an attractive choice, investigation of the spectral refractive index revealed several complications. A novel method of spectral refractive index measurement was published which was sensitive to the bulk refractive index of the test material [116]. The method demonstrated that the curing process of PDMS was not entirely consistent for the small scale fabrication desired for these phantoms. Furthermore, this study along with others demonstrated a boundary effect for PDMS refractive index where the index was a function of distance to a boundary with another surface and thus altered the predicted index contrast of the phantom. A final complication was the mixing of spheres with PDMS polymer. Typical microspheres of the size and composition needed to construct Mie scattering phantoms are produced in an aqueous media, which is not directly miscible with PDMS due to the hydrophobicity of PDMS. The result of mixing the spheres in water suspension with the PDMS was air pockets which themselves would form either large cavities or high scattering signal from the index contrast of air and water. Attempts to transfer the spheres from water to a more miscible solvent proved difficult due to sphere aggregation which could not be reversed. Ultimately, the most accurate phantom, while not suitable for long term use, consisted of polystyrene microspheres suspended in water.

An initial liquid phantom was prepared by careful dilution of a 0.40 μm microsphere stock solution (Bangs Labs, Fishers, IN). The Mie calculation for a scattering coefficient, μ_s, of approximately 460 cm^{-1} at 575 nm was used to create the initial phantom which was approximately 2.0% (wt/wt) of polystyrene in water. This initial phantom was then serially diluted by a factor of 2 to create several phantoms of lower concentration down to 28-29 cm^{-1}.

These phantoms were imaged both on the VIS-OCT system described in Section 3.1 and a commercial Telesto NIR-OCT imaging system (Thorlabs Inc., Newton, NJ). The Telesto system

consisted of the Telesto II base (TEL1300V2-BU, Thorlabs Inc., Newton, NJ) which was coupled to an adjustable scanner (OCTP-1300(/M, Thorlabs Inc., Newton, NJ) equipped with a laser scanning lens kit LSM03 (OCT-L3, Thorlabs Inc., Newton, NJ). The image acquisition with the Telesto system was powered by ThorImage (Thorlabs Inc., Newton, NJ) and analysis was performed in Matlab. Briefly, the NIR system was used as a commercial comparison to assess the performance of the custom system and to offer a complementary data set. The NIR system possessed lower resolution and scattering contrast, but possessed a greater axial field of view and higher SNR. Additionally, several NIR-based commercial instruments have clinical approval already, offering a comparison for a more clinic-ready instrument. The specifications of these instruments are compared in Table 4.1.

System Parameter	**VIS**	**NIR**
Source Central Wavelength (nm)	575	1300
Source Bandwidth (nm)	200	170
Axial Sampling (μm)	1.1	3.4
Axial resolution (coherence length) (μm)	0.9	3.7
FWHM Single Reflection in Air (μm)	3.4	5.5
A-line Length (pixels)	700	1024
Axial Range in Air (mm)	0.8	3.5
Sensitivity (dB)	65	111
Lateral Resolution (μm)	5.61	13.0
Lateral Pixel Size (μm)	5.3	5.0
Peak Power at λ_0 (mW)	0.18	2.09

Table 4.1: Comparison of the VIS and NIR OCT systems used in the ablation study. The NIR offered a greater lateral and axial field of view. The VIS offered superior resolution.

Fitting of the optical properties was performed as described in Sections 2.5.1 and 3.2.3. In addition to the previously described steps, a noise profile was fitted for each image to account for the so-called pink noise' or $1/f$ noise that is common in OCT systems which was mentioned in Section 2.4.2. This noise was mitigated by imaging a glass slide or single reflector, digitally removing the single interface, and then fitting a profile of the noise which was subtracted from data before compensating for the depth-dependent fall-off. This process published here [115] and reprinted below demonstrates this procedure graphically in Figure 4.1. For simplicity, the dispersion compensation steps are not shown. As described previously, the spectral shape is removed from the detected interferogram, I_{det}, which gives I_{ac}. After dispersion compensation, the interferogram is subjected to a fast Fourier transform (FFT) to get $I(z)$. The fitted noise from a single reflector

is subtracted before correcting for the depth-dependent fall-off. Figure 4.1 shows the mean A-line profile for a liquid scattering phantom on a log-scale of intensity. The highly linear region in the final panel is an excellent demonstration that a well-corrected signal has a straightforward fit to determine μ_s.

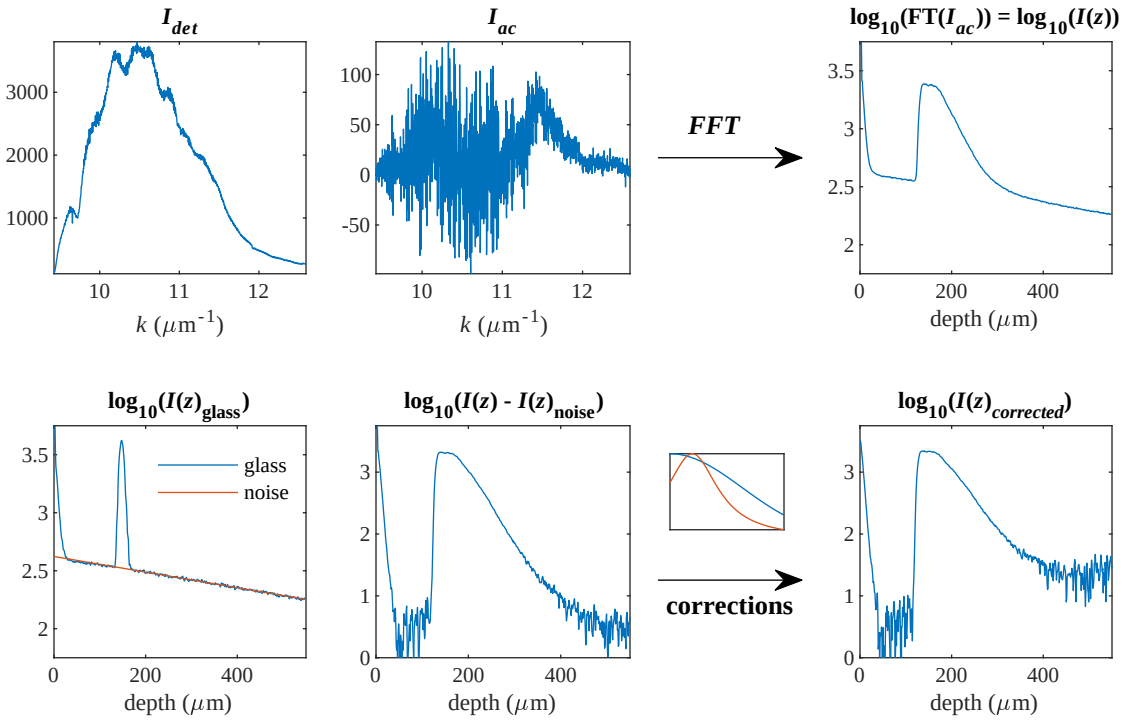

Figure 4.1: The image processing procedure begins by subtracting the mean B-scan interferogram from each A-line interferogram (I_{det}), isolating the desired signal, I_{ac}, from the source spectrum. This subtraction eliminates the DC term in the interference equation. The A-line image is then calculated by taking the Fourier Transform of I_{ac}. The system noise floor, $I(z)_{noise}$, is determined by fitting an image of glass, $I(z)_{glass}$. $I(z)_{noise}$ is subtracted from $I(z)$ before applying fall-off corrections to $I(z)$. The spectrometer fall-off correction (blue) is fixed while the confocal roll-off correction (red) is centered at the focal position, which must be known when imaging. The final image intensity is well-corrected until the noise floor of the image is encountered at the limit of imaging depth.

Using this workflow, images were acquired from all scattering phantoms on the custom VIS-OCT and commercial NIR-OCT instruments. Final images were fit to determine the bulk μ_s and compared to the theoretical values. Fitting for bulk values of μ_s was performed as many pixels as possible in the axial dimension to provide the fitting algorithms with a long range to minimize the impact of noise. The end point of the fits could be set manually, typically 50-100 μm in the

VIS-OCT system or 150-300 μm in the NIR-OCT system. Alternatively, the point at which the signal decays to $I_0/exp(2)$ is a convenient length to fit as it corresponds to $nz = l_s$ or the mean free path which is another measure of optical scattering properties. Furthermore, l_s is typically within the depth of imaging of the system and typically well above the noise floor. The data of these fits published in [115] shows high agreement in using the VIS-OCT system until the highest amount of scattering (μ_s = 400 cm^{-1}), which was estimated to be the maximum amount of scattering which could be detected. This was acceptable since scattering in tissue rarely exceeds 200 cm^{-1}.

An example image of a phantom from the NIR-OCT system in Figure 4.2 is accompanied by the plot of μ_s across the scan and demonstrates that variations in μ_s were not due to the sample position in the axial field of view. This provides some evidence that the depth-dependent fall-off has been correctly mitigated and the consistency of the fit value is evidence that the fitting procedure is working correctly. Bulk values of μ_s taken as an average of all lateral positions in the image show good agreement between predicted and measured values of μ_s. Both the custom VIS-OCT instrument and the Telesto NIR-OCT system had a low value for the maximum values of μ_s which suggest that this is a limitation of the fitting procedure rather than a limitation of either instrument. A review of the data showed that the total length of the image was much shorter than typically used for fitting, which may have contributed to poor fitting results as the smooth noise floor would have appeared as a decreased rate of attenuation. Additionally, there was a constant offset in the NIR-OCT data where the measured value of μ_s was higher than predicted. This was attributed to the absorption spectra of water beginning to contribute to the attenuation of the OCT signal.

Additionally, as shown in Eqs. 26 and 36, the scattering coefficient is a function of depth, $\mu_s(z)$. The local value of $\mu_s(z)$ can therefore be determined by the pixel-to-pixel attenuation in depth, or as the derivative of the linear image by taking the natural log of $I(z)^2_{OCT}$. This measurement will be more susceptible to image noise since it does not have the benefit of being fit over several pixels. Lateral and axial averaging of the image can reduce this noise, particularly in a shot-noise limited system, however the effective resolution of the optical scattering properties will be diminished. With these conditions in mind, a radial blur of 2-4 pixels was used in the VIS-OCT imaging to keep the resolution equal to the NIR-OCT system and reduce the contributions of noise to the signal. Depth-resolved optical scattering was computed from the phantoms and is shown in Figure 4.3. It should

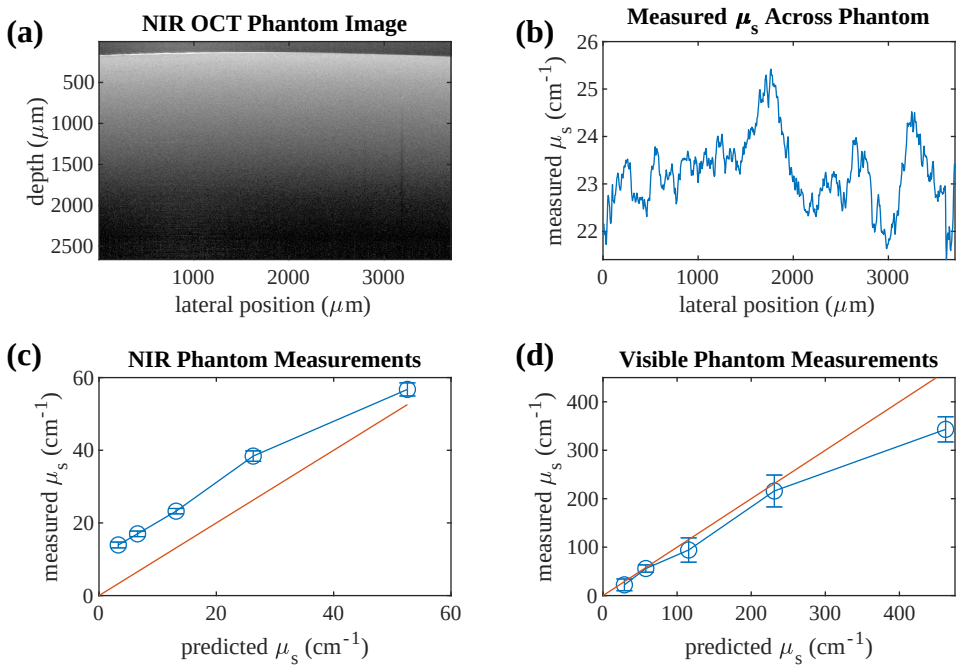

Figure 4.2: OCT image of polystyrene/water phantoms (a) with good uniformity across the sample (b). Measured vs. predicted scattering values for NIR (c) and visible (d) OCT systems showed good agreement and linear trends. Predicted scattering values were computed from Mie theory using polystyrene sphere size and concentration in water.

be noted that $I(z)$ in the top row of the figure is analogous to the backscattering coefficient, $\mu_b(z)$, and changes consistently between dilutions. The depth-resolved scattering map in the bottom row of Figure 4.3 also changes consistently with dilution. The bulk of the $\mu_s(z)$ image is also consistent throughout the field of view until the noise floor begins to be included in the small window for fitting.

4.2 Assessing Esophogeal Ablation Boundaries

Thermal ablation is a tumor treatment strategy that is common in the liver and kidney with growing applications in esophagus, lung, heart, and brain [117]. Microwave and radiofrequency ablations involve delivering thermal radiation from a probe radially to heat the tumor sufficiently to eradicate the malignant tissue. In tissues with finer structure and where thermal dose must be precisely controlled, high-resolution and high-speed imaging technologies with intrinsic contrast are of vital

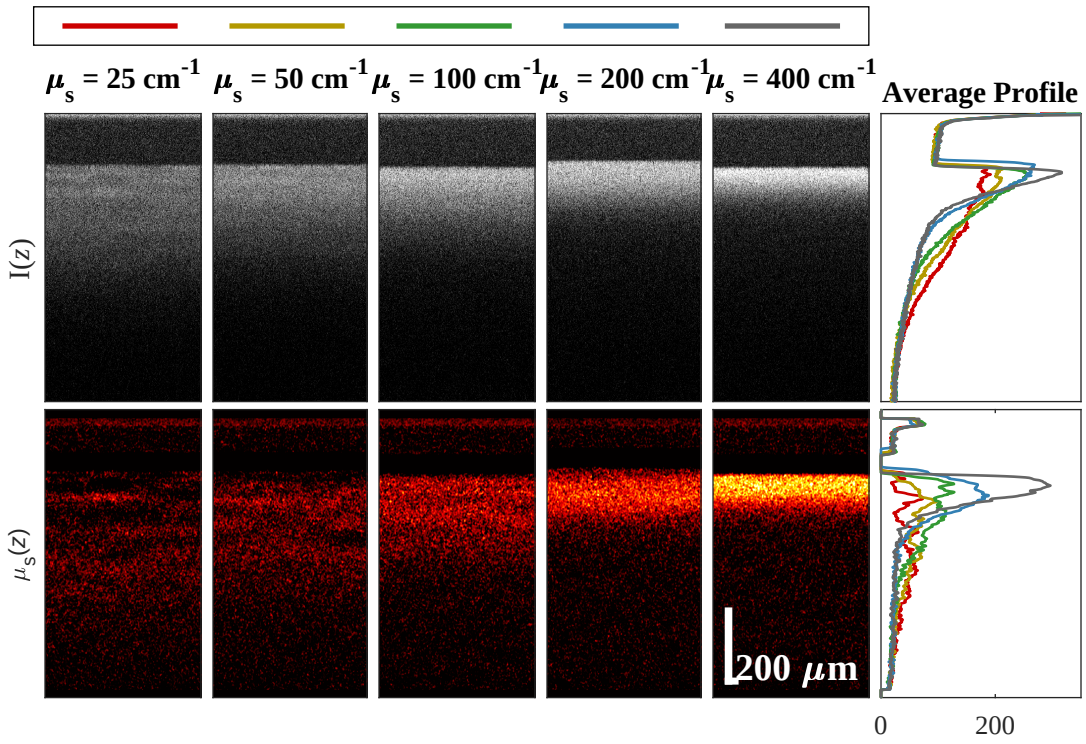

Figure 4.3: Intensity OCT images of the different scattering phantoms (top). Depth-resolved determination of scattering demonstrates uniform scattering within phantoms throughout the available depth (bottom). Axis of scattering graph in cm^{-1} and shows good agreement between predicted and measured μ_s when averaged and adjusted for smoothing.

importance. Thermal ablation leads to denaturation of proteins, tissue dehydration, and membrane degradation, all of which will impact optical scattering. Thus, OCT has the potential for high impact in this area for both tumor boundary estimation and image-guided therapy [118, 119, 120].

Barrett's esophagus (BE) is a premalignant lesion strongly associated with the development of esophogial adenocarcinoma, a cancer with a 5-year survival rate of less than 15% [121]. Standard practice is to evaluate suspected lesions with white light endoscopy and endoscopic biopsy in order to diagnose the abnormal region as no dysplasia, low-grade dysplasia, high-grade dysplasia, or intramucosal carcinoma. In both high-grade dysplasia and intramucosal carcinoma, endoscopic resection is used to remove lesions followed by thermal ablation to ensure total destruction of malignant tissue [122]. While radiofrequency ablation (RFA) is an established technique for delivering the thermal dose, there is high variability in RFA success rates for treatment of BE and the eradication rates of high-grade dysplasia are lower than that of low-grade dysplasia [123, 124, 119].

Additionally, the presence of buried glands not visible in white light endoscopy may result in recurrence and have been observed post-RFA treatment in patients. To improve treatment outcomes, both improved ablation methods and depth-resolved quantitative imaging methods are required.

To treat BE successfully, the Barrett's epithelium must be completely eradicated with minimal damage to the submucosa and the surrounding healthy tissue [125, 126]. While endoscopic microwave system are currently not in clinical use in the GI tract, they have recently emerged as a powerful tool in thermal ablation therapy [127]. Microwave heating induces agitation of polar molecules in the tissue and is not limited by media with low electrical conductivity, unlike RFA [117]. As a result, microwaves can penetrate electrically inhomogeneous tissues more uniformly than RFA and may have improved performance in treating more advanced stages of BE. To monitor the depth of ablation, several clinical imaging modalities have been used in both liver and kidney including magnetic resonance imaging, computed tomography, and ultrasound [128]. These imaging methods, however, lack the resolution sufficient to visualize the microstructures of the esophageal tissue layers [129, 130]. Recently, NIR-OCT has been proposed as a new tool in monitoring ablation therapies. Work from the Hendon group in particular has recognized that OCT possesses the resolution, field of view, speed, and intrinsic contrast to monitor the volumetric extent of the ablation zone [131, 132].

To further this work, a collaborative study was proposed using the above-described VIS-OCT and Telesto NIR-OCT systems to assess microwave ablation in porcine esophagus. As described in Section 4.1, both systems were capable of optical scattering quantification and possessed imaging resolution on the order of 5 μm. Previous work in the ablation field has also noted changes in optical scattering and scattering anisotropy during ablation, which agrees roughly with the effects of dehydration in tissue [118, 133, 134, 135]. It has also been shown that temperatures above 60°C induce protein aggregation from denaturation, which is also a source of increased optical scattering [136, 137]. It was hypothesized that both the VIS-OCT and NIR-OCT instruments would be sensitive to these changes in scattering which would be sufficient for identifying the ablation zone boundaries. The transition zone is particularly difficult to characterize, not just by OCT, but also other methods of optical property determination. Developing an optical scattering-based metric for identification of the ablation zone boundary would provide valuable information for high-resolution image guidance which may, in the future, lead to real-time guidance during

ablation therapy.

Porcine esophagus tissue was harvested within one hour of sacrifice of three swine. Microwave ablation was performed using a 2.45 GHz generator through a coaxial antenna placed against the luminal surface of the esophagus (Certus 140; NeuWave Medical Inc, Madison, WI). Generator power was set to 20 W and applied for either 40 seconds or 20 seconds. Different application times were used to show the sensitivity of the proposed technique to tissues with different amounts of thermal injury. Ablations using the 40 second application time were replicated in three locations on each of the three esophagus samples. Tissue was then imaged with both VIS-OCT and NIR-OCT. After imaging, several samples were stained with triphenyltetrazolium chloride (TTC) to demarcate zones of necrosis from viable tissues. Esophageal tissues were then imaged with OCT within five hours of ablation. Imaging of normal and healthy regions of tissue samples was performed in the same imaging session. During this time, tissues were kept hydrated in normal phosphate buffered saline. After imaging, ablated and normal tissues were prepared for histologic analysis. Samples were embedded in cryosectioning gel before being frozen on a metal block with dry ice, then placed on a cryostat and sectioned into 4 μm slices. Slices were stained with hematoxylin and eosin and imaged for a gross estimation of morphology of normal and ablated tissue. This workflow is summarized graphically in Figure 4.4

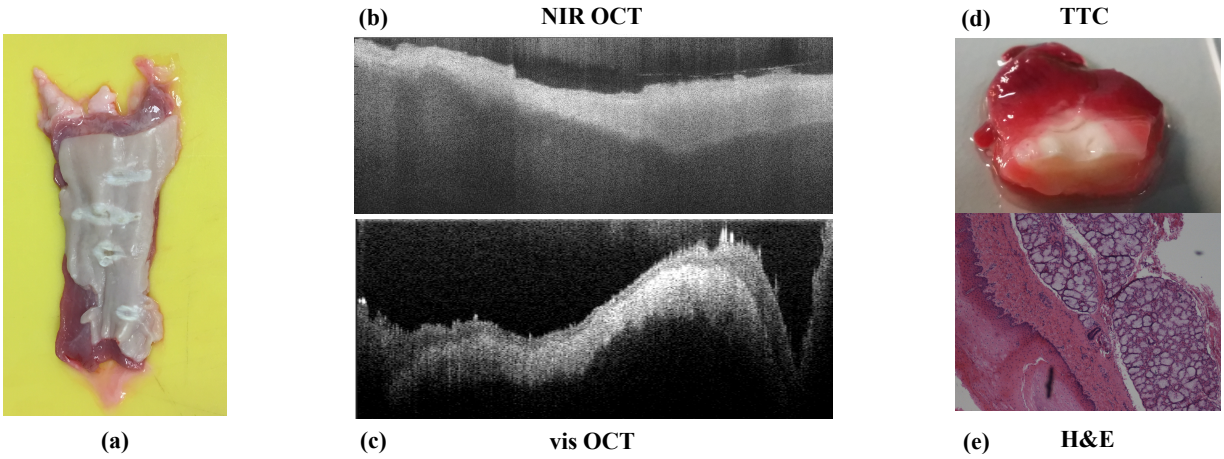

Figure 4.4: The schematic illustration of methods: (a): ex-vivo ablation of swine esophagus, OCT B-scans that are acquired with the NIR (b) and visible light OCT systems(c), TTC staining (d) of the sample and the H&E staining of normal and ablated tissues (e).

OCT imaging was able to provide high resolution images of both normal and ablated tissues.

Tissue type	NIR μ_s (cm^{-1})	NIR % change in μ_s	VIS μ_s (cm^{-1})	VIS % change in μ_s
Normal	25.4 ± 7.0	n/a	100.6 ± 18.9	n/a
Transition zone	57.4 ± 19.3	226.4%	231.6 ± 96.9	230.2%
Ablated	105.2 ± 36.7	415.0%	349.9 ± 178.7	347.8%

Table 4.2: Optical properties relative to non-ablated tissue (normal) samples. Data provided as sum of means from 9 total ablation sites. N = 3 swine were used with each tissue sample receiving 3 ablations that were imaged under both systems.

The depth limit of OCT imaging is governed by light scattering within the tissues and by Fourier domain sampling rates. NIR OCT was subject to less scattering and was capable of imaging 1.5-2.0 mm into tissue, which was sufficient to reach the submucosa. In contrast, the visible light OCT signal was completely attenuated by 300 μm into tissue, restricting images to the epithelial layer due to the increase in scattering at shorter wavelengths. While the imaging depth is reduced in the visible system, there appears to be more contrast, suggesting a greater sensitivity to scattering. Comparison with histology confirmed the structures visualized in OCT (Figure 4.5). Of particular note, regions in histology that appear as cavitation correspond to regions of hyperscattering in the OCT B-scan, which is consistent with previous findings. Hematoxylin and eosin staining were unable to directly visualize the ablation region due to microwave fixation preserving the cell membrane structure. Images of stained tissues showed degradation of tissue which were not observed as often in OCT, a common problem with histology of ablated tissue. TTC staining provided visual confirmation of a region of completely necrotic tissue at the ablation core while tissue outside of the ablation zone remained viable. TTC staining was not used for quantification due to the need for sectioning to analyze the depth of the ablation.

Using both visible and NIR OCT, fitting over regions of interest for μ_s demonstrated significant differences between normal and ablated tissues. Furthermore, there were variations in μ_s within the ablated zone owing to the inhomogeneous heating pattern of the antenna. Patterns in the scattering can be observed in Figure 4.6 which provides a map of maximum intensity or backscattering (Figure 4.6, left) and a map of the scattering coefficient (Figure 4.6, right) fit over a small tissue volume. The major axis of the antenna was found to have the greatest increase in scattering. The scattering coefficients presented in Table 4.2 demonstrate the substantial increase in μ_s as the core of the ablation zone was reached.

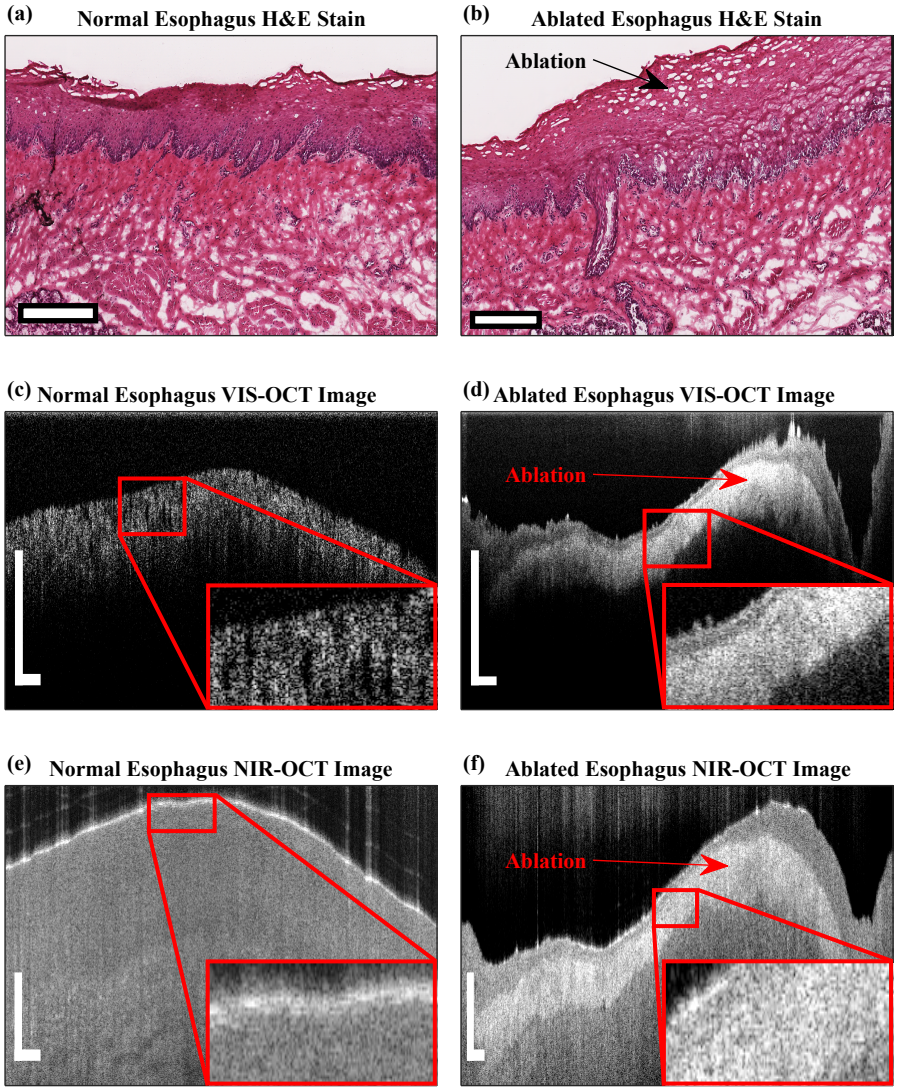

Figure 4.5: (a) Normal esophagus H&E staining, (c) VIS-OCT and (e) NIR-OCT images from different tissue sites. Ablated tissue imaged by (b) H&E staining, (d) VIS-OCT and (f) NIR-OCT. The ablation zone becomes apparent in OCT due to increased backscattering which displays as higher intensity in the image. All scale bars represent 300 μm in each direction. All zoomed insets are approximately 125 μm axially and 800 μm laterally.

To compare scattering coefficient values from regions of normal, ablated, and transition zones, regions of interest were determined by finding the surface of tissue or the ablation zone and extended to between 50 and 100 μm in depth, corresponding to approximately ls in tissue. These restrictions also ensured only the uppermost layer (epithelium) of normal tissue was compared with corresponding layer of ablated tissue. The tissue surface was consistently used for the start of fitting

in the normal tissue, however the surface location algorithm was adjusted to detect the surface of the ablation zone for proper segmentation of transition and ablation zones before fitting. Applying these restrictions to fitting a volume of tissue allows visualization of the decrease in backscattering and μ_s as distance from the antenna placement increases (Figure 4.6). The results of Table 4.2 also demonstrate that both systems were sensitive to changes in μ_s, the magnitudes of which were well within the range of the phantom calibrations. Mapping these changes in μ_s in an *en face* view (Figure 4.6, right) allows for both qualitative and quantitative characterization of normal, transition, and ablated tissue.

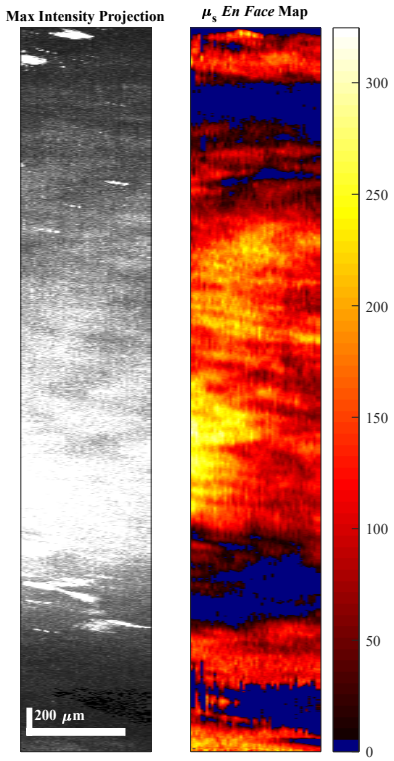

Figure 4.6: A maximum intensity plot (left) demonstrates the increase in backscattering while a scattering map (right) shows increased attenuation in the leasion which was not found to correlate to surface location. Blue pixels indicate locations where either surface location or fitting failed.

Intensity of the OCT signal is proportional to $\mu_b(z)$, meaning that an intensity image serves as a map of $\mu_b(z)$ after correcting for depth-attenuation of the OCT signal due to the system. Changes in the backscattering were observed in intensity images for tissues ablated for both a short time of 20 seconds (Figure 4.7(a),(e)) and for longer times of 40 seconds (Figure 4.7(c),(g)).

To complement these observed changes in backscattering, depth-resolved measurements of attenuation were converted to $\mu_s(z)$. Analogous to the phantom images in Figure 4.3, an image of the local scattering coefficient was created by mapping $\mu_s(z)$ as intensity on a single color axis (Figure 4.7(b),(d),(f),(h)). In 20 second ablations (Figure 4.7(b),(f)) there is a minor increase in scattering that is more noticeable in the visible image (Figure 4.7(b)). The increase in scattering is more apparent in the 40 second ablation images (Figure 4.7(d),(h)). The increased visibility of the scattering in the visible images is attributed to the absolute increase in scattering values at visible wavelengths.

Bands along the surface of the tissue or surface of the lesion present themselves as negative scattering due to the transition from a low-backscattering region to a high backscattering region (i.e. intensity increases between pixels). The bands visualize the method by which surface detection was performed. A lower boundary of the ablation zone can be seen in another artifact that appears as high scattering values outside physiological ranges where the tissue transitions from highly backscattering ablation zone to less backscattering normal tissue or noise floor. While useful for qualitative assessment of the size of the ablation zone, these artifacts should be removed from any quantitative assessment of scattering.

The distinct change in μ_b but small change in μ_s suggest that at low ablation temperatures, the scattering anisotropy (g) decreases. At longer ablation times, a greater change in μ_s was observed, indicating higher scattering once higher temperatures are reached. As expected, these measurements of $\mu_s(z)$ suffered from image noise which can be reduced by smoothing or blurring the image, but at the cost of spatial resolution.

Microwave ablation therapy benefits substantially from image guidance to monitor ablation size and would be improved with additional quantitative metrics at imaging. Here we have determined a significant increase in the scattering coefficient, μ_s, in tissue that was subjected to microwave ablation using both VIS-OCT and NIR-OCT. Linear fitting of log-scale data produced maps of optical properties across volumetric scans 5000x300x100 μm (Figure 4.6). Interestingly, OCT imaging of the ablated region reveals a thin layer ($\approx$ 25 μm) that has lower backscattering intensity and lower apparent scattering coefficient. This layer is not obvious in histology and suggests lower temperatures than the ablation threshold due to the cooling mechanism of the antenna or from fluid retention. Depth-resolved fitting allowed generation of attenuation images that showed

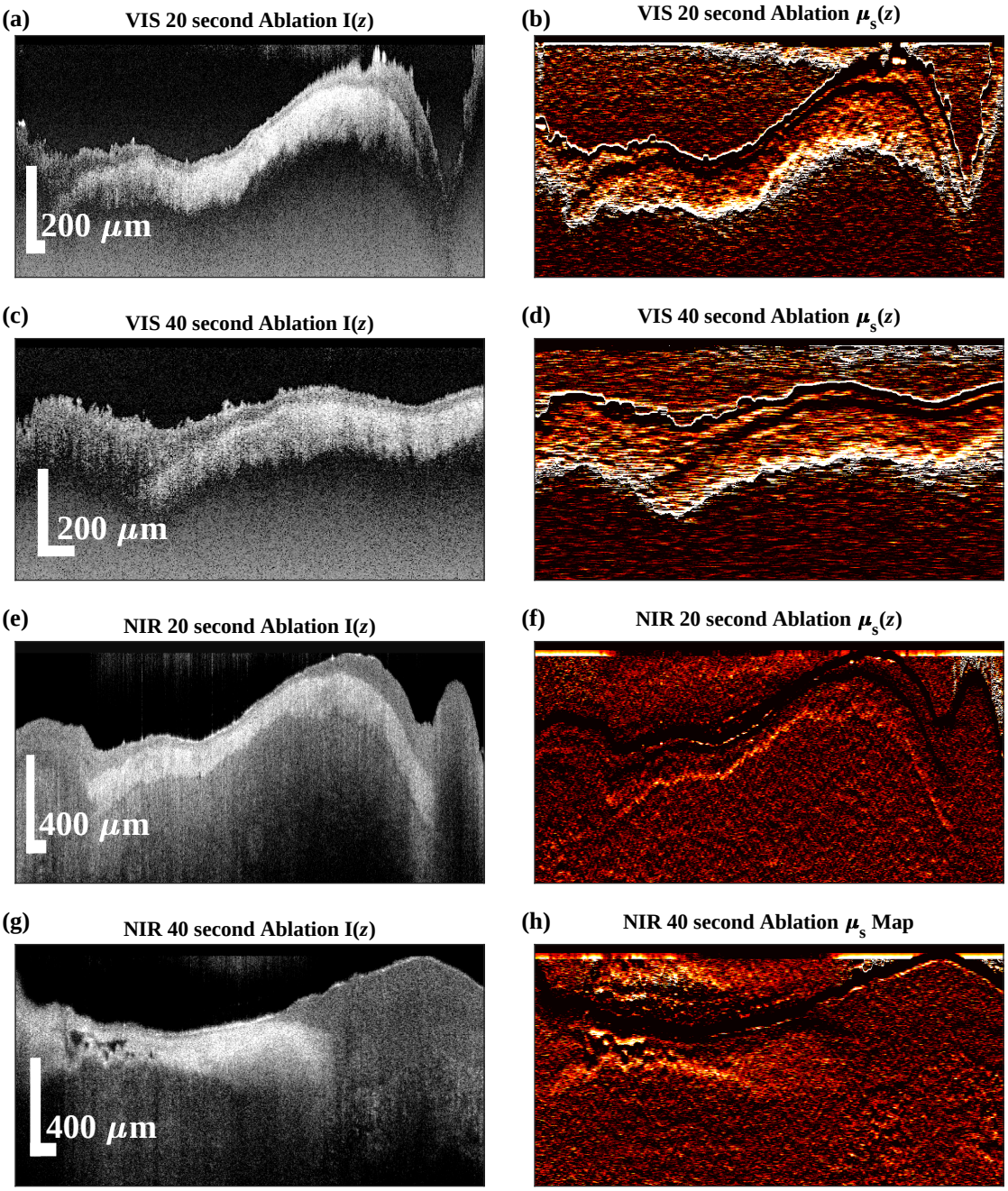

Figure 4.7: OCT intensity images (left) and $\mu_s(z)$ images (right) demonstrates changes in tissue scattering after ablation. In normal OCT B-scan images, pixel intensity is proportional to the backscattering,$\mu_b(z)$, which demonstrates increased backscattering in ablation. Scattering maps of 20 second ablations (b,f) show less contrast between normal and ablated tissue as compared to 40 second ablations (d,h). VIS-OCT images (a-d) show greater detail due to increased $\mu_s(z)$ in both normal and ablated tissue, however NIR images had a larger FOV (e-h). Heatmap colorbar scaled between 0 and 800 cm^{-1}.

changes in optical properties throughout the ablation zone and between tissue layers. Several potential factors exist that may contribute to the observed changes in optical properties, which have been characterized previously citeyi2013can, samatham2008optical, backman2013advances. The explanation is likely three-fold: contraction of the tissue, disruption of the extracellular matrix, and cell morphology changes.

Tissue contraction in ablation has been well documented and would easily contribute to the increase in scattering by simply changing the concentration of scatterers per unit volume or the differential scattering cross section per unit volume[63, 135, 55]. Dehydration of the tissue would also contribute to both effects and should be carefully considered in any *in vivo* or *ex vivo* experiments.

The extracellular matrix is also vulnerable to changing as a result of thermal ablation. In particular, collagen shrinkage was characterized at temperatures around 60°C and observed to change from organized fibers to an amorphous structure as a function of temperature [138]. Changes in the ECM composition are known to affect the scattering phase function, which describes the magnitude of scattering as a function of angle relative to the incidence [63]. This would imply that the fraction of scattered light that backscatters would be higher in ablated tissues where the tissue has become less forward-scattering or more isotropic. This could explain the increase in the apparent backscattering seen in the low power ablation images (Figure 4.7) without a dramatic increase in μ_s.

There have been many attempts to characterize thermal damage during ablation on a cellular level. Between 60°C and 140°C, protein denaturation, cell shrinkage and hyperchromaticity occur in ablated liver tissue [28]. The most significant ultrastructural change after heat injury was found in mitochondria with intramithocondrial dense granules, vesicularization of cristae, myelin damage, and swelling of intracristal areas [136]. Each of these effects can alter light scattering and OCT signal.

VIS-OCT and NIR-OCT provide different resolution and imaging depth, and scattering at these wavelengths are also sensitive to different structures, potentially to providing complementary information. This study demonstrates that both modalities can quantify differences between the optical properties of ablated and normal tissues. These differences can be seen with a resolution that has not yet been attained by conventional image-guidance methods. This information could provide axial and lateral information on the shape of the ablation core and transition zone, especially as

processing methods and visible OCT system capabilities are improved. OCT imaging revealed a fine layer of lower scattering that is not evident in histology which may not have been completely ablated. The use of optical properties derived via OCT to diagnose and visualize cancerous lesions is also of clinical importance [139, 140]. These data are particularly useful when assessing antenna performance and offer advantages over histology methods. Viability staining was the only histological tool able to confirm cell areas of necrosis from microwave ablation due the microwave fixation effect. Agreement between TTC stained tissue cross-sections and OCT images imply that increase in μ_b before a change in μ_s is observed could be a sign of non-viable cells after ablation.

Quantitative analysis of OCT signals may provide a new metric for studying, monitoring, and guiding ablation therapies. Ablation therapies utilize image guidance to minimize damage to healthy tissue. Previous work has observed hyper-scattering present in ablated tissue [141]. Rigorous determination of scattering in the ablation zone provides a useful criterion for determining the boundaries of the ablated zone. OCT endoscopes can be used to acquire scattering data for real time identification of ablation boundaries.

5 Polarization-Sensitive OCT as a Tool to Monitor Lung Fibrosis

The work presented in this chapter is based of a large collaborative study primarily with Dr. Ksenija Bernau, Dr. Nathan Sandbo, Dr. Allan Brasier, and Prof. Paul Campagnola.

5.1 Idiopathic Pulmonary Fibrosis of the Lung

Idiopathic pulmonary fibrosis (IPF) is a disorder of the lung which causes fibrosis due to unknown origins and has a lower 5-year survival rate than many cancers [41, 27]. IPF remains challenging in both diagnosis and treatment since the exact mechanisms remain unknown [41, 27]. A large body of work has been developed aimed at examining the causes of lung fibrosis and potential drugs to mediate or reverse the fibrotic response [40]. In a collaboration with groups at University of Wisconsin-Madison, an animal model of IPF was assessed using polarization-sensitive VIS-OCT (PS-VIS-OCT), commercial NIR-OCT, and enhanced backscattering spectroscopy (EBS) to evaluate both the progression of fibrosis and the efficacy of a novel therapeutic.

A mouse model treated with bleomycin, a chemotherapy agent, has been shown to develop a fibrotic response within the lungs similar to IPF. It has been observed that IPF manifests with drastic changes to the ECM and its cellular constituents which may govern disease progression [26, 41]. Increases in fibrillar collagen deposition are hypothesized to drive the ECM stiffening which in turn influences cell fate [41]. The precise organization and accumulation of fibrillar collagen is not known precisely and has recently been studied by SHG microscopy [142, 143]. The sensitivity of SHG to collagen fibers has made it a powerful tool to study *ex vivo* tissue to understand micro-scale schanges to the collagen architecture. Studies have shown increased deposition and alignment of collagen fibers, which should impact both the optical scattering and the polarization properties of the tissue [143]. Measurements of the reduced scattering coefficient (equal to $\mu_s(1-g)$) using SHG microscopy demonstrated increased optical scattering of IPF lung versus control tissue [142]. Changes in the scattering anisotropy, g, were also observed [142]. Using these data to inform OCT system designs, this project aimed to establish OCT-based optical scattering measurements which could be utilized in an *in vivo* catheter-based OCT system for patient diagnosis and treatment monitoring.

These changes in tissue properties make PS-OCT an ideal choice to investigate tissue remod-

eling. The adaptability of OCT to an endoscope makes it an attractive choice for clinical use and current work has shown the ability of catheter-based PS-OCT systems to detect birefringence in airway smooth muscle [89]. A PS-VIS-OCT system was used alongside a commercial NIR-OCT system to assess airway and parenchyma remodeling to establish the criteria for a clinical prototype. The superior resolution of the VIS-OCT system comes at the cost of decreased depth of imaging. However, when the epithelium is a main region of interest, the trade-off is beneficial due since the epithelium is thin and high resolution is paramount. The NIR-OCT system was chosen for the best resolution performance possible and was identified as a strong candidate for clinical translation given the ease of adaptation to a catheter or endoscope for imaging. Additionally, the depth of imaging achievable in the NIR may be sufficient to image both the airway epithelium and the parenchyma. The polarization-sensitivity employed in the VIS-OCT system was engineered to exploit the increase in tissue birefringence that could arise from increased collagen deposition. Finally, EBS was used to discern scattering from nanostructure beyond the resolution of either OCT instrument.

The optical modalities to measure scattering were used to evaluate the bleomycin animal model and the efficacy of a novel therapeutic aimed at reducing the fibrotic response. Control animals were dosed with vehicle while bleomycin-treated animals were dosed with either a vehicle (negative control) or a novel small molecule inhibitor of bromodomain-containing protein 4 (BRD4) [40]. This inhibitor, ZL0591, is hypothesized to inhibit the remodelling response elicited by the activation of toll-like receptor TLR3-NF-KB/RelA pathway [40]. Inhibition of this pathway should decrease the fibrotic response while vehicle treated animals continue to develop fibrosis [40].

A primary goal of this study was to establish the minimum necessary criteria to screen for lung fibrosis. IPF is known to have greater scarring in the parenchyma of the lungs compared to the central airway [41]. However, access to the parenchmya is limited without biopsy. While SHG microscopy has been a powerful *ex vivo* method for scattering quantification, its lacks the clinical translation of OCT due to the higher source cost and the need to scan in depth [46, 34]. Additionally, OCT methods were compared to determine which would be more suitable. While the VIS-OCT allows for polarization sensitivity, it may be not be necessary and a simple quantification of optical scattering may be more relevant, which could be achieved with the NIR-OCT system with its greater field of view. Furthermore, the NIR-OCT may be capable of imaging into the parenchmya,

which may yield more relevant diagnostic information. In either case, the development of an *in vivo* diagnostic tool with sensitivity to collagen is desired since it could replace the need for invasive biopsy and histology staining. In addition to the invasiveness into tissue with already decreased function, histology may be time-consuming and may contain user bias that OCT-based scattering quantification may avoid.

5.2 Imaging and Optical Scattering Quantification in the Lung

A Ganymede NIR-OCT system (GAN620C1, Thorlabs) was used to study the lung microstructure due to its relatively high resolution and generous field of view. While depth of imaging was limited to approximately 500 μm, large axial range of imaging allowed the heterogeneous topography of the central airway and parenchyma to be imaged in a single volumetric acquisition. The Ganymede system was equipped with a scan lens kit (OCT-LK2-BB, Thorlabs) which was capable of 4 μm lateral resolution. The axial resolution of the base unit (GAN620, Thorlabs) was 3 μm in air (2.2 μm in water), a maximum axial range of imaging of 1.9 mm in air (1.5 mm in water), and had a max scan rate of 248 kHz. The high scan rate of the system allowed for several acquisitions to be taken in order to reduce the image noise by averaging, allowed for high-sensitivity imaging. Large volumes were also acquired using a small amount of A-line averaging.

Dual-input PS-VIS-OCT was used to maximize the amount of data collected from single samples. This also had the benefit of allowing for conventional PS-OCT processing along with the orthogonal Stokes vector based method. Due to the high axial resolution and reduced axial range of imaging for the PS-VIS-OCT, separate acquisitions were taken of the target sites in the tissue. Additionally, due to the increased acquisition time, smaller volumes were acquired with the PS-VIS-OCT system, however, this reduced lateral field of view was acceptable due to the surface height heterogeneity of the lung.

Tissue was subject to gross dissection along the sagital axis to expose the airway and parenchyma. Imaging was performed by scanning laterally along the airway and the ventral portion of the parenchyma in order to best discern where fibrosis was occurring and to evaluate the potential for airway to be used as a surrogate site for less-invasive imaging procedures. Lung samples were perfused and fixed in 4% formalin before being transferred to normal phosphate buffered saline for short-term storage. As a secondary method to measure optical scattering properties, EBS was

used to probe each sample after gross dissection. The sample was mounted such that the beam was able to probe multiple spots on each lung. After initial imaging with the PS-VIS-OCT and EBS systems, samples were stored in cryo-preservation using optimal cutting temperature compound.

Initial PS-VIS-OCT data did not yield a sufficient quality of imaging and cryopreservation was performed just before a temporary suspension due to COVID-19. During the suspension, the polarization analysis was refined, data processing was improved to implement the dual-input method, and the Ganymede system was purchased and initialized. Once the project was able to resume, the lungs were thawed and rinsed in phosphate buffered saline before being imaged on both the PS-VIS-OCT and Ganymede NIR-OCT systems.

5.2.1 NIR-OCT Imaging of the Lung

While results are still in the preliminary stages, initial data shows promising results. The NIR-OCT imaging (Figure 5.1) demonstrates several interesting pathological features such as the increased signal from the airway and the porous structure of the parenchyma. Broad structure can also be measured and quantified using the volumetric renderings of the NIR-OCT data. Furthermore, the high image quality suggests that interrogation of optical scattering properties given the proper image corrections.

The image system resolution was sufficient to determine much of the fine structure such as the cavitation in the parenchyma. Furthermore, the axial range of imaging was sufficient to capture the full depth of imaging in the central airway and the surrounding parenchyma, providing an excellent comprehensive view of the tissue. The maximum depth of imaging was lower than initially expected given the shift to NIR wavelengths, however, this is likely due to the fixation process and *in vivo* imaging may present a greater depth of imaging.

Substantial backscattering is observed in the airway images (which manifests as high image intensity) and presence of a low-scattering superficial layer is suggested by a rudimentary measurement of $\mu_s(z)$, see Figure 5.2. However, these measurements have neither been compensated for depth-dependent fall-off nor validated with a known scattering phantom, so precise quantification cannot be performed.

Initial depth-resolved scattering measurements place the value of μ_s on the order of hundreds cm^{-1}. These values are likely not realistic for the lung, as it would suggest that the signal would

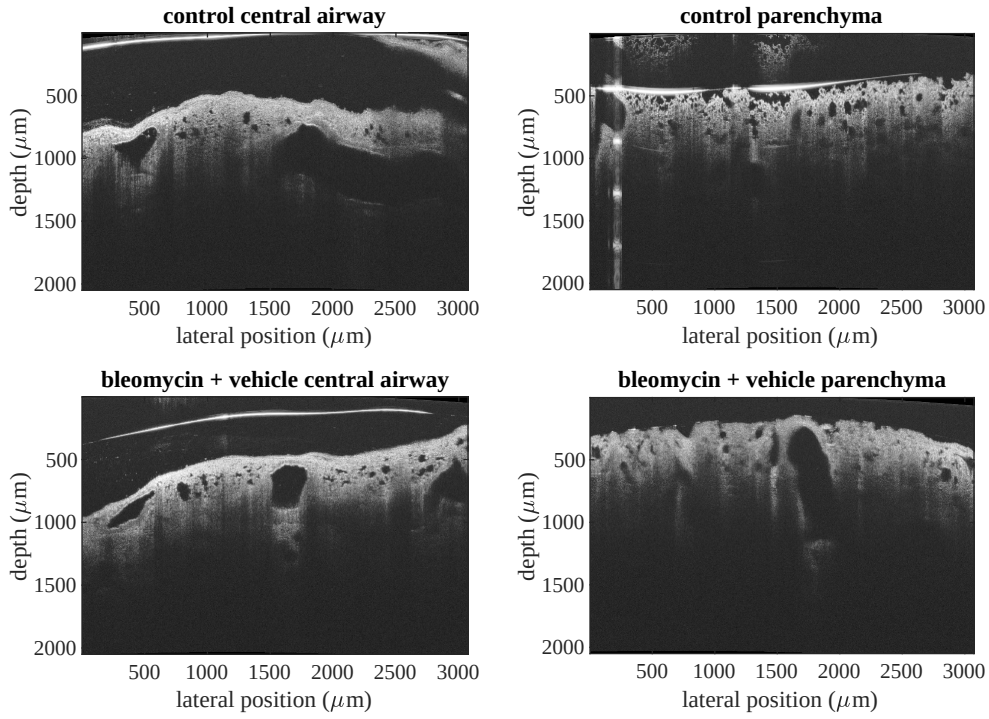

Figure 5.1: Images of the central airway and parenchyma using the Ganymede NIR-OCT system. Large fields of view were acquired in order to assess the anatomical structure as well as to quantify optical scattering.

fall to the noise floor within 100 μm rather than the nearly 0.5 mm of imaging depth observed in Figure 5.1. This additional decay is likely due to the signal fall-off and can be corrected. The Ganymede system itself was not available until after COVID-19 restrictions were lessened and is still undergoing fine calibrations. Furthermore, the parnechyma will be difficult to quantify due to the substantial amount of voids int he image which may be misinterpreted by the scattering quantification algorithm. The lack of signal in the void is mislabeled as high scattering which the transition from void back into tissue is mislabeled as negative scattering. This can be solved by blurring the image to essentially eliminate these structures, but the sacrifice in resolution would drastically reduce the ability to measure local increases in optical scattering.

A volumetric rendering (see Figure 5.3) of the central airway reveals several striking features that are not apparent in the B-scan. Folding of the airway, branch angle and diameter, and the size of the canal structure visible in Figure 5.1 (top left) may all be useful pathological dimensions to quantify. Furthermore, the fine structure of the parnechyma is also easily visualized and can the

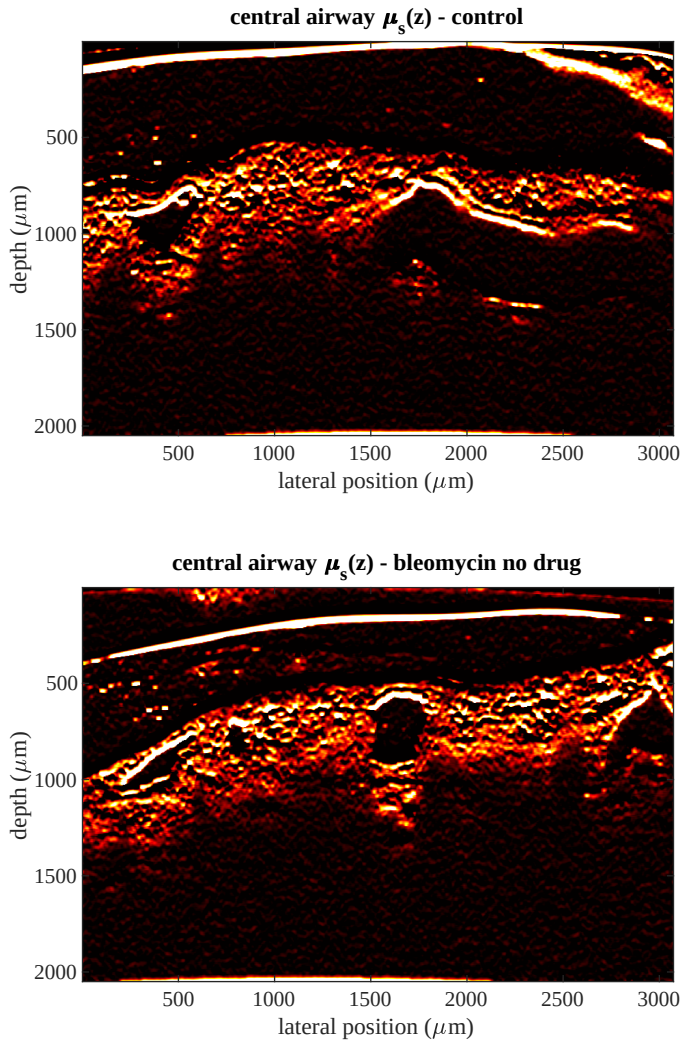

Figure 5.2: $\mu_s(z)$ image of the central airway in a control mouse (top) and a mouse treated with bleomycin and no drug for 21 days (bottom) using the Ganymede NIR-OCT system. A clear artifact can be seen at the surface of the liquid-air interface and can be easily segmented and removed from further analysis.

size of the alveoli may be assessed.

In addition to providing structural information, the volumetric data of the full lung can be rapidly acquired from preserved samples. Reconstructions can be performed to render the full volume of the lung and optical scattering could be measured from the full volume. Comparing this data to micro-CT, which measures tissue density, may yield insight into tissue architecture.

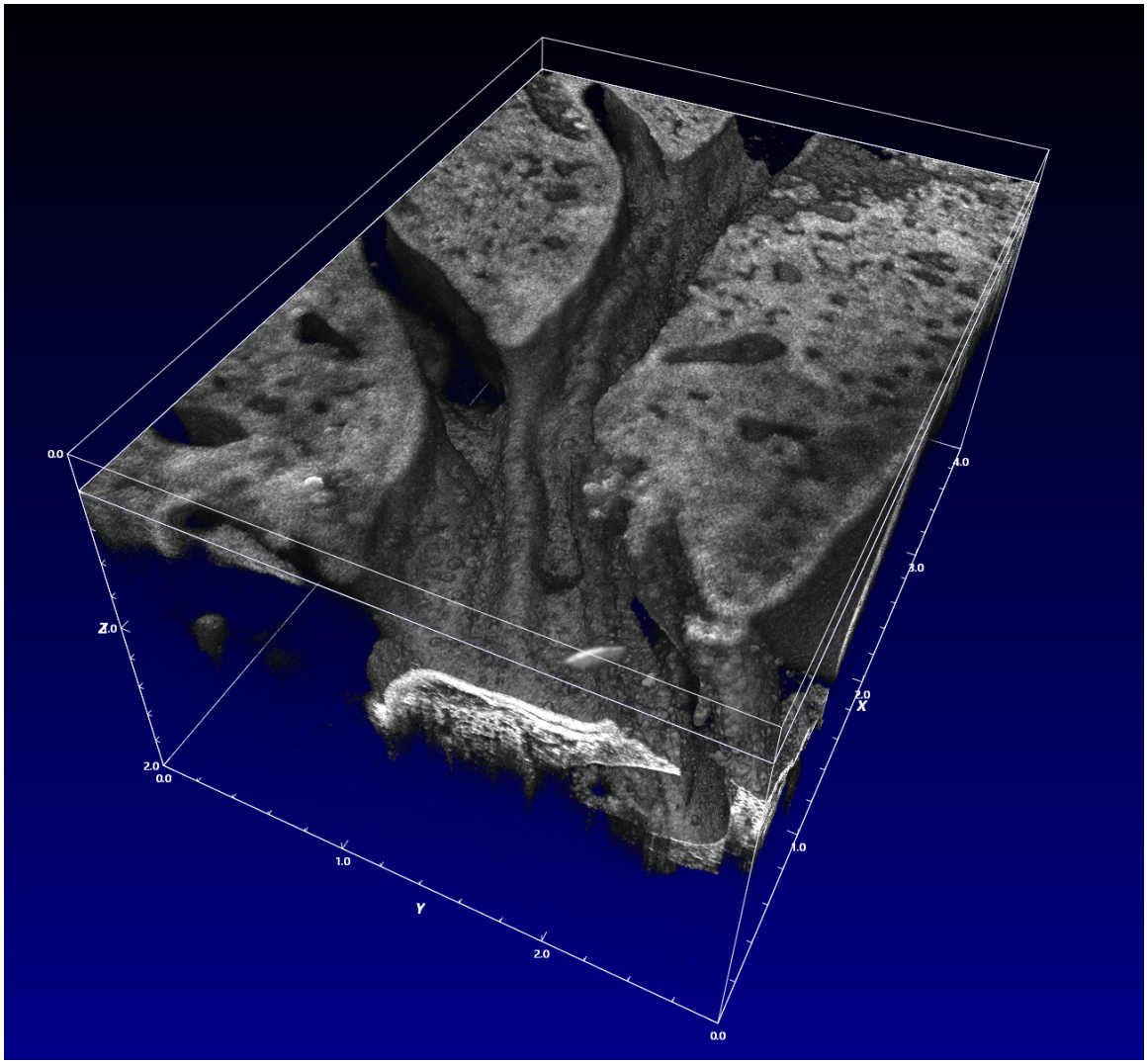

Figure 5.3: Volumetric rendering of the central airway with several folds and branches visible.

5.2.2 PS-VIS-OCT Imaging of the Lung and EBS-based Scattering Quantification

Before cryopreservation, basic PS-VIS-OCT images were used for an initial quantification of optical scattering properties and were correlated to EBS measurements and the results of several other measurements performed as part of the collaborative study. PS-VIS-OCT images were measured for total intensity, bulk scattering coefficient (for each polarization and the combined image intensity), and the mean free path (for each polarization and the combined image intensity). These data were computed for both the central airway and the ventral parenchyma. An example of the optical scattering measurement using VIS-OCT is shown in Figure 5.4 and demonstrates similar structure and information to that seen in the NIR-OCT measurements (Figure 5.2. The chief difference from

the NIR-OCT is the increased resolution allows greater detail and the addition of polarization adds another dimension to the data.

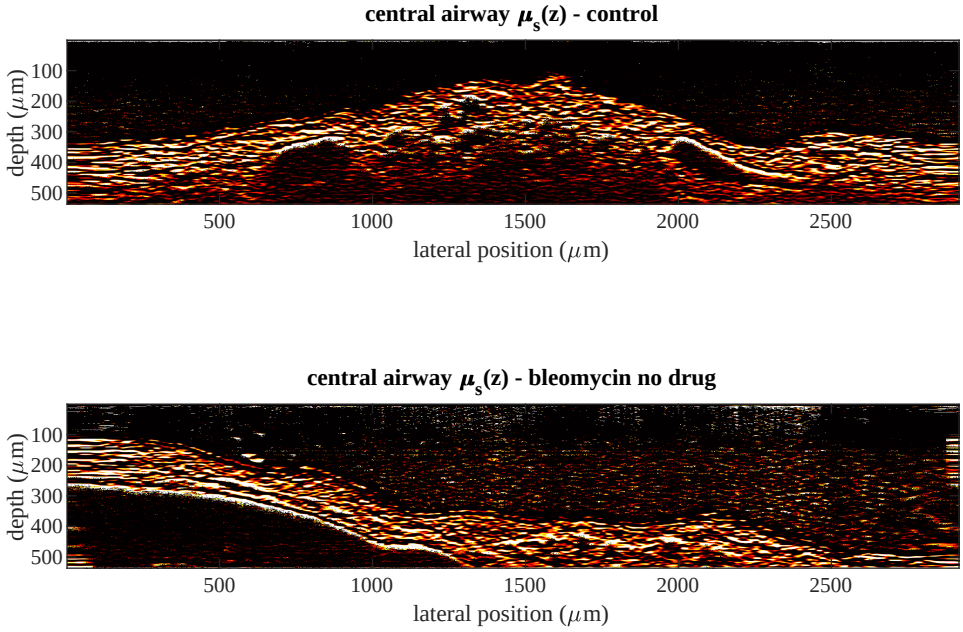

Figure 5.4: $\mu_s(z)$ image of the central airway in a control mouse (top) and a mouse treated with bleomycin and no drug for 21 days (bottom) using the total intensity of the VIS-OCT system.

Correlation with other methods of analysis were analyzed to identify potential significant trends between methods. Figure 5.5 shows the correlations between several techniques and uses color saturation to indicate increase positive (red) or negative (blue) correlation. Several interesting pairs stand out upon close inspection. Among the most notable is the tissue density measured by micro-CT. It would be expected that an increase in tissue density would correlate positively to μ_s since the scattering cross-section per unit volume would increase. However, here there is a negative correlation between the two. One explanation could be the way air or water is interpreted in both methods. In CT and micro-CT the Hounsfield unit value for air and water -1000 and 0 respectively. A given voxel containing both air/water and tissue would be skewed towards a lower value. In OCT-based measurements of optical scattering, the presence of air or water in the sample may skew the result further and ruin the measurement entirely. Furthermore, micro-CT was performed before animal sacrifice and lung perfusion. The process of perfusion could drastically

change the inflation of the lung.

Another pairing that may yield some insight is the decrease in correlation in the polarized optical scattering measured by PS-VIS-OCT. In a tissue with no birefringence, the polarization images would be identical. Given that, there would be no reason the measured scattering coefficients to differ. However, here we see a slight disparity between polarization states which persists when fitting over both a short and long range of pixels. Fitting was performed over both 50 and 100 pixels in depth in order to establish both the minimum depth of imaging needed and to assess the impact of noise by using a longer range.

After the initial imaging, the recovered samples were imaged with the PS-VIS-OCT system again to evaluate tissue birefringence. Figure 5.6 shows the per pixel retardance mapped as color onto the OCT intensity image for a control sample after 21 days. There is some variation in the measured retardance per pixel at the surface. But the signal is still within a narrow range and the stark bands seen in muscle are not present. Several interpretations of these data are possible, such as the airway not possessing significant birefringence, the birefringence not being substantial at this depth of imaging, or that the collagen distribution is too random to accumulate a coherent signal. Another possibility is that the instrument sensitivity is not sufficient to resolve the birefringence that is present.

Similarly, Figure 5.7 shows the same processing for a bleomycin-treated mouse lung after 21 days of treatment. Overall retardance per pixel appears to have decreased, which would suggest a disruption of ECM organization or a decrease in collagen density. Both of these run contradictory to the hypothesized fibrosis response. At current, more data and careful analysis is needed to interpret data correctly. To aid in this effort, SHG microscopy could be used in the mouse model samples which are still in cryopreservation. Direct imaging of the collagen deposition in the airway would be invaluable in resolving the potential birefringence of the tissue and inform PS-OCT results. A multi-modal instrument which could image with both OCT and SHG microscopy would also be a valuable tool for this study provided there is correct sample preparation. Section 6.2 describes the development of such an instrument and its applications to imaging in the eye, but the current iteration lacks the polarization-diverse detection needed for PS-OCT.

The optical scattering coefficient, μ_s, was measured using a set 100 pixel fit from the surface. Fitting can be performed with an automatic boundary of $I_{surface}exp(-1)$ or $I_{surface}exp(-2)$ where

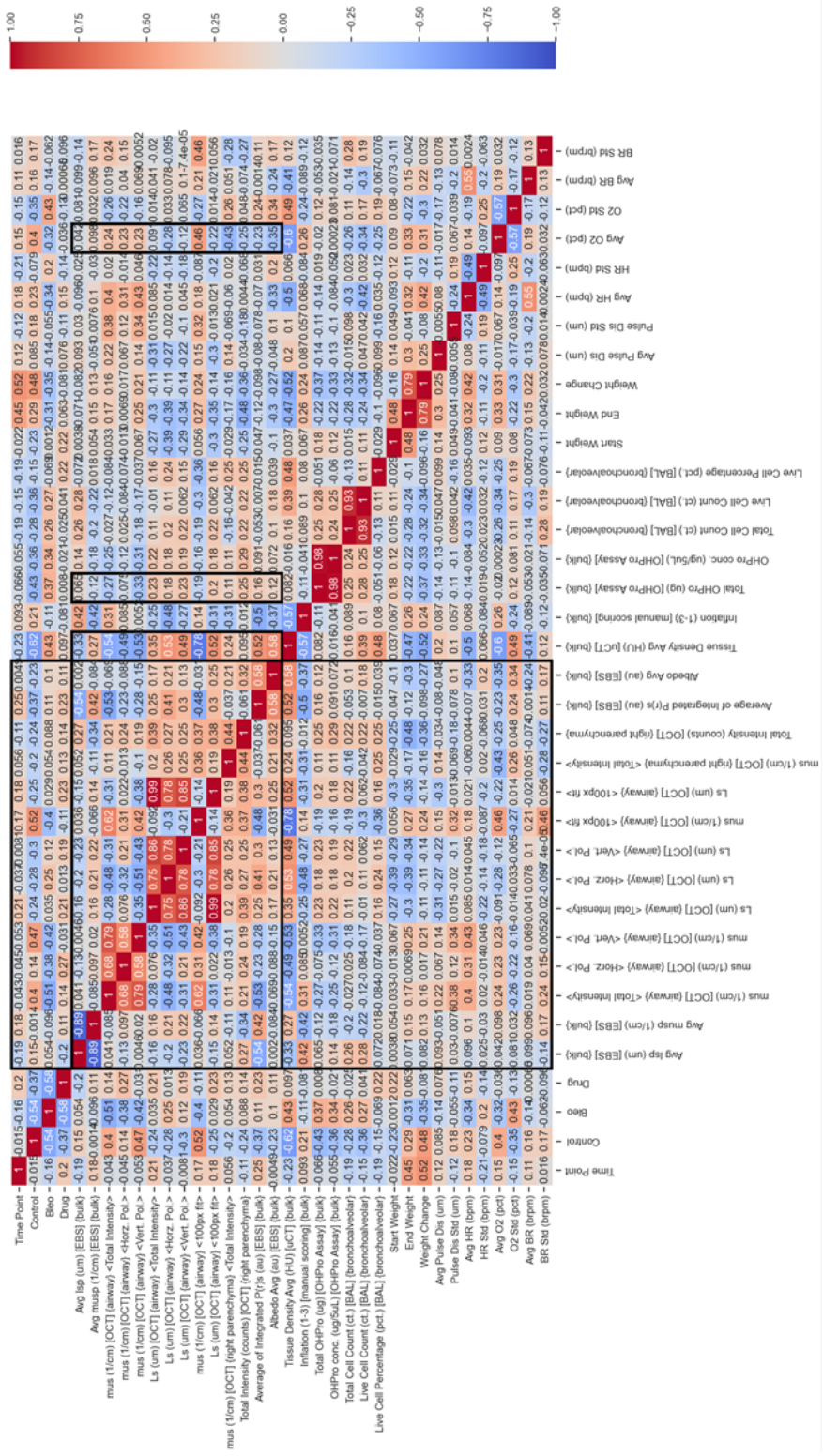

Figure 5.5: Correlations between various methods of assessment across the full study of the lung. Optical methods are outlined in the bold black boxes.

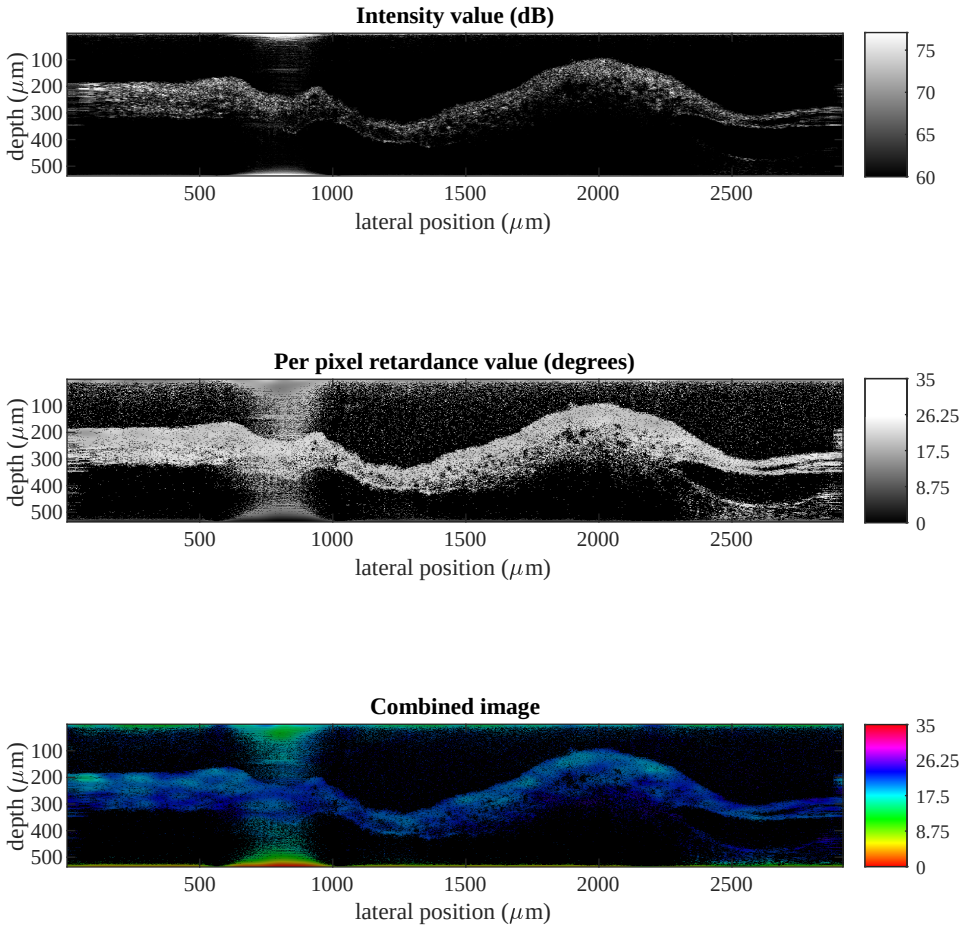

Figure 5.6: Polarization image of the central airway in a control mouse at 21 days using the PS-VIS-OCT system. Top: OCT intensity image in decibels which is used for pixel intensity. Middle: Per pixel retardance image which is used to generate hue/color. Bottom: The OCT intensity image with the per pixel retardance mapped as color.

$I_{surface}$ is the intensity at the sample surface, which corresponds to $z = l_s$) and $z = 2l_s$ respectively (recall that $l_s = \mu_s^{-1}$). This method of defining a lower boundary for fitting has difficulty measuring tissue when there are voids or gaps in tissue. Noting the porous nature of the lung, the parenchyma in particular, this method of setting a boundary will stop prematurely and be subject to greater impact from noise during fitting. To mitigate this, a manual distance of 100 pixels was set. The results in Figure 5.5 show results for 50 and 100 pixels used in fitting, however, 100 pixels was

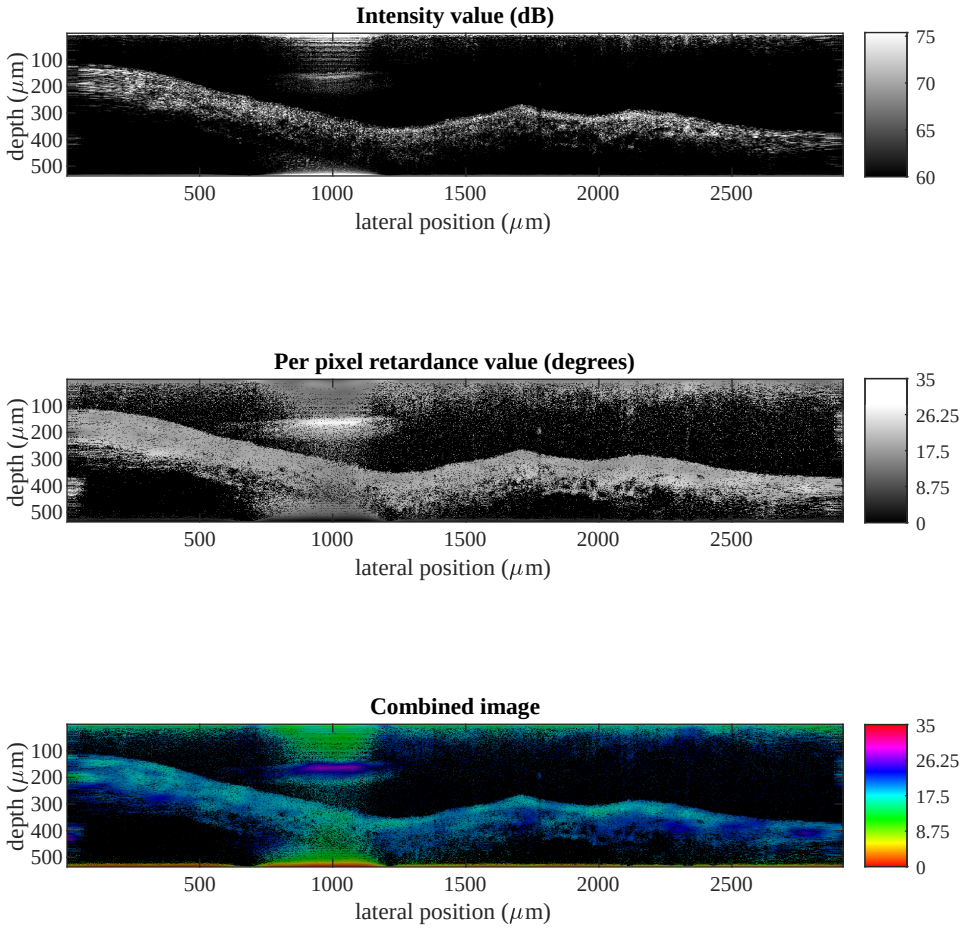

Figure 5.7: Polarization image of the central airway in a mouse treated with bleomycin and no drug for 21 days using the PS-VIS-OCT system. Top: OCT intensity image in decibels which is used for pixel intensity. Middle: Per pixel retardance image which is used to generate hue/color. Bottom: The OCT intensity image with the per pixel retardance mapped as color.

chosen since the increased number of pixels reduces the impact of noise during fitting. The results of these fits from the total intensity images (combining polarization channels) in the PS-VIS-OCT taken in the central airway are shown for all groups and samples in Figure 5.8. Control samples appear to have the highest scattering at 28 days despite other data suggesting that the peak of the fibrotic response to bleomycin should occur at day 28. The interpretation of these results has several confounding factors. The fibrosis may not occur in the airway of the mouse but instead in

the parnechyma. Fibrosis may also decrease scattering by creating a more homogeneous material which does not possess as much refractive index discontinuity. Finally, it should also be considered that the imaging and optical scattering measurements were performed *ex vivo* and the process of perfusing and fixing the lungs may alter the tissue structure and reduce the scattering contrast in fibrotic tissue.

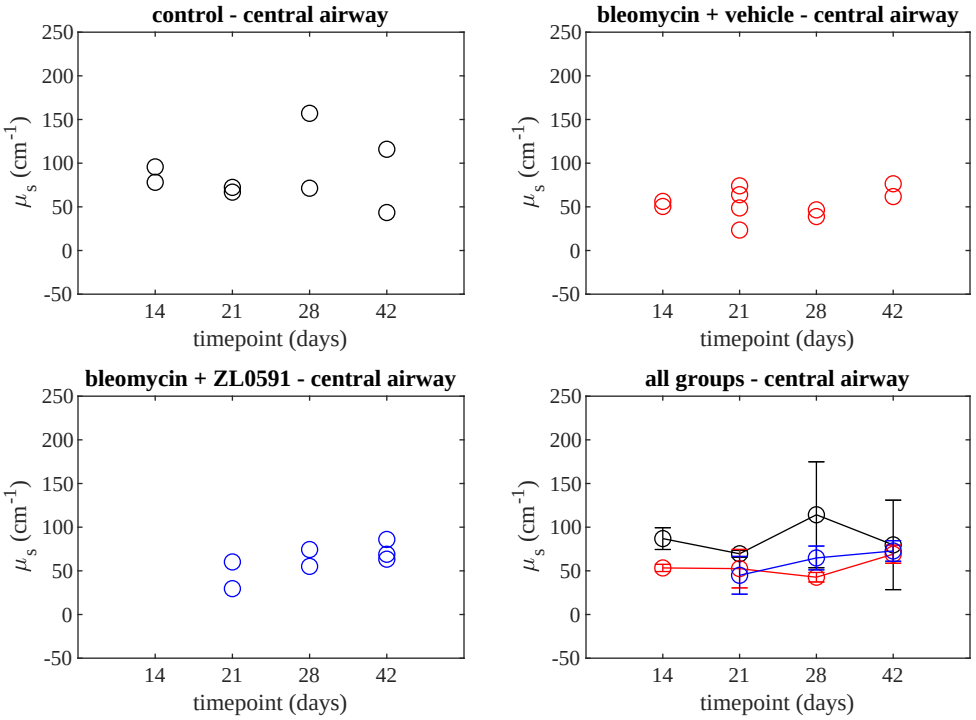

Figure 5.8: Top left: The scattering coefficient reported for control animals at all time points. Circles represent a mean value for μ_s across a B-scan. Top right: The scattering coefficient reported for animals given bleomycin but only a vehicle for all time points. Circles represent a mean value for μ_s across a B-scan. Bottom left: The scattering coefficient reported for animals given bleomycin and treated with the ZL0591 drug at all time point. Circles represent a mean value for μ_s across a B-scan. Bottom right: Samples from all groups and time points. Cirlces are mean of all samples from the group at a given timepoint with errors bars to express the standard deviation.

In addition to the airway imaging, the parnechyma was subjected to similar quantification which is shown in Figure 5.9. Image quality in the parenchyma was more uniform due to sectioning allowing more samples to be used. The changes in optical scattering were more varied but showed more trends than in the central airway. The group treated with the ZL0591 drug showed a consistent increase in the scattering coefficient across time points while the vehicle treated group showed only slight changes. The control group was varied but remained within the standard deviation of the

other groups at all time points. As with the central airway data, the interpretation is difficult. This is compounded by the need to consider inflation and perfusion of the alveoli.

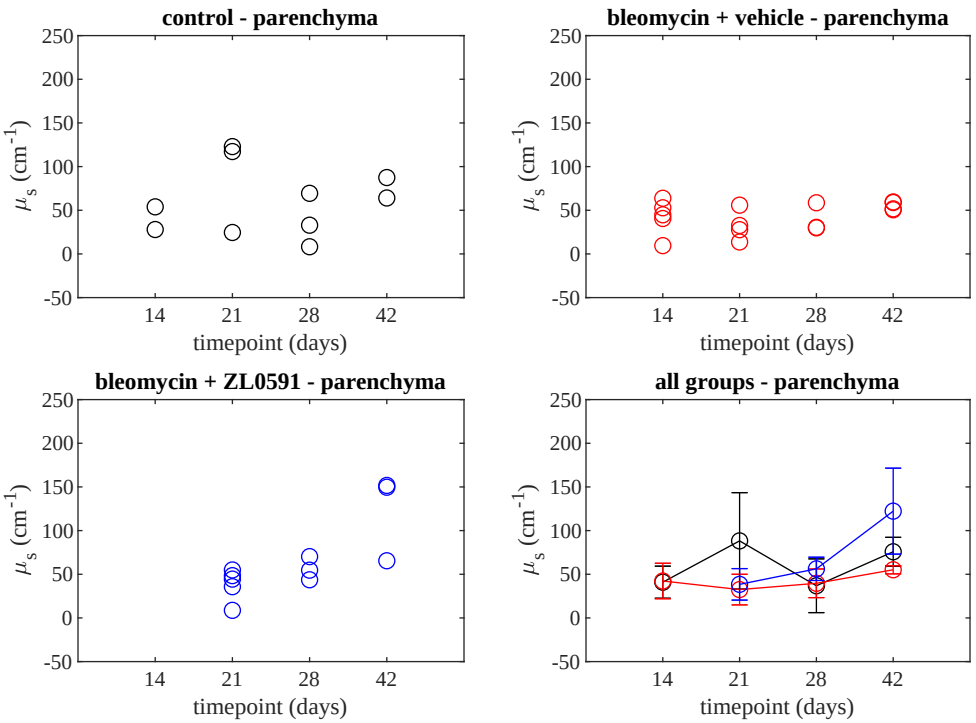

Figure 5.9: Top left: The scattering coefficient reported for control animals at all time points. Circles represent a mean value for μ_s across a B-scan. Top right: The scattering coefficient reported for animals given bleomycin but only a vehicle for all time points. Circles represent a mean value for μ_s across a B-scan. Bottom left: The scattering coefficient reported for animals given bleomycin and treated with the ZL0591 drug at all time point. Circles represent a mean value for μ_s across a B-scan. Bottom right: Samples from all groups and time points. Cirlces are mean of all samples from the group at a given timepoint with errors bars to express the standard deviation.

5.3 Refining the Optical Scattering Analysis and Future Work

While these initial results are promising, there remains a significant amount of consideration to properly interpret the data. The vast array of data shown in Figure 5.5 demonstrate the volume of information that must be processed and carefully weighted. Furthermore, refined image analysis and processing of the dual-input polarization data (discussed further in Section 7.1.1) may provide a higher sensitivity to the changes in optical scattering properties that are not apparent with the current data processing procedure.

The complex structure of the lung must be regarded carefully when quantifying the optical

scattering properties. The structural heterogeneity, like in many tissues, is present on several length scales from cellular organelles to the gross structure of alveoli in the parenchyma. Further modeling and study is needed to understand the impact of these inhomogeneities on optical scattering. In the case of the OCT-based measurements presented here, the parenchyma posed significant challenges. The presence of several voids in the tissue structure result in high scattering values at the tissue-air interface and low scattering values at the air-tissue interface. Using spatial averaging to reduce the contributions of of these interfaces, a positive correlation between the optical scattering coefficient in the parenchyma and the tissue density determined by micro-CT was observed. A negative correlation between the micro-CT tissue density measurements and the central airway optical scattering coefficient was also observed. While further investigation is needed to identify the cause of the inverse correlation, the strength of the correlation demonstrates the potential of the airway scattering coefficient as a diagnostic marker.

The increase of the scattering coefficient in the parenchyma agrees well with scattering measurements from SHG microscopy performed by the Campagnola group [142]. The SHG microscopy measurements also demonstrate a change in the scattering anisotropy, g, in IPF. Future work will aim to characterize g using OCT as well. However, because OCT does not measure g directly and instead relies on the assumptions of models [88], a novel 4π goniometry method produced by the Rogers Lab [60, 59] will be used to directly measure the anisotropy. The combination of these data aim to achieve a more comprehensive view of the changes to the tissue optical scattering and architecture. Ultimately, a more sophisticated analysis procedure must be prepared to identify what parameters have the greatest predictive power for IPF.

6 OCT as Part of a Novel Multi-modal Platform to Study the Eye

The work presented in this chapter is based on a collaborative study with Dr. Michael Pinkert, Dr. Zachary Simmons, and Dr. Bing Dai under the guidance of Prof. Tim Hall, Prof. Paul Campagnola, Prof. Jeremy Rogers, and Prof. Kevin Eliceiri. The resulting publication [144] contains a more thorough discussion of all modalities. The portion presented here consists largely of the OCT portion which was developed by the author.

6.1 The Role of Mutli-modal Imaging

6.1.1 The Need for Multi-modal Imaging in the Eye

Glaucoma can be thought of as a collection of conditions and diseases which lead to changes in intraocular pressure (IOP) [42, 28]. The change in IOP leads to death of retinal ganglion cells and damage to the optic nerve, leading to blindness [42]. The myriad of contributors to glaucoma present several challenges in diagnosis. OCT is typically used to assess the retina and has more recently been developed for high-resolution anterior ocular imaging. Additionally, genetic models of glaucoma have been developed which have changes in the biomechanical properties of the sclera [32, 43]. The sclera, being composed primarily of collagen, is also an easily accessible site for high-throughput, non-invasive screening for optical imaging methods sensitive to tissue birefringence [145].

To assess collagen remodeling in the sclera and its association with glaucoma in a feline model, NIR-OCT was used along with enhanced backscattering spectroscopy (EBS), second harmonic generation (SHG) microscopy, and micro-ultrasound (μUS) to better understand the development of glaucoma.

6.1.2 Multi-modal Imaging and Functional OCT

Functional and multi-modal OCT has been pursued in several forms including fluorescence [146, 147], coherent anti-Stokes Raman (CARS) [148], and SHG [149] OCT. These variations are typically referred to as Molecular OCT due to their imaging specificity. Incoherent fluorescence can be collected from OCT imaging for use in techniques such as fluorescence lifetime imaging [146] and fluorescence molecular imaging [147]. The addition of fluorescence can add useful dimensions of information but requires separate illumination sources due to the spectral separation needed

between broadband OCT illumination and the fluorescence emission. The use of multiple illumination sources and detectors requires image co-registration which is made straightforward by the use of common-path scanning optics. Additionally, axial resolution of the fluorescence signal is not achieved without some method of optical sectioning such as a confocal pinhole.

As opposed to incoherent fluorescence, nonlinear optical interactions such as CARS and SHG retain coherence with the excitation field. A key advantage of this is that the same source can be used to generate an OCT (or fundamental) image and a secondary image. In order to investigate the role of collagen in disease, a combination of SHG microscopy and OCT was an ideal candidate. Previous work from the Chen group and the Izatt group demonstrated a novel incorporation of SHG microscopy and OCT in 2003 [150] and 2004 [149], respectively, using a time-domain system with the Izatt group shifting to a Fourier-domain system in 2005 [151]. Briefly, the fundamental OCT interferogram was achieved in the typical way using a NIR source with sufficient power to achieve SHG. The SHG signal was directed to a second spectrometer where it interferes with an SHG reference arm and produces a co-localized "OCT" image of collagen. This method combines the tissue contrast, resolution, and scale of OCT with the molecular specificity of SHG microscopy. The use of the same illumination source and scanning optics leaves the images innately co-registered, however the low NA used in OCT will impact the SHG microscopy images accordingly. Work in 2004 from the So group [152] demonstrated high NA SHOCT that had superior lateral resolution, but at the cost of axial range of imaging. Multi-modal system design will contain several compromises in imaging resolution, speed, field of view, image co-registration, and more. The criteria of the application will often dictate the desired capabilities of the system. To study collagen and its organization, a multi-modal imaging platform was designed to combine high-resolution SHG, OCT, micro-ultrasound, and enhanced backscattering spectroscopy.

6.2 Integration of OCT with other modalities: A multi-modal imaging platform

6.2.1 Instrument Overview

Imaging over several size scales and using different sources of intrinsic contrast is a nontrivial task. Typical instrument design recognizes the trade-offs between resolution and field of view, speed of acquisition and noise, and combination with complementary optics and detectors. The

Method	SHG	OCM	μUS	EBS
Lateral Resolution (μm)	0.9	7.5	110	.030
Axial resolution (μm)	8.8	25	100	.030
Single Lateral FOV (mm)	0.75	2.00	≈ 14	3
Axial FOV (mm)	< 0.25	1.20	≈ 5	1
Contrast source	collagen	scattering	structure	scattering

Table 6.1: Each modality offered differing levels of resolution and field of view. Additionally, contrast from each method was similar and interrogates sample structure. Importantly, each method uses intrinsic contrast, allowing for minimum sample manipulation before imaging.

design of this system aimed to minimize the compromises necessary by unifying the optical design to be as complementary as possible. For the micro-scale, SHG microscopy was incorporated for its specificity to collagen and high resolution. Meso-scale imaging was achieved using an optical coherence microscopy (OCM) system which provided a larger field of view with poorer resolution compared to SHG, but offered image contrast based on optical scattering. The macro-scale imaging was achieved using μUS, which provided the largest scale of imaging and would also not require any contrast agents or labels. Finally, EBS was incorporated into the system to interrogate the optical scattering arising from the sample ultrastructure. These methods have been tabulated below (Table 6.1) and, once incorporated and co-registered, allowed for multi-scale imaging of samples on a single platform with no required sample preparation.

The final instrument design, shown below in Figure 6.1, relied on efficient use of common optical paths and a well-engineered platform to achieve its goals. The first key principle was to combine SHG and EBS illumination, which was convenient and is discussed further in Section 6.2.2. Critically, the OCT was folded into the beam path to make use of the SHG scanning optics by using a parfocal objective for illumination. The convenience of both methods utilizing the same scanning optics cannot be understated as it mitigated most of the difficulty in image co-registration. Finally, the mechanism for moving the sample relative to the optics and transducer could be precisely controlled, allowed for image co-registration and coordinate transform with a single fiducial phantom with known dimensions. To preserve the high resolution and intrinsic optical sectioning of SHG microscopy, the multi-modal system here was designed to have independent illumination and detection paths. While more complex, this approach preserved SHG resolution and allowed the component systems to be approached and upgraded separately.

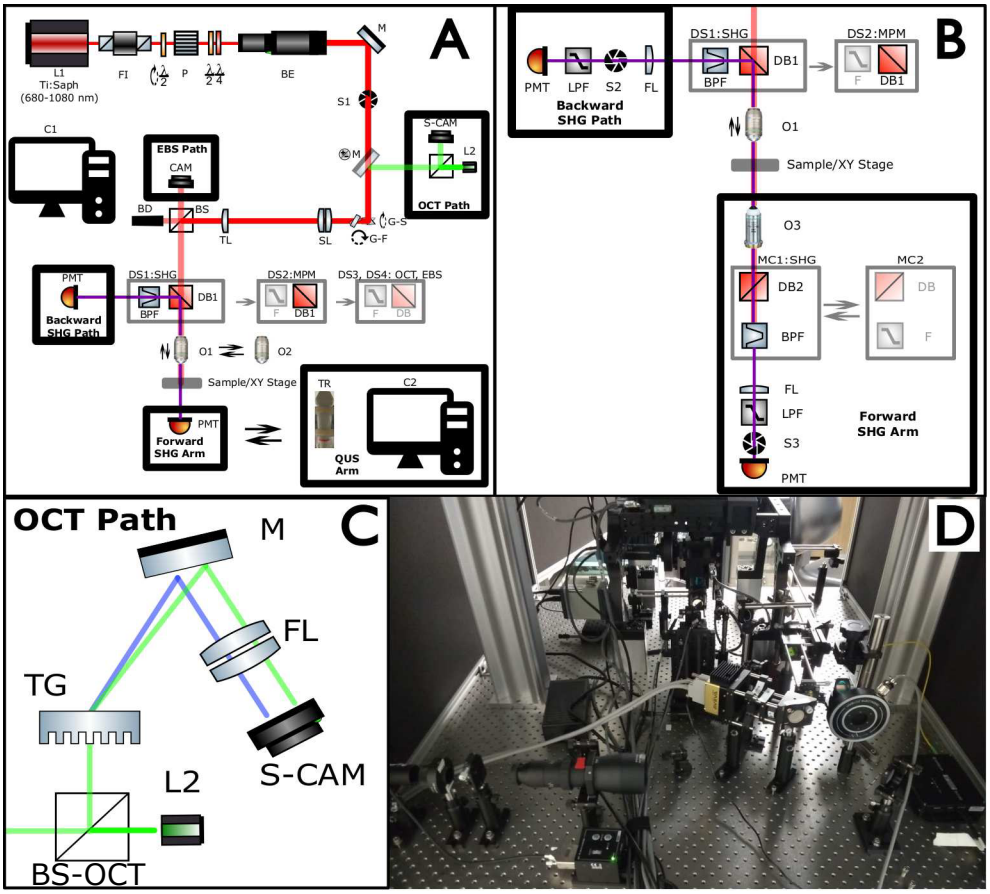

Figure 6.1: Multiscale imaging platform design. (A) Optical diagram of the main beamline, with simplified component boxes for each imaging arm. (B) Schematic diagram of the Multiphoton Microscopy imaging arm. The system switches between the modalities with a filter slider in the backwards position and a filter cube in the forwards. (C) Schematic diagram of the OCT arm. (D) Back photograph of the central beamline, galvos, and OCT imaging arm. The full description of the components is in the text.

Figure 6.1 displays schematic diagrams and photographs for the system. The diagram in Figure 6.1A displays the overall platform design. The imaging arms for Multiphoton Microscopy are depicted in Figure 6.1.B. The diagram for the OCT imaging arm is depicted in Figure 6.1.C. A photograph displays the arrangement of optical elements on the table in Figure 6.1.D. The light source for MPM and EBS imaging is a 3.5-W femtosecond Titanium:Sapphire laser (Chameleon Ultra II, Coherent, Santa Clara, CA) (L1) with a wavelength range of 680-1080 nm and an 80 MHz repetition rate. Back-reflections are prevented using a Faraday Isolator (I-7090, Isowave, Dover, NJ) (FI). The power output of the laser is modulated using a rotating half-waveplate leading into a polarizer (MWPQA2, MGLA12, Karl Lambrecht Corp, Chicago, IL) ($\lambda/2$, P). Circular polarization

is set using a half- and quarter-waveplate (MWPQA2 and MWPQA4, Karl Lambrecht Corp) ($\lambda/2$, $\lambda/4$) to obtain uniform SHG signal with fiber angle [33]. The main beam is expanded (BE02, Thorlabs, Newton, NJ) (BE) and shuttered (VS14, Uniblitz, Rochester, NY) (S1) before being integrated with the OCT laser (L2 described in section 2.4) via a flip mirror. The beamline then leads into independent fast/X scanning and slow/Y scanning galvanometer mirrors (62xxH series, Cambridge Technology, Bedform, MA) (G-F, G-S). The galvos direct the beamline through a pair of adjacent achromatic lenses (LBF254, Thorlabs) that act as a scan lens (SL) ($f_{effective} = 50$ mm), placed 50 mm from the galvos (G-F). A tube lens ($f = 200$ mm) (LA1541, Thorlabs) (TL) is placed 150 mm beyond the scan lenses.

This is followed by a Modular Infinity Microscope (MIM, ASI Imaging) housed on a Rapid Automated Modular Mounting (RAMM, ASI Imaging) frame. The beamsplitter (BS) redirects the beam upwards and functions to direct backscattered light from the sample into the EBS collection path. A beam dump (BT600, Thorlabs) (BD) captures the transmitted light. The illumination light passes through a 4-position dichroic slider (DS) capable of holding a square diagonal mirror and a circular filter at each position. Positions 1 and 2 are configured for SHG and MPM respectively. Both positions contain a long pass dichroic beamsplitter (FF685, Semrock, Rochester, NY) (DB1). The filter slot for Position 1 is fitted with a band pass filter (445/20 nm, Semrock) (BPF). The motorized objective turret is fitted with a 20x magnification 0.75 Numerical Aperture (NA) air objective for SHG and MPM (Plan Apo VC, Nikon, Tokyo, Japan) (O1), a 4x magnification 0.13 NA objective for OCT (N4X-PF, Nikon) (O2), and an empty aperture for EBS. The objective leads to a motorized XY stage and a sample holder insert (Sample/XY Stage) for either slides or glass bottom dishes, where the latter are required for US. The Forward SHG imaging arm and the US imaging arm are mounted on a manual rail, with stops in either position. Finally, all optical detectors, stages, and lasers are controlled through a computer (C1). The US transducer is controlled through a separate computer (C2).

6.2.2 Design Considerations

A combination of these methods was created on a single microscopy platform for co-registered volumetric image acquisition. Combining these modalities on a common sample stage presented a nontrivial challenge from an optics and engineering perspective. The primary design constraints

were the geometry of the platform and incorporation of the ultrasound. Ultrasound requires a transducer to be in contact with the sample and, for liquid immersion (to prevent sample dehydration), is best done from the top. This required the bulk of the microscopy optics to be in an inverted microscope geometry.

The use of inverted geometry presented a unique engineering challenge to each modality. Typically, SHG microscopy is performed with both a forward and backward detection channel and uses optically thin samples. Adapting this to the multi-modal geometry required mounting a detection arm (PMT) on a movable arm with the ultrasound transducer, functioning analogously to an objective turret on a traditional microscope. Illuminating along the inverted microscope allowed the backward channel to be constructed conventionally using a dichroic and PMT. Two other critical requirements for SHG presented confounding factors. The first was the need for circularly polarized NIR illumination, which required OCM and EBS designs to shift source central wavelength to the NIR to be compatible with the scanning and dichroic optics. The second critical requirement was the sample mount, which directly impacts SHG efficiency. As mount thickness increases, SHG signal will decrease, requiring the thinnest mount possible on the order of 150 μm and for its orientation to be flat.

Mitigating these challenges was straightforward, albeit technically difficult in the EBS design. Source wavelength and bandwidth can be matched to the optics somewhat easily. And conveniently, EBS prefers circular illumination for its increased penetration depth and its utility in filtering reflections. Thus the circularly polarized NIR illumination for SHG was compatible with EBS. The flat orientation of the sample mount, however, significantly interferes with EBS signal collection as it produces specular reflections which are difficult to filter without significant loss, due to there being no wavelength shift for EBS to leverage using dichroic filters. Typically, this loss is mitigated by tilting the EBS sample mount off axis to reject specular reflection from the low angular field of view of the detector. However, for an instrument designed around image co-registration, changing the sample mount tilt was undesirable. Ultimately, the solution was to move EBS to the final step of the work flow and introduce sample tilt with minimal disturbance to position. This compromise is thought to be technically sound since EBS interrogates samples with a relatively large, collimated beam (approximately 3 mm), meaning the local interrogation of optical properties will still match the SHG and OCM field of view.

The challenges presented to the OCM design were also substantial. The inverted geometry and requirement for a thin sample mount led to specular reflections as mentioned in the EBS design considerations. As discussed in Section 2.4.1, axial range of imaging is proportional to the spectrometer resolution or the coherence length of a single pixel which can range from 0.5 mm up to more than 2 mm. Because of this extended FOV, it is possible for internal reflections from the sample arm to interfere and confound the image signal. This complicated the design of a traditional OCM system and required the use of common-path geometry. This is discussed further in Section 6.2.3.

6.2.3 Common-Path OCT and Linnik Interferometry-based OCM

Typically, OCM uses a Linnik interferometer as opposed to the Michelson interferometer which is typical of OCT. The critical difference in these schema is the incorporation of identical objectives into both the sample and reference paths. These objectives focus the beam on the reference and sample reflectors and have the benefit of matching any dispersion or aberrations between the arms. There is an added measure of difficulty in this technique, however. The reference reflector must be kept at the focus of an objective, requiring the objective and reference reflector to be moved simultaneously. While this may not appear to be a difficult task, the long path lengths involved in the system meant any deviation from focus would produce a significant beam divergence or convergence.

The initial multi-modal design intended to use Linnik interferometry to power the OCT arm. However, difficulty in aligning the reference arm presented a significant challenges, particularly to new users. A more substantial problem was observed with the Linnik-based system as well. The axial range of imaging was found to be greater than the optical thickness of the sample mounts required for SHG microscopy, the aforementioned 150 μm dish. Because of the dish's flat orientation for SHG microscopy and the inverted microscope geometry, the produced specular reflections created several autocorrelation images from the sample arm, see the $E_s E_s^*$ term in Eq. 21. In this situation, we turn this reflection to our advantage and use it as the reference for a common-path OCT. Conveniently, common-path OCT has the benefit of eliminating system dispersion [153], which is typically digitally corrected in conventional OCT. This common-path OCT system geometry is compatible with the SHG, TPEF, and US components.

6.2.4 Final OCM System Design and Evaluation of Performance

The optical diagram for the OCT arm is displayed in Figure 6.1.C. A coherent light source (860 nm SLD, SuperLum) is collimated (F280APC-850, Thorlabs) (L2) and directed into the laser scanning optics (Figure 6.1.A). A low NA objective (Nikon 4x plan fluorite, Thorlabs) (O2) collects backscattered light from the sample and sample-glass reference [154]. This backscattered light is directed using a beamsplitter (BS-OCT) into a transmission grating (TG) which spectrally separates the interference. The first order diffraction is collected by a 150 mm focal length lens (FL) and focused onto a line-scan camera (AViiVA em4, Teledyne e2v, Essex, England) (S-CAM). The interferogram for each scan position is recorded as a function of wavelength. Interpolation of the interferogram into k-space ($2\pi/\lambda$) followed by Fourier transform recovers the signal in depth (also referred to as an A-line). An A-line is collected for each scan position in one lateral dimension (also referred to as a B-scan) and is used to build up a complete volume image of the sample. Camera exposure is set by the pixel clock time for Nyquist sampling in the

OCT lateral resolution follows the conventional diffraction limit for a given objective. Objective NA can be artificially lowered by underfilling the back of the objective which increases depth of focus at the cost of lateral resolution. The full NA of the objective was used in this application to maximize the lateral resolution. The galvo size and magnification of the scan and tube lens fix the beam diameter at 12 mm, giving a total NA of 0.13 and lateral resolution of 3.9 μm. Imaging a United States Airforce Bar Target (1951 USAF Negative Bar Target, Edmund Optics) provides a demonstration of the OCT lateral resolution and FOV (Figure 6.2). Lateral resolution as assessed by the slanted-edge method demonstrated 7.5 μm [155].

OCT axial resolution and axial range of imaging is governed by source bandwidth and spectrometer resolution, respectively [156]. Axial resolution is calculated as $(2ln(2)\lambda_0^2) = (\pi\Delta\lambda)$, where λ_0 is the mean wavelength and $\Delta\lambda$ is the bandwidth measured as the FWHM of the source spectrum [84]. Using our source, we have an expected axial resolution of 10 μm. Our spectrometer design gave us a spectral sampling of 0.17 nm per pixel, providing an axial range of approximately 1.2 mm and a digital sampling of the axial range of 7.15 μm. The depth of imaging within a sample in OCT is limited by objective depth of focus, spectrometer-dependent fall-off, and sample-dependent attenuation. The depth of focus of the objective was calculated as 110 μm [84]. The fall-off in depth

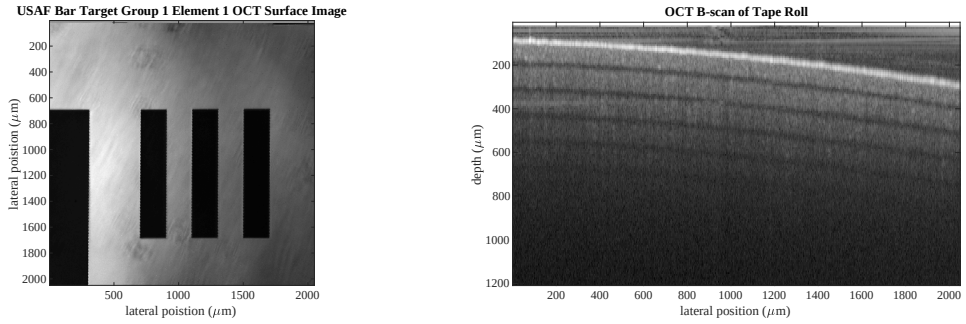

Figure 6.2: **Left:** USAF 1951 Bar Target surface image reconstructed from OCT volume. Pictured is group one, element one. **Right:** OCT B-scan of rolled Scotch tape (3M, Maplewood, MN). Image demonstrates up to 500 μm of imaging depth in a scattering material. Imaging depth was also well-preserved across the curved surface of the sample.

for OCT intensity also depends on the spectrometer and has been well characterized [157, 87]. The signal in our spectrometer decays to 50% of its maximum value at approximately 250 μm. Combining all sources of signal fall-off has been done previously and can be observed to depend on the position of the depth of the objective focal plane [86]. The impact of these factors are discussed further below, but can be well-summarized with the 6 dB fall-off depth and was measured as approximately 300 μm when the focus was moved with the specular reflection, which agrees well with the spectrometer-based roll-off. The 6 dB fall-off depth can also be calculated according to [84], which was approximately 340 μm for this system and agrees well with this measurement. Rolled tape is a common OCT phantom which demonstrates axial resolution, axial range, and depth of imaging [101, 158]. Figure 6.2 demonstrates visibility of five or more layers when the sample is mounted on a standard 1 mm microscope slide and with no corrections for signal decay. Images of an air-glass interface had a FWHM of approximately 25 μm in depth while the surface of a strongly scattering material (tape) had a FWHM of 15 μm.

A sample image of the sclera in a rabbit eye in Figure 6.3 demonstrates the imaging capabilities in tissue. The OCT system acquires a 3D volume, corresponding to an A-line for each sampling point, and allowing reconstruction of B-scans along the X or Y axes. Full imaging volumes can be processed to reconstruct a surface image of the tissue.

The OCT design was constrained primarily by the light source, the objective, and the need to conform to the SHG, TPEF, and US geometries. A near-infrared superluminescent diode with a central wavelength of 860 nm (FWHM of 30 nm) was used to minimize noise and to provide

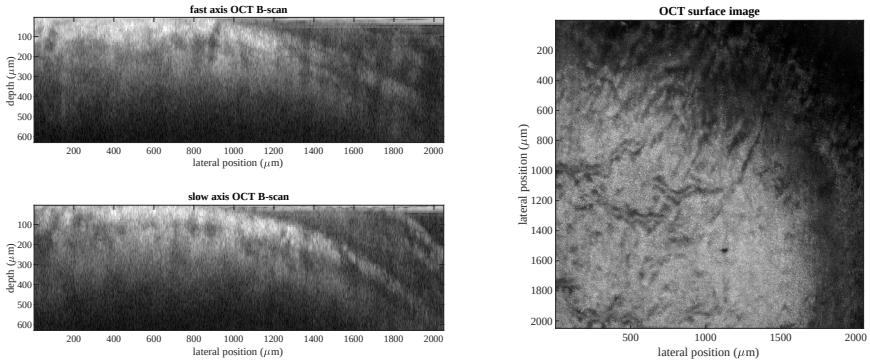

Figure 6.3: **Left:** OCT B-scans of the sclera. **Right:** Example OCT surface image data.

adequate axial resolution over a 1 mm of axial range of imaging. OCT axial range is limited by the resolution of the spectrometer and the axial resolution is limited by the bandwidth of the source. Without the use of a telescope between the beamsplitter and grating, the spectrometer resolution is limited by the size of the galvos which in turn limited the number of lines illuminated on the grating. In this case, a 600 lines/mm grating was used for the 3 mm galvo mirrors. The dispersed spectrum is focused onto the camera by a 150 mm lens giving a diffraction limited spot of approximately 40 μm. The line-scan camera is a linear array of 2048 square 14 μm pixels. While this design oversampled the spectrum, the spectrometer resolution was sufficient for a 1 mm axial range. Both the spectrometer resolution (and thus axial range) and the efficiency of the pixel illumination could be improved by using a telescope to expand the beam before illumination of the grating, however the constraints of the objective and microscope geometry imposed greater restrictions, including the confocal fall-off [72].

The OCT objective and its NA were the primary factors governing the imaging depth in samples. The 4x 0.13 NA Nikon objective was chosen to allow the OCT image plane to be parfocal with the other microscopy modalities. The objective was filled completely by the 3 mm galvos with beam expansion to maximize lateral resolution. Due to the full NA of the objective being used, the depth of focus was reduced as described above . The combination of spectrometer-based sensitivity fall-off and the confocal PSF reduce the image intensity by half at a depth of 200 μm when the objective is focused at interface between the coverslip and sample. Focusing the objective into the sample will reduce the overall image intensity but provide a more even illumination of the sample. When the focus is placed 300 μm into the sample, the depth at which the image intensity falls to

half extends from 200 μm to 375 μm. The maximum depth of imaging in samples was on the order of 500 μm, which was sufficient for this intermediate-scale application.

While the depth of imaging is small compared to other OCT systems, the use of common-path detection and microscope integration was a nontrivial restriction in the OCT design. The depth of imaging was limited by the thickness of the required sample mount for SHG microscopy, where using a 1.5 coverslip glass bottom dish limits the depth to approximately double the optical path of the thickness of the glass bottom dish or approximately 450 μm. The limitation occurs due to duplicate images in the axial range, arising from reflections at the front and back surfaces of the glass bottom dish. These reflections can be segmented out in post-processing provided there is at least some separation between them, as was the case in the system presented here. Future improvements in OCT signal fall-off in depth would need to be balanced with this separation kept in mind. This limitation to the depth of achievable imaging was not considered critical, as the role of OCT was to offer an imaging modality on an intermediate size-scale between SHG and ultrasound.

6.3 Multiscale Imaging of a Rabbit Eye

This section demonstrates the system's multiscale imaging capabilities through an example dataset on a common sample for all modalities. Our criteria for the common sample was a tissue that has structure and characteristics of interest for all the instrument modalities. For this purpose, a rabbit eye is an excellent demonstration sample. The sclera is largely composed of fibrillar collagen and exhibits strong SHG signal [159]. This collagen structure should be reflected in OCT, alongside other tissue components that have no SHG contrast. The eye is also a subject of numerous ultrasound studies investigating diseases ranging from melanoma to vision loss [160, 161, 162, 163], and for demonstration purposes reveals internal structures such as the anterior chamber, lens, and angle. The sclera, usually appearing white, is highly scattering and so has a strong EBS response (see Figure 9 in the published manuscript [144]).

6.3.1 Sample Preparation

Juvenile albino rabbit eyes were obtained at the time of sacrifice from an unrelated study using rabbits that was approved by the University of Wisconsin-Madison's Institutional Animal Care and Use Committee. All eyes were fixed overnight in 4% PFA after extraction.

One eye was placed in a custom glass bottom dish made out of acrylic, with a #1.5 glass coverslip bottom, and fitted to a large petri-dish stage insert (I-3088, ASI Imaging, Eugene, OR). The eye was then embedded in a 2% agarose solution by applying light pressure from the top of the eye to prevent it from floating and then filling the chamber with agarose. Once the agarose congealed, phosphate buffered saline was poured over the eye to give US a water-coupled path. This embedding ensured that the eye would not shift during imaging. The eye was imaged in place for SHG, US, and OCT. However, for EBS imaging the dish had to be removed and re-inserted over the shim.

6.3.2 Imaging Parameters

The agarose embedded rabbit eye was imaged with SHG, US, OCT, and EBS. Due to the disparities in scale and image orientation, each modality imaged the whole accessible volume of the eye. A single SHG image represents only a few US voxels, and so any statistical comparison between SHG and US requires many stitched SHG images to obtain a sufficiently large volume. In addition, the US and images are perpendicularly oriented to the SHG images, and so acquiring images over the SHG volume similarly requires a large number of B-scan US images in order to form a C-scan image in the region of interest. The SHG image was acquired as a 22 x 17 grid of 512 x 512 x 33 images with a sampling resolution of 1.02 x 1.02 x 20 μm. The tiles were stitched into a FOV of 8.46 x 10.94 x 0.66 mm in X/Y/Z. The images were taken at a 200 kHz sampling rate, yielding an overall imaging time of approximately five hours.

The US image was acquired as a series of B-mode scans with a transmit and receive focus of 14 mm, a transmit F/# of 6, and a receive F/# of 3.6. Each B-mode scan acquired an image in a 2D X x Z plane of 4 x 19mm, corresponding to the X and Z axes of the optical imaging. The acquisition obtained 40 raylines around the central 40 transducer elements, in order to avoid the noise from asymmetry mentioned in section 3.2. There were 6 x 233 slices, separated by 3733 μm X spacing and 100 x Y spacing, for a total FOV of 22.71 x 23.3 x 19.05 mm. The US imaging took approximately 15 minutes.

The OCT volumes were acquired using co-registration of the ultrasound and multiphoton scanning grid. A mosaic of OCT volumes provided a 10 mm by 10 mm lateral FOV with approximately 500 μm axial range of imaging. Each OCT volume was acquired at 50 kHz sampling night, which

resulted in an overnight acquisition taking approximately 16 hours.

EBS images were obtained as stacks of 10 images for averaging. The sample was manually rotated (EBS measurement was performed first of the modalities) about the center of the beam to suppress speckle. A background image of a black background and a low-scattering scan for flat-fielding were also obtained during the same session. The EBS image acquisition took approximately five minutes, including setup.

The whole imaging procedure took place over two days, starting in the morning and finishing in the late afternoon of the next day.

6.3.3 Multiscale Eye Imaging

The images from each modality were registered using the procedure described in the publication [144] and the results are depicted in Figure 6.4. The multiscale image shows a clear correspondence between the gross curvature of the eye bottom in US, in SHG, and in OCT (Figure 6.4.A, B, E) Further, finer scale anatomical correspondence can be seen in the higher resolution SHG and OCT images (Figure 6.4.C, F). In addition, the EBS peak depicted in panel (D) displays the illumination scattering response of the EBS peak in the graph and an inset of the EBS camera image.

6.3.4 Evaluating System Performance

This system is a significant advance for multiscale imaging. It demonstrates several new multi-modality combinations and enables a range of multiscale imaging studies. To our knowledge, it is the first system to merge a low-frequency (< 20 MHz) linear-array US imaging with SHG or TPEF; this makes the instrument valuable for studies using external US probes and any US parameters available on multi-element (clinical/pre-clinical) imaging systems [164, 165, 166]. Several groups have developed endoscopic probes merging high-frequency (> 20 MHz) single-element US and optical imaging, but these devices have FOV and speed limitations and cannot perform multi-element acquisitions [167, 168, 169]. In addition, this system is the first time that EBS has been incorporated into a microscope or used alongside other modalities. This combination of modalities is sensitive to structures at sub-optical resolutions, and it resolves structures at the micro, meso, and macro scales. EBS is complementary to the other modalities in this instrument. Having

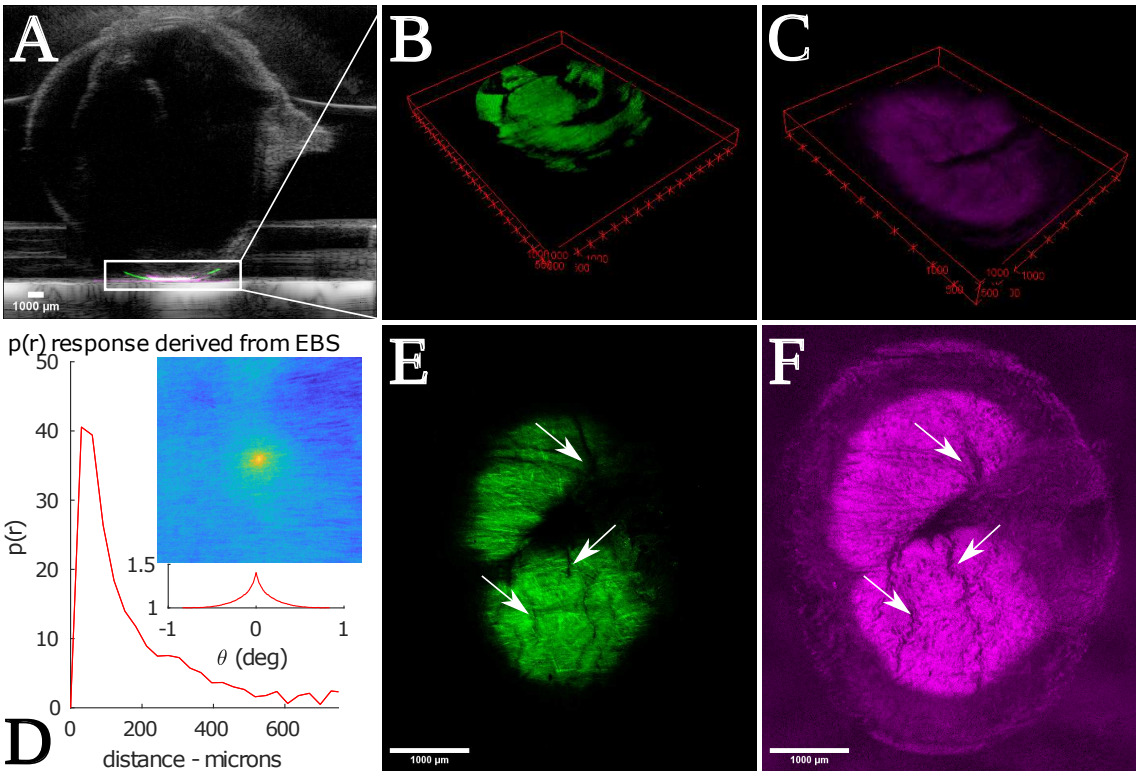

Figure 6.4: Multiscale image of a rabbit eye sclera. (A) A B-mode US image of the eye is overlaid with registered SHG (green) and OCT (magenta) images. (B, C) 3D visualizations of the SHG (B) and OCT (C) from above. (E, F) A close up of the SHG (E) and OCT (F) images from below shows similar biology between the two modalities, with corresponding seams pointed out by white arrows. (D) The EBS image and corresponding illumination scattering response. The curvatures of the SHG image match that of the US image. At higher resolutions, the OCT and SHG images depict corresponding physical structures. The scale bars in A, E, and F are 1000 μm wide, and the tick marks in B and C are 500 μm spacing.

the EBS channel common with the optical imaging modalities allows the opportunity to correlate small structural changes that may present in imaging modalities with EBS signal changes. Both SHG and OCT exploit tissue properties to create contrast and images but do not natively report scattering parameters. As a result, scattering information derived from ultrasound and EBS is valuable to efforts to derive quantitative information in these imaging modalities. For example, scatting information from bulk samples measured with all optical modalities could potentially be mapped to imaging volumes too small to measure with EBS.

We have shown that the system contrast can differentiate between structures in the eye and that it can produce co-registered images across these multiple imaging scales. This example showed clear structural similarities between OCT and SHG, while also showing that OCT detected regions of

low-collagen that SHG could not. In addition, we have shown how the EBS peaks can differentiate between regions of tissue and between the same region with different scattering properties. This instrument thus facilitates studies that investigate phenomena link between subcellular composition to macroscale tissue properties.

The system has several limitations. The main limitation is the area of tissue that can be directly compared between the optical modalities and US. The optical imaging can only penetrate a few hundred micrometers, depending on the scattering properties of the tissue, whereas the US system has an axial resolution of approximately 100 μm. This means that the optical region of interest is only a small segment of the US image, right where the tissue rests above the glass. The full thickness of tissue scanned with ultrasound cannot be directly correlated to the less-penetrating optical modalities. Another limitation is imposed by the glass bottom dish, which affects the US, OCT, and EBS imaging arms. The US clutter noise from the glass bottom limits the image quality near the glass surface. The noise can be reduced at the expense of SNR and resolution by using smaller apertures for transmit and receive. It will be the focus of future work to investigate other approaches for dealing with this noise.

7 Future Directions and Conclusions

The work presented in this thesis aims to establish the use of multi-channel detection for VIS-OCT. Careful design of instrument geometry can maximize each frame readout from a large detector. The studies conducted here demonstrate the utility of such instruments, but further improvements can be made and new instruments can be designed with other applications in mind.

7.1 Future instrumentation

The multi-channel VIS-OCT system allows for several detection schemes to be engineered for various purposes. Future instrument development will focus on enhancing the polarization-diverse detection and make better use of the existing platform. Additionally, line illumination has been proposed to construct a true OCM system with high NA and sub-micron lateral resolution that utilizes the full camera frame to acquire a B-scan in a single frame readout.

7.1.1 Dual-input PS-OCT

The dual-input PS-OCT method has been mentioned throughout this manuscript. Little data has been shown largely due to its lack of validation. At current, the processing method has been adapted and incorporates spectral binning to reduce polarization mode dispersion. However, a lack of suitable validation procedures have left the data difficult to interpret and with little reliance. Shown below are a pair of lung samples using the dual-input method. Each sample has good intensity signal contrast but the depth-resolved retardance values lack consistency. There are several possibilities that may contribute to this result. One is that the image between the two orthogonal Stokes input vectors may not be identical. Sample drift, beam deviations, and tissue hydration may all impact the generated image and impede the analysis method.

Further validation studies will be explored and the utility of this measurement will be assessed for performance in lung fibrosis detection. The utility of this measurement must be carefully consider as it doubles the acquisition time due to the multiple input polarizations. Multi-channel detection may be able to improve upon this by illuminating with a second, off-axis beam with an orthogonal Stokes vector. Image registration will need to be addressed but if the signals can be isolated on the detector, simultaneous acquisition can be performed. There are two highly

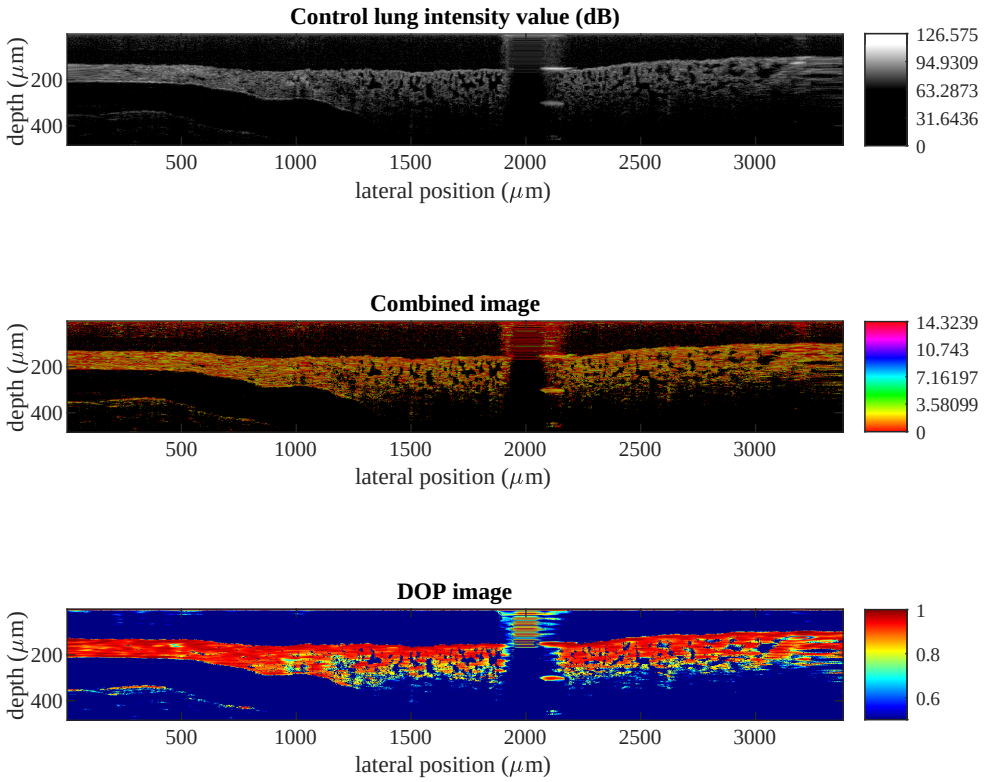

Figure 7.1: Dual-input PS-VIS-OCT imaging of a normal mouse lung at 21 days. Top: PS-VIS-OCT intensity image of a control mouse lung. Middle: Intensity image with per pixel retardance used for color. Bottom: The degree of polarization (DOP) image.

desirable outcomes of this method that add value to pursuing it. First is the application of this method to an endoscope for *in vivo* imaging. Current work by the Bouma group has applied this method in catheter-based imaging of the trachea, which make it an attractive option for imaging the lung airway. The second is that the orthogonal Stokes vector input is capable of measuring the accumulated retardance beyond $\pi/4$ radians (45°), which expands the range of unambiguous tissue measurement. This may be critical as studies move from the mouse to human where the amount of reatardance is not yet known. Minimizing the amount of *a priori* knowledge needed to process data is ideal.

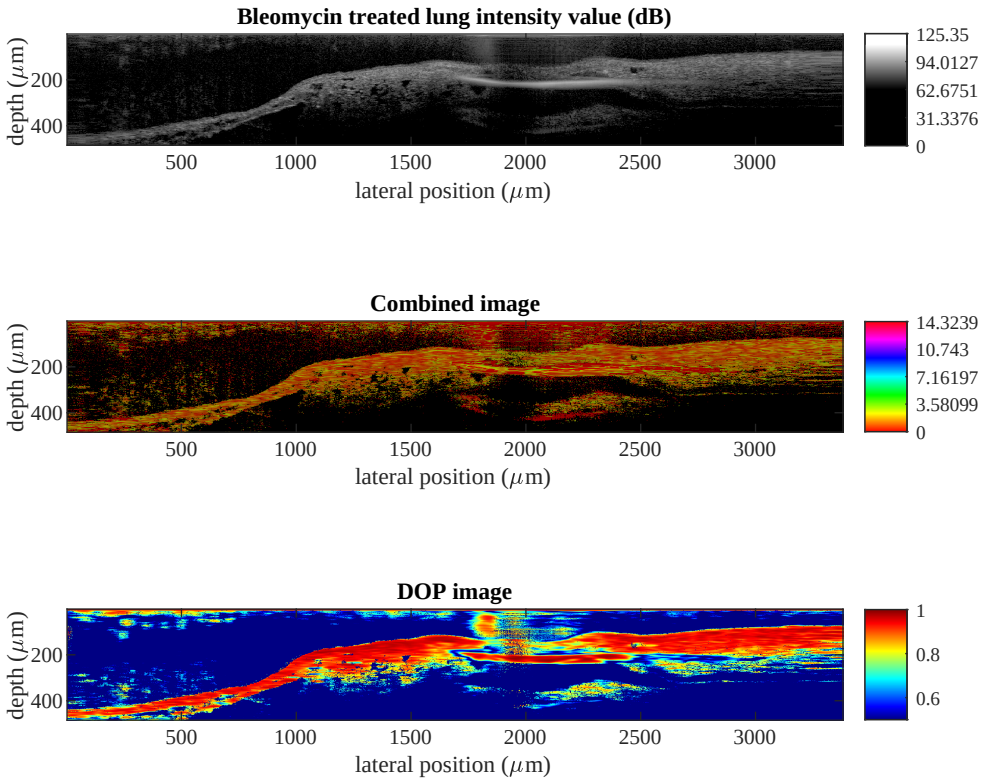

Figure 7.2: Dual-input PS-VIS-OCT imaging of a bleomycin-treated mouse lung at 21 days. Top: PS-VIS-OCT intensity image of a mouse lung treated with bleomycin. Middle: Intensity image with per pixel retardance used for color. Bottom: The degree of polarization (DOP) image.

7.1.2 Spectral

The so-called inverse-spectroscopic OCT (IS-OCT) has been demonstrated previously to be suitable for spectral determination of optical properties. The spectral dependence of tissue optical properties can be leveraged with models to describe tissue ultrastructure. Due to the high bandwidth used in this VIS-OCT instrument, spectral properties can be determined over a broad range of λ with little to no change in the instrument configuration. The maximum bandwidth for the source is the most necessary instrumentation consideration when using this type of processing. As was reviewed in Section 2.5.2, this method relies on windowing the spectral interferogram into bins before the Fourier processing to extract multiple images at a lower axial resolution. It was also mentioned

that this windowing procedure has utility in mitigating polarization mode dispersion and better estimating sample-dependent dispersion.

This analysis method is not exclusive to solving the inverse scattering problem as demonstrated by Yi et al. The dual-input PS-OCT processing makes use of spectral binning to mitigate polarization mode dispersion, which is common in fiber-based OCT systems. In future work, spectral binning can be applied to PS-OCT data to produce a polarization-diverse and wavelength-resolved description of optical scattering. Spectral binning has seen use in both IS-OCT and PS-OCT independently to the knowledge of the author, they have never been used simultaneously, particularly in VIS-OCT imaging.

7.1.3 OCM and Line-field

The intrinsic trade-off of lateral resolution and depth of focus has been a critical design consideration in all systems. The relatively high NA (0.13) of the OCM system provided good resolution but was noted for its low depth of imaging due to the confocal PSF. For applications where only a short depth of imaging is necessary, OCM can be a valuable tool. As the NA increases to achieve sub-micron resolution, the depth of focus reduces exponentially. For a sub-micron lateral resolution, the realistic depth of imaging is on the order of tens of microns.

The current detector for the multi-channel system contains 48 rows of 4096 pixels and current designs disperse the spectrum across the long axis of the camera. The source bandwidth gives approximately a micron of axial resolution. By remounting the camera and far reducing the amount of dispersion, a row of 48 pixels could be used to reconstruct an image with approximately 25 μm of depth, which matches well with OCM. The potential utility of this relies on line-field illumination, where a cylindrical lens is used to produce a line of illuminated pixels with an objective rather than a single point. Effectively, one of the scanning galvo mirros is replaced by this and the full line can be reimaged onto the transmission grating, creating several spectra across the 4096 rows of 48 pixels on the detector. In principle, this design would require minimum modifications and be capable of imaging a full OCM B-scan in one frame read out. The ability to acquire B-scans in high resolution at kHz rates is an attractive option for several studies of cellular dynamics.

7.2 Clinical use for risk stratification

A major motivation in several aspects of this work are the ability of OCT to the clinic. Ophthalmic OCT is an increasingly pervasive tool when imaging the retina. It is convenient due to the optics of the eye being amenable to scanning microscopy tools. In areas outside of the eye, endoscopes and catheters must be used. Several adaptations of OCT exist in this space and typically involve a catheter or endoscope which uses a GRIN lens to focus while rotation and pullback perform the scanning. These tools provide excellent imaging of lumenal spaces within the body but require investment into the distal optics.

An OCT probe with no distal optics has been explored for measuring optical scattering. The light source was coupled into a fiber optic which was cleaved to expose the inner core. Rather than using a reference arm which would need a matching length of optical fiber, the drastic index change between the end of the fiber and the sample was used as the reference, creating a common-path OCT system. The lack of focusing or scanning optics present substantial obstacles in the fiber's use, however, initial data demonstrated the ability of this fiber to measure optical scattering.

Modifying the depth of focus corrections explored earlier for the focus to be at zero and constant divergence, a prediction of the intensity fall-off was generated. Imaging a glass reflection in air while the fiber tip was moved further from the surface generated data that agreed well with this fall-off estimate. Using this correction, optical scattering phantoms and ablated esophageal tissue that had been fixed in paraformaldehyde were imaged and their optical properties were measured. While there is some deviation from the predicted value for the phantoms, the probe was able to measure an increase in optical scattering as sphere concentration increased. Furthermore, the probe was able to measure a difference in optical scattering between the ablated and normal tissue post-fixation.

The spectral binning method mentioned in Section 7.1.2 was applied to the optical scattering data measured by the probe. Spectral dependence of scattering has been a topic of interest in cancer development. By windowing the limited data, some spectral resolution of the properties is achieved by the technique still needs refinement. If successful, it could be a powerful tool in characterizing the progression of disease in epithelial tissue, where many cancers originate.

The utility of this probe is that its imaging depth is sufficient for epithelial cell layers and its cost is low enough for it to be disposable. The intent is for this probe to find use for cancer

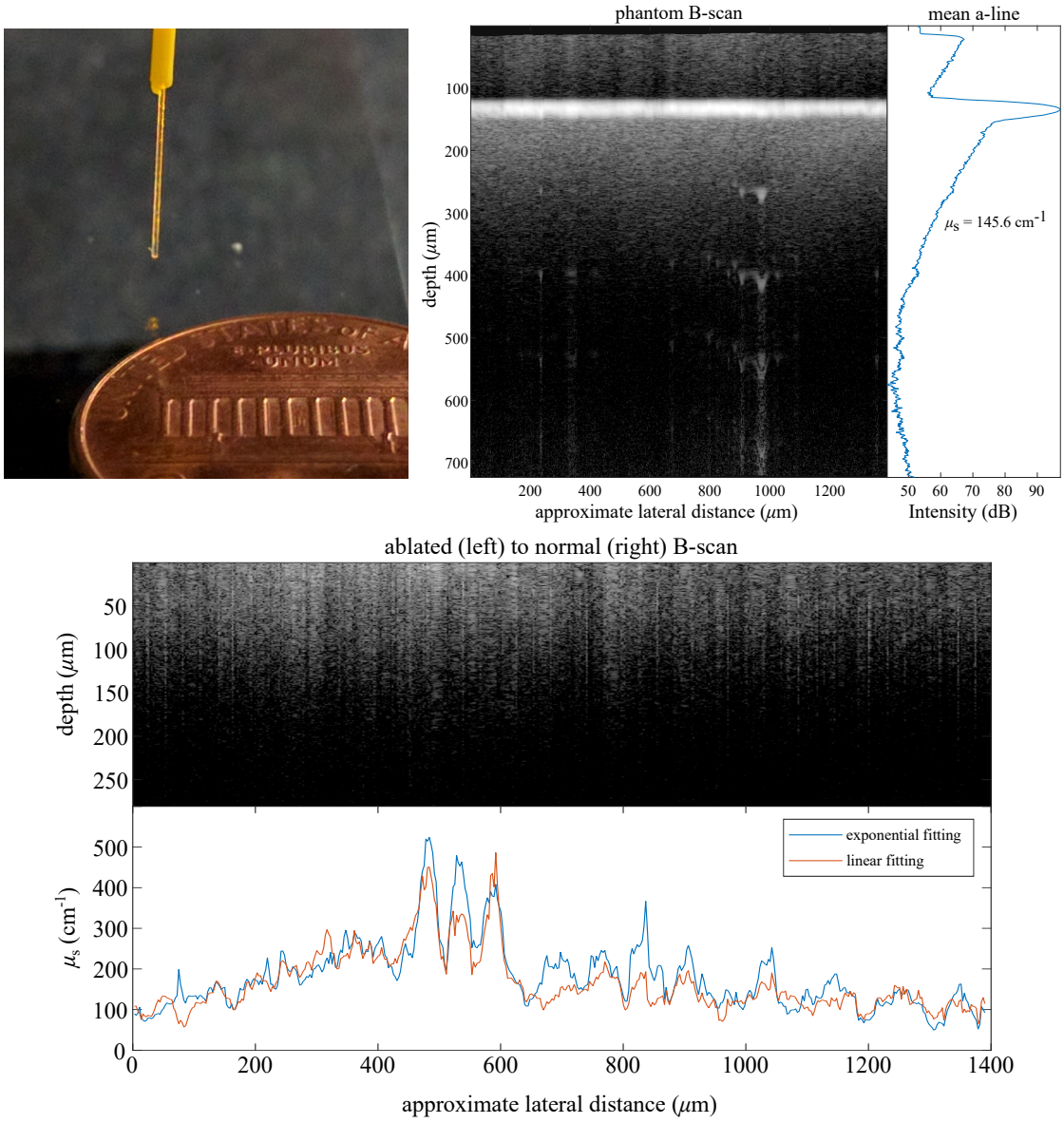

Figure 7.3: Top left: Image of the probe with a standard penny for scale. Top right: Phantom b-scan without contact with the corresponding mean A-line and the measured scattering. Bottom: ablated and normal esophageal tissue after fixation with the measured scattering coefficient for each pixel in the B-scan.

risk stratification. Its greater flexibility and low cost make it suitable for exploring the duodenum and could potentially serve to measure tissue optical scattering distal to the pancreas. Given the scarcity of pancreatic cancer diagnostic metric, any tool that could predict patient risk and classify them for more invasive and expensive screening would be a significant boon to the field.

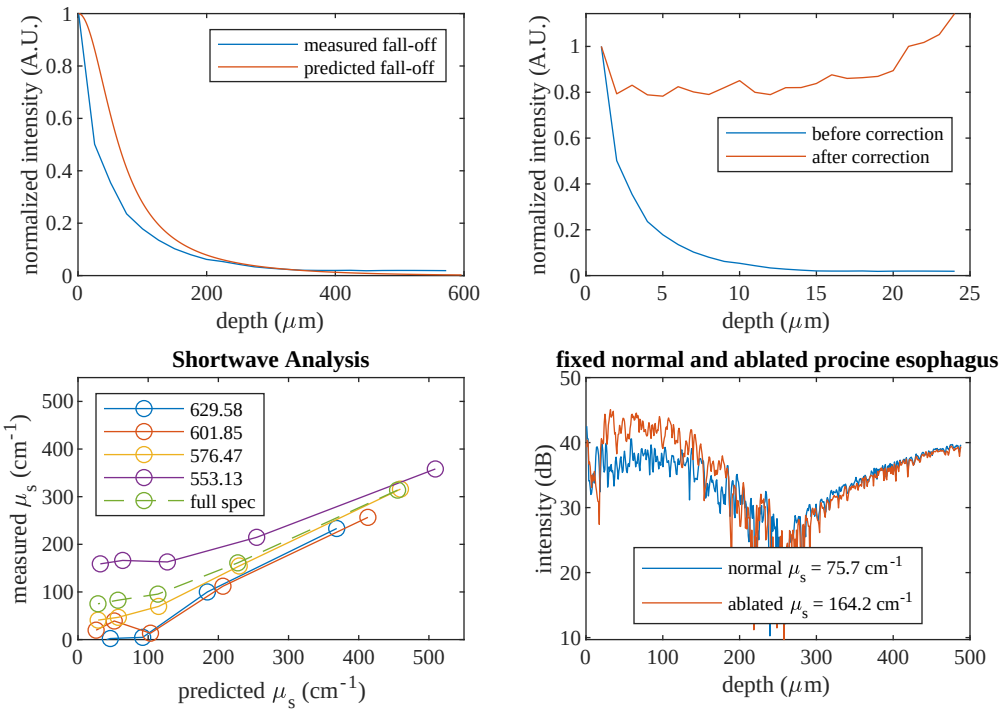

Figure 7.4: Top left: Predicted (blue) and measured (red) fall-off from the probe. Top right: Maximum intensity before (blue) and after (red) correction. Bottom left: Spectral binning and full range fitting of optical properties. Bottom right: Mean intensity profile for normal (blue) and ablated (red) esophageal tissue after fixation.

7.3 Conclusions and Final Remarks

The multi-channel OCT system presented in this dissertation fulfilled several functions and provides a strong basis for a future body of work. The VIS-OCT platform was capable of measuring optical scattering and discriminating ablated esophageal tissue from normal. These capabilities mirrored that of a commercial NIR-OCT system but with superior resolution at the cost of depth of imaging. The implementation of the multi-channel method for reducing noise demonstrated the potential for low-cost, portable supercontinuum sources to approach that of shot noise limited sources. Establishing polarization sensitivity on a single detector and with a single set of optics enabled single and dual-input PS-OCT imaging which was capable of evaluating tissue birefringece. Integration of OCT into a multi-modal system was achieved and co-registered imaging of the eye was performed. The multi-channel imaging tools are high-resolution, broadband, and capable of polarization-diverse detection, making it the ideal base to examine fibrotic disease.

8 Bibliography

References

[1] Bruce Alberts, Alexander Johnson, Julian Lewis, David Morgan, Martin Raff, Keith Roberts, and Peter Walter. *Molecular Biology of the Cell*. Garland Science, Taylor and Francis Group, 6th edition, 2014.

[2] Richard O Hynes. The extracellular matrix: not just pretty fibrils. *Science*, 326(5957):1216–1219, 2009.

[3] Jussi Taipale and Jorma Keski-Oja. Growth factors in the extracellular matrix. *The FASEB Journal*, 11(1):51–59, 1997.

[4] Rudolph L Juliano and S Haskill. Signal transduction from the extracellular matrix. *The Journal of cell biology*, 120(3):577–585, 1993.

[5] Li Sun, Defeng Wang, Xiaotian Li, Lingling Zhang, Hui Zhang, and Yingjie Zhang. Extracellular matrix protein itgbl1 promotes ovarian cancer cell migration and adhesion through wnt/pcp signaling and fak/src pathway. *Biomedicine & Pharmacotherapy*, 81:145–151, 2016.

[6] Theresa A Ulrich, Elena M de Juan Pardo, and Sanjay Kumar. The mechanical rigidity of the extracellular matrix regulates the structure, motility, and proliferation of glioma cells. *Cancer research*, 69(10):4167–4174, 2009.

[7] Charles Streuli. Extracellular matrix remodelling and cellular differentiation. *Current opinion in cell biology*, 11(5):634–640, 1999.

[8] Gwendolen C Reilly and Adam J Engler. Intrinsic extracellular matrix properties regulate stem cell differentiation. *Journal of biomechanics*, 43(1):55–62, 2010.

[9] Boris Hinz. Tissue stiffness, latent tgf-β1 activation, and mechanical signal transduction: implications for the pathogenesis and treatment of fibrosis. *Current rheumatology reports*, 11(2):120, 2009.

[10] Ruchi Malik, Peter I Lelkes, and Edna Cukierman. Biomechanical and biochemical remodeling of stromal extracellular matrix in cancer. *Trends in biotechnology*, 33(4):230–236, 2015.

[11] Craig E Barcus, Patricia J Keely, Kevin W Eliceiri, and Linda A Schuler. Stiff collagen matrices increase tumorigenic prolactin signaling in breast cancer cells. *Journal of Biological Chemistry*, 288(18):12722–12732, 2013.

[12] Harvey Lodish, Arnold Berk, Chris A Kaiser, Monty Krieger, Matthew P Scott, Anthony Bretscher, Hidde Ploegh, Paul Matsudaira, et al. *Molecular cell biology*. Macmillan, 2008.

[13] Matthew D Shoulders and Ronald T Raines. Collagen structure and stability. *Annual review of biochemistry*, 78:929–958, 2009.

[14] Frederick Grinnell. Fibroblast biology in three-dimensional collagen matrices. *Trends in cell biology*, 13(5):264–269, 2003.

[15] Prediman K Shah, Erling Falk, Juan J Badimon, Antonio Fernandez-Ortiz, Alessandra Mailhac, Gerardo Villareal-Levy, John T Fallon, Jan Regnstrom, and Valentin Fuster. Human monocyte-derived macrophages induce collagen breakdown in fibrous caps of atherosclerotic plaques. potential role of matrix-degrading metalloproteinases and implications for plaque rupture. *Circulation*, 92(6):1565–1569, 1995.

[16] Timothy J Koh and Luisa Ann DiPietro. Inflammation and wound healing: the role of the macrophage. *Expert reviews in molecular medicine*, 13, 2011.

[17] Michael Zeisberg, Frank Strutz, and Gerhard A Müller. Role of fibroblast activation in inducing interstitial fibrosis. *Journal of nephrology*, 13:S111, 2000.

[18] Matthew J Scanlan, BK Raj, Benjamin Calvo, Pilar Garin-Chesa, M Pilar Sanz-Moncasi, John H Healey, Lloyd J Old, and Wolfgang J Rettig. Molecular cloning of fibroblast activation protein alpha, a member of the serine protease family selectively expressed in stromal fibroblasts of epithelial cancers. *Proceedings of the National Academy of Sciences*, 91(12):5657–5661, 1994.

[19] Ivan Stamenkovic. Extracellular matrix remodelling: the role of matrix metalloproteinases. *The Journal of Pathology: A Journal of the Pathological Society of Great Britain and Ireland*, 200(4):448–464, 2003.

[20] Matvey E Lukashev and Zena Werb. Ecm signalling: orchestrating cell behaviour and misbehaviour. *Trends in cell biology*, 8(11):437–441, 1998.

[21] Charles H Streuli. Maspin is a tumour suppressor that inhibits breast cancer tumour metastasis in vivo. *Breast Cancer Research*, 4(4):1–4, 2002.

[22] Raghu Kalluri. The biology and function of fibroblasts in cancer. *Nature Reviews Cancer*, 16(9):582, 2016.

[23] GT Thomas, MP Lewis, and PM Speight. Matrix metalloproteinases and oral cancer. *Oral oncology*, 35(3):227–233, 1999.

[24] Paolo Cirri and Paola Chiarugi. Cancer-associated-fibroblasts and tumour cells: a diabolic liaison driving cancer progression. *Cancer and Metastasis Reviews*, 31(1-2):195–208, 2012.

[25] Gavin Tjin, Eric S White, Alen Faiz, Delphine Sicard, Daniel J Tschumperlin, Annabelle Mahar, Eleanor PW Kable, and Janette K Burgess. Lysyl oxidases regulate fibrillar collagen remodelling in idiopathic pulmonary fibrosis. *Disease models & mechanisms*, 10(11):1301–1312, 2017.

[26] Scott McKeown, Alex G Richter, Cecilia O'Kane, Danny F McAuley, and DR Thickett. Mmp expression and abnormal lung permeability are important determinants of outcome in ipf. *European Respiratory Journal*, 33(1):77–84, 2009.

[27] Shaney L Barratt, Andrew Creamer, Conal Hayton, and Nazia Chaudhuri. Idiopathic pulmonary fibrosis (ipf): an overview. *Journal of clinical medicine*, 7(8):201, 2018.

[28] S Bleich, A JŘnemann, N Von Ahsen, B Lausen, K Ritter, G Beck, GOH Naumann, and J Kornhuber. Homocysteine and risk of open-angle glaucoma. *Journal of neural transmission*, 109(12):1499–1504, 2002.

[29] Mark A Prendes, Alon Harris, Barbara M Wirostko, Austin L Gerber, and Brent Siesky. The role of transforming growth factor β in glaucoma and the therapeutic implications. *British Journal of Ophthalmology*, 97(6):680–686, 2013.

[30] Oleg Nadiarnykh, Ronald B LaComb, Molly A Brewer, and Paul J Campagnola. Alterations of the extracellular matrix in ovarian cancer studied by second harmonic generation imaging microscopy. *BMC cancer*, 10(1):94, 2010.

[31] Karissa B Tilbury, James D Hocker, Bruce L Wen, Nathan Sandbo, Vikas Singh, and Paul J Campagnola. Second harmonic generation microscopy analysis of extracellular matrix changes in human idiopathic pulmonary fibrosis. *Journal of biomedical optics*, 19(8):086014, 2014.

[32] Sarah Baldivia, Alexander Levy, Shylaja Hegde, Stijn JA Aper, Maarten Merkx, and Rafael Grytz. A novel organ culture model to quantify collagen remodeling in tree shrew sclera. *PloS one*, 11(11):e0166644, 2016.

[33] Xiyi Chen, Oleg Nadiarynkh, Sergey Plotnikov, and Paul J Campagnola. Second harmonic generation microscopy for quantitative analysis of collagen fibrillar structure. *Nature protocols*, 7(4):654–669, 2012.

[34] David R Rivera, Christopher M Brown, Dimitre G Ouzounov, Ina Pavlova, Demirhan Kobat, Watt W Webb, and Chris Xu. Compact and flexible raster scanning multiphoton endoscope capable of imaging unstained tissue. *Proceedings of the National Academy of Sciences*, 108(43):17598–17603, 2011.

[35] Paolo P Provenzano, David R Inman, Kevin W Eliceiri, Justin G Knittel, Long Yan, Curtis T Rueden, John G White, and Patricia J Keely. Collagen density promotes mammary tumor initiation and progression. *BMC medicine*, 6(1):1–15, 2008.

[36] Paolo P Provenzano, Kevin W Eliceiri, Jay M Campbell, David R Inman, John G White, and Patricia J Keely. Collagen reorganization at the tumor-stromal interface facilitates local invasion. *BMC medicine*, 4(1):1–15, 2006.

[37] Adib Keikhosravi, Jeremy S Bredfeldt, Abdul Kader Sagar, and Kevin W Eliceiri. Second-harmonic generation imaging of cancer. In *Methods in cell biology*, volume 123, pages 531–546. Elsevier, 2014.

[38] Kristin M Riching, Benjamin L Cox, Max R Salick, Carolyn Pehlke, Andrew S Riching, Susan M Ponik, Benjamin R Bass, Wendy C Crone, Yi Jiang, Alissa M Weaver, et al. 3d collagen alignment limits protrusions to enhance breast cancer cell persistence. *Biophysical journal*, 107(11):2546–2558, 2014.

[39] Matthew W Conklin, Jens C Eickhoff, Kristin M Riching, Carolyn A Pehlke, Kevin W Eliceiri, Paolo P Provenzano, Andreas Friedl, and Patricia J Keely. Aligned collagen is a prognostic signature for survival in human breast carcinoma. *The American journal of pathology*, 178(3):1221–1232, 2011.

[40] Yingxin Zhao, Bing Tian, Hong Sun, Jing Zhang, Yueqing Zhang, Maxim Ivannikov, Massoud Motamedi, Zhiqing Liu, Jia Zhou, Lata Kaphalia, et al. Pharmacoproteomics reveal novel protective activity of bromodomain containing 4 inhibitors on vascular homeostasis in tlr3-mediated airway remodeling. *Journal of proteomics*, 205:103415, 2019.

[41] Nathan Sandbo. Mechanisms of fibrosis in ipf. In *Idiopathic Pulmonary Fibrosis*, pages 133–182. Springer, 2019.

[42] M Rosario Hernandez and Hongqing Ye. Glaucoma: changes in extracellular matrix in the optic nerve head. *Annals of medicine*, 25(4):309–315, 1993.

[43] Ivey L Thornton, William J Dupps, Abhijit Sinha Roy, and Ronald R Krueger. Biomechanical effects of intraocular pressure elevation on optic nerve/lamina cribrosa before and after peripapillary scleral collagen cross-linking. *Investigative ophthalmology & visual science*, 50(3):1227–1233, 2009.

[44] Markus H Kuehn, Koren A Lipsett, Marilyn Menotti-Raymond, S Scott Whitmore, Todd E Scheetz, Victor A David, Stephen J O'Brien, Zhongyuan Zhao, Jackie K Jens, Elizabeth M Snella, et al. A mutation in ltbp2 causes congenital glaucoma in domestic cats (felis catus). *PloS one*, 11(5):e0154412, 2016.

[45] Gunnsteinn Hall, Karissa B Tilbury, Kirby R Campbell, Kevin W Eliceiri, and Paul J Campagnola. Experimental and simulation study of the wavelength dependent second harmonic generation of collagen in scattering tissues. *Optics letters*, 39(7):1897–1900, 2014.

[46] Aleksandar Lukic, Sebastian Dochow, Hyeonsoo Bae, Gregor Matz, Ines Latka, Bernhard Messerschmidt, Michael Schmitt, and Jürgen Popp. Endoscopic fiber probe for nonlinear spectroscopic imaging. *Optica*, 4(5):496–501, 2017.

[47] Ronald LaComb, Oleg Nadiarnykh, and Paul J Campagnola. Quantitative second harmonic generation imaging of the diseased state osteogenesis imperfecta: experiment and simulation. *Biophysical journal*, 94(11):4504–4514, 2008.

[48] Dizem Arifler, Ina Pavlova, Ann Gillenwater, and Rebecca Richards-Kortum. Light scattering from collagen fiber networks: micro-optical properties of normal and neoplastic stroma. *Biophysical journal*, 92(9):3260–3274, 2007.

[49] Duncan J Maitland and Joseph T Walsh Jr. Quantitative measurements of linear birefringence during heating of native collagen. *Lasers in Surgery and Medicine: The Official Journal of the American Society for Laser Medicine and Surgery*, 20(3):310–318, 1997.

[50] K Kiraly, MM Hyttinen, T Lapvetelainen, M Elo, I Kiviranta, J Dobai, L Modis, HJ Helminen, and JPA Arokoski. Specimen preparation and quantification of collagen birefringence in unstained sections of articular cartilage using image analysis and polarizing light microscopy. *The Histochemical journal*, 29(4):317–327, 1997.

[51] Craig F Bohren and Donald R Huffman. *Absorption and scattering of light by small particles*. John Wiley & Sons, 2008.

[52] Hendrik Christoffel Hulst and Hendrik C van de Hulst. *Light scattering by small particles*. Courier Corporation, 1981.

[53] Valery V Tuchin et al. Tissue optics. Society of Photo-Optical Instrumentation Engineers (SPIE), 2015.

[54] Lusik Cherkezyan, Yolanda Stypula-Cyrus, Hariharan Subramanian, Craig White, Mart Dela Cruz, Ramesh K Wali, Michael J Goldberg, Laura K Bianchi, Hemant K Roy, and Vadim

Backman. Nanoscale changes in chromatin organization represent the initial steps of tumorigenesis: a transmission electron microscopy study. *BMC cancer*, 14(1):189, 2014.

[55] Jeremy D Rogers, İlker R Çapoğlu, and Vadim Backman. Nonscalar elastic light scattering from continuous random media in the born approximation. *Optics letters*, 34(12):1891–1893, 2009.

[56] Max Born and Emil Wolf. *Principles of optics: electromagnetic theory of propagation, interference and diffraction of light*. Elsevier, 2013.

[57] Johannes F De Boer, Christoph K Hitzenberger, and Yoshiaki Yasuno. Polarization sensitive optical coherence tomography–a review. *Biomedical optics express*, 8(3):1838–1873, 2017.

[58] Adam Wax and Vadim Backman. *Biomedical applications of light scattering*. McGraw Hill Professional, 2009.

[59] Zach J Simmons and Jeremy Rogers. Spatially resolved spectral 4pi optical scattering goniometry and experimental refractive index autocorrelations (conference presentation). In *Optical Interactions with Tissue and Cells XXX*, volume 10876, page 108760G. International Society for Optics and Photonics, 2019.

[60] Z. J. Simmons and J. D. Rogers. Microscope objective based 4π spectroscopic tissue scattering goniometry. *Biomed. Opt. Express*, 8(8):3828–3841, Aug 2017.

[61] Gunnsteinn Hall, Steven L Jacques, Kevin W Eliceiri, and Paul J Campagnola. Goniometric measurements of thick tissue using monte carlo simulations to obtain the single scattering anisotropy coefficient. *Biomedical optics express*, 3(11):2707–2719, 2012.

[62] Steven L Jacques, Bo Wang, and Ravikant Samatham. Reflectance confocal microscopy of optical phantoms. *Biomedical optics express*, 3(6):1162–1172, 2012.

[63] Ravikant V Samatham, Steven L Jacques, and Paul J Campagnola. Optical properties of mutant versus wild-type mouse skin measured by reflectance-mode confocal scanning laser microscopy (rcslm). *Journal of biomedical optics*, 13(4):041309, 2008.

[64] David M Burmeister, Adrien Ponticorvo, Bruce Yang, Sandra C Becerra, Bernard Choi, Anthony J Durkin, and Robert J Christy. Utility of spatial frequency domain imaging (sfdi) and laser speckle imaging (lsi) to non-invasively diagnose burn depth in a porcine model. *Burns*, 41(6):1242–1252, 2015.

[65] Jessie R Weber, Anthony J Durkin, Bruce J Tromberg, David J Cuccia, William R Johnson, Daniel W Wilson, Gregory H Bearman, Mike Hsu, Alexander Lin, and Devin K Binder. Multispectral imaging of tissue absorption and scattering using spatial frequency domain imaging and a computed-tomography imaging spectrometer. *Journal of biomedical optics*, 16(1):011015, 2011.

[66] John W Pickering, Scott A Prahl, Niek Van Wieringen, Johan F Beek, Henricus JCM Sterenborg, and Martin JC Van Gemert. Double-integrating-sphere system for measuring the optical properties of tissue. *Applied optics*, 32(4):399–410, 1993.

[67] Anna N Yaroslavsky, Ilya V Yaroslavsky, Thomas Goldbach, and Hans-Joachim Schwarzmaier. Influence of the scattering phase function approximation on the optical properties of blood determined from the integrating sphere measurements. *Journal of Biomedical Optics*, 4(1):47–54, 1999.

[68] John W Pyhtila and Adam Wax. Rapid, depth-resolved light scattering measurements using fourier domain, angle-resolved low coherence interferometry. *Optics Express*, 12(25):6178–6183, 2004.

[69] John W Pyhtila, Robert N Graf, and Adam Wax. Determining nuclear morphology using an improved angle-resolved low coherence interferometry system. *Optics Express*, 11(25):3473–3484, 2003.

[70] Hemant K Roy, Young L Kim, Yang Liu, Ramesh K Wali, Michael J Goldberg, Vladimir Turzhitsky, Jonathan Horwitz, and Vadim Backman. Risk stratification of colon carcinogenesis through enhanced backscattering spectroscopy analysis of the uninvolved colonic mucosa. *Clinical Cancer Research*, 12(3):961–968, 2006.

[71] Vladimir M Turzhitsky, Andrew J Radosevich, Jeremy D Rogers, Nikhil N Mutyal, and Vadim Backman. Measurement of optical scattering properties with low-coherence enhanced backscattering spectroscopy. *Journal of biomedical optics*, 16(6):067007, 2011.

[72] Joseph A Izatt, Michael R Hee, Gabrielle M Owen, Eric A Swanson, and James G Fujimoto. Optical coherence microscopy in scattering media. *Optics letters*, 19(8):590–592, 1994.

[73] Dirk J Faber, Freek J Van Der Meer, Maurice CG Aalders, and Ton G van Leeuwen. Quantitative measurement of attenuation coefficients of weakly scattering media using optical coherence tomography. *Optics express*, 12(19):4353–4365, 2004.

[74] David Levitz, Lars Thrane, Michael H Frosz, Peter E Andersen, Claus B Andersen, Jurga Valanciunaite, Johannes Swartling, Stefan Andersson-Engels, and Peter R Hansen. Determination of optical scattering properties of highly-scattering media in optical coherence tomography images. *Optics express*, 12(2):249–259, 2004.

[75] Sreyankar Nandy, William Chapman, Rehan Rais, Ivan Gonzalez, Deyali Chatterjee, Matthew Mutch, and Quing Zhu. Label-free quantitative optical assessment of human colon tissue using spatial frequency domain imaging. *Techniques in coloproctology*, 22(8):617–621, 2018.

[76] Jordan A Sweer, Mason T Chen, Kevan J Salimian, Richard J Battafarano, and Nicholas J Durr. Wide-field optical property mapping and structured light imaging of the esophagus with spatial frequency domain imaging. *Journal of biophotonics*, 12(9):e201900005, 2019.

[77] John W Pyhtila, Kevin J Chalut, Jeffrey D Boyer, Justin Keener, Thomas D'Amico, Marcia Gottfried, Frank Gress, and Adam Wax. In situ detection of nuclear atypia in barrett's esophagus by using angle-resolved low-coherence interferometry. *Gastrointestinal Endoscopy*, 65(3):487–491, 2007.

[78] Andrew J Radosevich, Nikhil N Mutyal, Ji Yi, Yolanda Stypula-Cyrus, Jeremy D Rogers, Michael J Goldberg, Laura Bianchi, Shailesh Bajaj, and Hemant K Roy. Ultrastructural alterations in field carcinogenesis measured by enhanced backscattering spectroscopy. *Journal of biomedical optics*, 18(9):097002, 2013.

[79] David Huang, Eric A Swanson, Charles P Lin, Joel S Schuman, William G Stinson, Warren Chang, Michael R Hee, Thomas Flotte, Kenton Gregory, Carmen A Puliafito, et al. Optical coherence tomography. *science*, 254(5035):1178–1181, 1991.

[80] Adolph F Fercher, Ch K Hitzenberger, G Kamp, and Sy Y El-Zaiat. Measurement of intraocular distances by backscattering spectral interferometry. *Optics communications*, 117(1-2):43–48, 1995.

[81] Maciej Wojtkowski, Rainer Leitgeb, Andrzej Kowalczyk, Tomasz Bajraszewski, and Adolf F Fercher. In vivo human retinal imaging by fourier domain optical coherence tomography. *Journal of Biomedical Optics*, 7(3):457 – 463, 2002.

[82] James Fujimoto and Eric Swanson. The development, commercialization, and impact of optical coherence tomography. *Investigative Ophthalmology & Visual Science*, 57(9):OCT1–OCT13, 07 2016.

[83] Wolfgang Drexler and James Fujimoto. *Optical Coherence Tomography: Technology and Applications*. 01 2008.

[84] Joseph Izatt and Michael Choma. *Theory of Optical Coherence Tomography*, pages 47–72. 01 2008.

[85] Adolf Friedrich Fercher. Optical coherence tomography – development, principles, applications. *Zeitschrift für Medizinische Physik*, 20(4):251 – 276, 2010.

[86] Gennifer T Smith, Nicholas Dwork, Daniel O'Connor, Uzair Sikora, Kristen L Lurie, John M Pauly, and Audrey K Ellerbee. Automated, depth-resolved estimation of the attenuation coefficient from optical coherence tomography data. *IEEE transactions on medical imaging*, 34(12):2592–2602, 2015.

[87] KA Vermeer, J Mo, JJA Weda, HG Lemij, and JF De Boer. Depth-resolved model-based reconstruction of attenuation coefficients in optical coherence tomography. *Biomedical optics express*, 5(1):322–337, 2014.

[88] Ji Yi, Andrew J Radosevich, Jeremy D Rogers, Sam CP Norris, İlker R Çapoğlu, Allen Taflove, and Vadim Backman. Can oct be sensitive to nanoscale structural alterations in biological tissue? *Optics express*, 21(7):9043–9059, 2013.

[89] David C Adams, Lida P Hariri, Alyssa J Miller, Yan Wang, Josalyn L Cho, Martin Villiger, Jasmin A Holz, Margit V Szabari, Daniel L Hamilos, R Scott Harris, et al. Birefringence microscopy platform for assessing airway smooth muscle structure and function in vivo. *Science translational medicine*, 8(359):359ra131–359ra131, 2016.

[90] Shuichi Makita, Masahiro Yamanari, and Yoshiaki Yasuno. Generalized jones matrix optical coherence tomography: performance and local birefringence imaging. *Optics express*, 18(2):854–876, 2010.

[91] Christoph K Hitzenberger, Erich Götzinger, Markus Sticker, Michael Pircher, and Adolf F Fercher. Measurement and imaging of birefringence and optic axis orientation by phase resolved polarization sensitive optical coherence tomography. *Optics express*, 9(13):780–790, 2001.

[92] Erich Götzinger, Michael Pircher, and Christoph K Hitzenberger. High speed spectral domain polarization sensitive optical coherence tomography of the human retina. *Optics express*, 13(25):10217–10229, 2005.

[93] Michael R Hee, David Huang, Eric A Swanson, and James G Fujimoto. Polarization-sensitive low-coherence reflectometer for birefringence characterization and ranging. *JOSA B*, 9(6):903–908, 1992.

[94] Rebecca Richards-Kortum and Eva Sevick-Muraca. Quantitative optical spectroscopy for tissue diagnosis. *Annual review of physical chemistry*, 47(1):555–606, 1996.

[95] Martin Villiger, Ellen Ziyi Zhang, Seemantini K Nadkarni, Wang-Yuhl Oh, Benjamin J Vakoc, and Brett E Bouma. Spectral binning for mitigation of polarization mode dispersion artifacts in catheter-based optical frequency domain imaging. *Optics express*, 21(14):16353–16369, 2013.

[96] Maciej Wojtkowski, Vivek J Srinivasan, Tony H Ko, James G Fujimoto, Andrzej Kowalczyk, and Jay S Duker. Ultrahigh-resolution, high-speed, fourier domain optical coherence tomography and methods for dispersion compensation. *Optics express*, 12(11):2404–2422, 2004.

[97] Adolf F Fercher, Christoph K Hitzenberger, Markus Sticker, Robert Zawadzki, Boris Karamata, and Theo Lasser. Numerical dispersion compensation for partial coherence interferometry and optical coherence tomography. *Optics express*, 9(12):610–615, 2001.

[98] Ryan C Niemeier, Zach J Simmons, and Jeremy D Rogers. Noise reduction in supercontinuum sources for oct by single-pulse spectral normalization. *Applied Optics*, 59(18):5521–5526, 2020.

[99] Xiao Shu, Lisa Jane Beckmann, and Hao F Zhang. Visible-light optical coherence tomography: a review. *Journal of biomedical optics*, 22(12):121707, 2017.

[100] Maciej Szkulmowski, Maciej Wojtkowski, Tomasz Bajraszewski, Iwona Gorczyńska, Piotr Targowski, Wojciech Wasilewski, Andrzej Kowalczyk, and Czesław Radzewicz. Quality improvement for high resolution in vivo images by spectral domain optical coherence tomography with supercontinuum source. *Optics Communications*, 246(4-6):569–578, 2005.

[101] William J Brown, Sanghoon Kim, and Adam Wax. Noise characterization of supercontinuum sources for low-coherence interferometry applications. *Journal of the Optical Society of America. A, Optics, image science, and vision*, 31(12):2703–10, dec 2014.

[102] Mikkel Jensen, Iván Bravo Gonzalo, Rasmus Dybbro Engelsholm, Michael Maria, Niels Møller Israelsen, Adrian Podoleanu, and Ole Bang. Noise of supercontinuum sources in spectral domain optical coherence tomography. *JOSA B*, 36(2):A154–A160, 2019.

[103] John M Dudley, Goëry Genty, and Stéphane Coen. Supercontinuum generation in photonic crystal fiber. *Reviews of modern physics*, 78(4):1135, 2006.

[104] J. M. Dudley, S. Coen, K. L. Corwin, N. R. Newbury, B. R. Washburn, S. A. Diddams, and R. S. Windeier. Fundamental noise limitations on supercontinuum generation in microstructure fiber. *2003 European Quantum Electronics Conference, EQEC 2003*, (March):203, 2003.

[105] U. Møller, S. T. Sørensen, C. Jakobsen, J. Johansen, P. M. Moselund, C. L. Thomsen, and O. Bang. Power dependence of supercontinuum noise in uniform and tapered PCFs. *Optics Express*, 20(3):2851, 2012.

[106] Sunghwan Shin, Utkarsh Sharma, Haohua Tu, Woonggyu Jung, and Stephen A Boppart. Characterization and analysis of relative intensity noise in broadband optical sources for optical coherence tomography. *IEEE Photonics Technology Letters*, 22(14):1057–1059, 2010.

[107] Tilman Schmoll, Erich Götzinger, Michael Pircher, Christoph K Hitzenberger, and Rainer A Leitgeb. Single-camera polarization-sensitive spectral-domain oct by spatial frequency encoding. *Optics letters*, 35(2):241–243, 2010.

[108] Michael Pircher, Erich Götzinger, Rainer A Leitgeb, Adolf Friedrich Fercher, and Christoph K Hitzenberger. Speckle reduction in optical coherence tomography by frequency compounding. *Journal of biomedical optics*, 8(3):565–570, 2003.

[109] Joseph M Schmitt, SH Xiang, and Kin Man Yung. Speckle in optical coherence tomography: an overview. In *Saratov Fall Meeting'98: Light Scattering Technologies for Mechanics, Biomedicine, and Material Science*, volume 3726, pages 450–461. International Society for Optics and Photonics, 1999.

[110] Michael Pircher, Christoph K Hitzenberger, and Ursula Schmidt-Erfurth. Polarization sensitive optical coherence tomography in the human eye. *Progress in retinal and eye research*, 30(6):431–451, 2011.

[111] Nate J Kemp, Jesung Park, Haitham N Zaatari, H Grady Rylander, and Thomas E Milner. High-sensitivity determination of birefringence in turbid media with enhanced polarization-sensitive optical coherence tomography. *JOSA A*, 22(3):552–560, 2005.

[112] Ellen Ziyi Zhang, Wang-Yuhl Oh, Martin L Villiger, Liang Chen, Brett E Bouma, and Benjamin J Vakoc. Numerical compensation of system polarization mode dispersion in polarization-sensitive optical coherence tomography. *Optics Express*, 21(1):1163–1180, 2013.

[113] Martin Villiger, Boy Braaf, Norman Lippok, Kenichiro Otsuka, Seemantini K Nadkarni, and Brett E Bouma. Optic axis mapping with catheter-based polarization-sensitive optical coherence tomography. *Optica*, 5(10):1329–1337, 2018.

[114] Seemantini K Nadkarni, Mark C Pierce, B Hyle Park, Johannes F de Boer, Peter Whittaker, Brett E Bouma, Jason E Bressner, Elkan Halpern, Stuart L Houser, and Guillermo J Tearney. Measurement of collagen and smooth muscle cell content in atherosclerotic plaques using polarization-sensitive optical coherence tomography. *Journal of the American College of Cardiology*, 49(13):1474–1481, 2007.

[115] Ryan C Niemeier, Sevde Etoz, Daniel A Gil, Melissa C Skala, Christopher L Brace, and Jeremy D Rogers. Quantifying optical properties with visible and near-infrared optical coherence tomography to visualize esophageal microwave ablation zones. *Biomedical optics express*, 9(4):1648–1663, 2018.

[116] R Niemeier and JD Rogers. Low-cost reflective hilger–chance refractometer used to determine sellmeier coefficients of bulk polydimethylsiloxane. *Applied optics*, 58(22):6152–6156, 2019.

[117] Christopher L Brace. Radiofrequency and microwave ablation of the liver, lung, kidney, and bone: what are the differences? *Current problems in diagnostic radiology*, 38(3):135–143, 2009.

[118] Stephen A Boppart, Juergen Herrmann, Costas Pitris, Debra L Stamper, Mark E Brezinski, and James G Fujimoto. High-resolution optical coherence tomography-guided laser ablation of surgical tissue. *Journal of Surgical Research*, 82(2):275–284, 1999.

[119] Chao Zhou, Tsung-Han Tsai, Hsiang-Chieh Lee, Tejas Kirtane, Marisa Figueiredo, Yuankai K Tao, Osman O Ahsen, Desmond C Adler, Joseph M Schmitt, Qin Huang, et al. Characterization of buried glands before and after radiofrequency ablation by using 3-dimensional optical coherence tomography (with videos). *Gastrointestinal endoscopy*, 76(1):32–40, 2012.

[120] Anne-Fré Swager, David F Boerwinkel, Daniel M de Bruin, Dirk J Faber, Ton G van Leeuwen, Bas L Weusten, Sybren L Meijer, Jacques J Bergman, and Wouter L Curvers. Detection of

buried barrett's glands after radiofrequency ablation with volumetric laser endomicroscopy. *Gastrointestinal endoscopy*, 83(1):80–88, 2016.

[121] Mohamad A Eloubeidi, Andrew C Mason, Renee A Desmond, and Hashem B El-Serag. Temporal trends (1973–1997) in survival of patients with esophageal adenocarcinoma in the united states: a glimmer of hope? *The American journal of gastroenterology*, 98(7):1627–1633, 2003.

[122] Jan Martínek, Jun-ichi Akiyama, Zuzana Vacková, Manuele Furnari, Edoardo Savarino, Teus J Weijs, Elen Valitova, Sylvia van der Horst, Jelle P Ruurda, Lucas Goense, et al. Current treatment options for esophageal diseases. *Annals of the New York Academy of Sciences*, 1381(1):139–151, 2016.

[123] Kamar Belghazi, Ilaria Cipollone, Jacques JGHM Bergman, and Roos E Pouw. Current controversies in radiofrequency ablation therapy for barrett's esophagus. *Current Treatment Options in Gastroenterology*, 14(1):1–18, 2016.

[124] Rebecca Tuttle, Steven J Nurkin, and Steven N Hochwald. Ablative therapy for esophageal dysplasia and early malignancy: focus on rfa. *BioMed research international*, 2014, 2014.

[125] BJ Dunkin, J Martinez, PA Bejarano, CD Smith, K Chang, AS Livingstone, and WS Melvin. Thin-layer ablation of human esophageal epithelium using a bipolar radiofrequency balloon device. *Surgical Endoscopy and Other Interventional Techniques*, 20(1):125–130, 2006.

[126] Robert A Ganz, David S Utley, Roger A Stern, Jerome Jackson, Kenneth P Batts, and Paul Termin. Complete ablation of esophageal epithelium with a balloon-based bipolar electrode: a phased evaluation in the porcine and in the human esophagus. *Gastrointestinal endoscopy*, 60(6):1002–1010, 2004.

[127] Chris Hancock, Nuwan Dharmasiri, Christopher I Duff, and Malcolm White. New microwave antenna structures for treating gastro-oesophageal reflux disease (gerd). *IEEE transactions on microwave theory and techniques*, 61(5):2242–2252, 2013.

[128] Robert M Eisele. Advances in local ablation of malignant liver lesions. *World journal of gastroenterology*, 22(15):3885, 2016.

[129] Matthew W Stier, Vani J Konda, John Hart, and Irving Waxman. Post-ablation surveillance in barrett's esophagus: A review of the literature. *World journal of gastroenterology*, 22(17):4297, 2016.

[130] Ananya Das, Michael V Sivak Jr, Amitabh Chak, Richard CK Wong, Volker Westphal, Andrew M Rollins, Joseph Willis, Gerard Isenberg, and Joseph A Izatt. High-resolution endoscopic imaging of the gi tract: a comparative study of optical coherence tomography versus high-frequency catheter probe eus. *Gastrointestinal endoscopy*, 54(2):219–224, 2001.

[131] Theresa Lye, Kevin Vincent, Andrew McCulloch, and Christine P Hendon. Normal and radiofrequency ablated atrial models enabled by optical coherence tomography tissue characterization. In *Optical Tomography and Spectroscopy*, pages OTh2B–3. Optical Society of America, 2016.

[132] Soo-Young Park, Rajinder P Singh-Moon, and Christine Hendon. Real-time single fiber based multispectral monitoring of cardiac ablation therapy. In *Optical Tomography and Spectroscopy*, pages SM2D–5. Optical Society of America, 2020.

[133] Stavros G Demos and Shiva Sharareh. Real time assessment of rf cardiac tissue ablation with optical spectroscopy. *Optics express*, 16(19):15286–15296, 2008.

[134] Johannes Swartling, Sara Pålsson, Pyotr Platonov, SB Olsson, and Stefan Andersson-Engels. Changes in tissue optical properties due to radio-frequency ablation of myocardium. *Medical and Biological Engineering and Computing*, 41(4):403–409, 2003.

[135] Jennifer K Barton. Dynamic changes in optical properties. In *Optical-Thermal Response of Laser-Irradiated Tissue*, pages 321–349. Springer, 2010.

[136] DN Wheatley, C Kerr, and DW Gregory. Heat-induced damage to hela-s3 cells: correlation of viability, permeability, osmosensitivity, phase-contrast light-, scanning electron-and transmission electron-microscopical findings. *International journal of hyperthermia*, 5(2):145–162, 1989.

[137] Mehrdad Nikfarjam, Vijayaragavan Muralidharan, and Christopher Christophi. Mechanisms of focal heat destruction of liver tumors. *Journal of Surgical Research*, 127(2):208–223, 2005.

[138] Michael S Wall, Xiang-Hua Deng, Peter A Torzilli, Stephen B Doty, Stephen J O'Brien, and Russell F Warren. Thermal modification of collagen. *Journal of Shoulder and Elbow Surgery*, 8(4):339–344, 1999.

[139] Graham LC Spicer, Samira M Azarin, Ji Yi, Scott T Young, Ronald Ellis, Greta M Bauer, Lonnie D Shea, and Vadim Backman. Detection of extracellular matrix modification in cancer models with inverse spectroscopic optical coherence tomography. *Physics in Medicine & Biology*, 61(19):6892, 2016.

[140] Weston A Welge and Jennifer K Barton. Optical coherence tomography imaging of colonic crypts in a mouse model of colorectal cancer. In *Endoscopic Microscopy XI; and Optical Techniques in Pulmonary Medicine III*, volume 9691, page 96910V. International Society for Optics and Photonics, 2016.

[141] Hsiang-Chieh Lee, Osman O Ahsen, Jonathan J Liu, Tsung-Han Tsai, Qin Huang, Hiroshi Mashimo, and James G Fujimoto. Assessment of the radiofrequency ablation dynamics of esophageal tissue with optical coherence tomography. *Journal of biomedical optics*, 22(7):076001, 2017.

[142] Darian S James, Alexander N Jambor, Hsin-Yu Chang, Zachary Alden, Karissa B Tilbury, Nathan K Sandbo, and Paul J Campagnola. Probing ecm remodeling in idiopathic pulmonary fibrosis via second harmonic generation microscopy analysis of macro/supramolecular collagen structure. *Journal of biomedical optics*, 25(1):014505, 2019.

[143] Darian S James, Hsin-Yu Belle Chang, Nathan K Sandbo, Vikas Singh, and Paul J Campagnola. Understanding ecm remodeling in idiopathic pulmonary fibrosis via polarization resolved shg microscopy. In *Novel Techniques in Microscopy*, pages NW1C–4. Optical Society of America, 2019.

[144] Michael A Pinkert, Zachary J Simmons, Ryan C Niemeier, Bing Dai, Lauren B Woods, Timothy J Hall, Paul J Campagnola, Jeremy D Rogers, and Kevin W Eliceiri. Platform for quantitative multiscale imaging of tissue composition. *Biomedical Optics Express*, 11(4):1927–1946, 2020.

[145] Li Su, Li Huang, Yupeng Xu, Cheng Zhang, and Zhengyu Song. Quantitative analysis of collagen produced by rabbit keratocytes using second harmonic generation microscopy. *Current eye research*, 42(2):195–200, 2017.

[146] Sebina Shrestha, Michael J Serafino, Jesus Rico-Jimenez, Jesung Park, Xi Chen, Siqin Zhaorigetu, Brian L Walton, Javier A Jo, and Brian E Applegate. Multimodal optical coherence tomography and fluorescence lifetime imaging with interleaved excitation sources for simultaneous endogenous and exogenous fluorescence. *Biomedical optics express*, 7(9):3184–3197, 2016.

[147] Shuai Yuan, Michael Lai, Celeste A Roney, James Jiang, Qian Li, Hongzhou Ma, Alex Cable, Ronald M Summers, and Yu Chen. Combining optical coherence tomography with fluorescence molecular imaging: towards simultaneous morphology and molecular imaging. In *Advanced Biomedical and Clinical Diagnostic Systems VII*, volume 7169, page 71690O. International Society for Optics and Photonics, 2009.

[148] Claudio Vinegoni, Jeremy S Bredfeldt, Daniel L Marks, and Stephen A Boppart. Nonlinear optical contrast enhancement for optical coherence tomography. *Optics express*, 12(2):331–341, 2004.

[149] Brian E Applegate, Changhuei Yang, Andrew M Rollins, and Joseph A Izatt. Polarization-resolved second-harmonic-generation optical coherence tomography in collagen. *Optics letters*, 29(19):2252–2254, 2004.

[150] Yi Jiang, Ivan Tomov, Yimin Wang, and Zhongping Chen. Second-harmonic optical coherence tomography. *Optics letters*, 29(10):1090–1092, 2004.

[151] Marinko V Sarunic, Brian E Applegate, and Joseph A Izatt. Spectral domain second-harmonic optical coherence tomography. *Optics letters*, 30(18):2391–2393, 2005.

[152] Siavash Yazdanfar, Lily H Laiho, and Peter TC So. Interferometric second harmonic generation microscopy. *Optics express*, 12(12):2739–2745, 2004.

[153] Andrei B Vakhtin, Daniel J Kane, William R Wood, and Kristen A Peterson. Common-path interferometer for frequency-domain optical coherence tomography. *Applied optics*, 42(34):6953–6958, 2003.

[154] Joseph M Schmitt, A Knuttel, M Yadlowsky, and MA Eckhaus. Optical-coherence tomography of a dense tissue: statistics of attenuation and backscattering. *Physics in Medicine & Biology*, 39(10):1705, 1994.

[155] Magali Estribeau and Pierre Magnan. Fast mtf measurement of cmos imagers using iso 12333 slanted-edge methodology. In *Detectors and Associated Signal Processing*, volume 5251, pages 243–252. International Society for Optics and Photonics, 2004.

[156] I Hartl, XD Li, C Chudoba, RK Ghanta, TH Ko, JG Fujimoto, JK Ranka, and RS Windeler. Ultrahigh-resolution optical coherence tomography using continuum generation in an air–silica microstructure optical fiber. *Optics letters*, 26(9):608–610, 2001.

[157] Seok-Hyun Yun, Guillermo J Tearney, Johannes F de Boer, N Iftimia, and Brett E Bouma. High-speed optical frequency-domain imaging. *Optics express*, 11(22):2953–2963, 2003.

[158] Karen M Joos and Jin-Hui Shen. Miniature real-time intraoperative forward-imaging optical coherence tomography probe. *Biomedical optics express*, 4(8):1342–1350, 2013.

[159] Meng Han, Günter Giese, and Josef F Bille. Second harmonic generation imaging of collagen fibrils in cornea and sclera. *Optics express*, 13(15):5791–5797, 2005.

[160] Frederic L Lizzi, William J Burt, and D Jackson Coleman. Effects of ocular structures on propagation of ultrasound in the eye. *Archives of ophthalmology*, 84(5):635–640, 1970.

[161] Cheri X Deng, Frederic L Lizzi, Ronald H Silverman, Roxana Ursea, and D Jackson Coleman. Imaging and spectrum analysis of contrast agents in the in vivo rabbit eye using very-high–frequency ultrasound. *Ultrasound in medicine & biology*, 24(3):383–394, 1998.

[162] Jonathan Mamou, Christianne A Wa, Kenneth MP Yee, Ronald H Silverman, Jeffrey A Ketterling, Alfredo A Sadun, and J Sebag. Ultrasound-based quantification of vitreous floaters correlates with contrast sensitivity and quality of life. *Investigative Ophthalmology & Visual Science*, 56(3):1611–1617, 2015.

[163] Ronald H Silverman, Robert Folberg, H Culver Boldt, Harriet O Lloyd, Mark J Rondeau, Mary G Mehaffey, Frederic L Lizzi, and D Jackson Coleman. Correlation of ultrasound parameter imaging with microcirculatory patterns in uveal melanomas. *Ultrasound in medicine & biology*, 23(4):573–581, 1997.

[164] MF Insana and TJ Hall. Characterising the microstructure of random media using ultrasound. *Physics in Medicine & Biology*, 35(10):1373, 1990.

[165] Ivan M Rosado-Mendez, Lindsey C Drehfal, James A Zagzebski, and Timothy J Hall. Analysis of coherent and diffuse scattering using a reference phantom. *IEEE transactions on ultrasonics, ferroelectrics, and frequency control*, 63(9):1306–1320, 2016.

[166] Quinton W Guerrero, Ivan M Rosado-Mendez, Lindsey C Drehfal, Helen Feltovich, and Timothy J Hall. Quantifying backscatter anisotropy using the reference phantom method. *IEEE transactions on ultrasonics, ferroelectrics, and frequency control*, 64(7):1063–1077, 2017.

[167] Xianjin Dai, Lei Xi, Can Duan, Hao Yang, Huikai Xie, and Huabei Jiang. Miniature probe integrating optical-resolution photoacoustic microscopy, optical coherence tomography, and ultrasound imaging: proof-of-concept. *Optics letters*, 40(12):2921–2924, 2015.

[168] Yan Li, Joseph Jing, Yueqiao Qu, Yusi Miao, Buyun Zhang, Teng Ma, Mingyue Yu, Qifa Zhou, and Zhongping Chen. Fully integrated optical coherence tomography, ultrasound, and indocyanine green-based fluorescence tri-modality system for intravascular imaging. *Biomedical optics express*, 8(2):1036–1044, 2017.

[169] Maxime Abran, Barbara E Stähli, Nolwenn Merlet, Teodora Mihalache-Avram, Mélanie Mecteau, Eric Rhéaume, David Busseuil, Jean-Claude Tardif, and Frédéric Lesage. Validating a bimodal intravascular ultrasound (ivus) and near-infrared fluorescence (nirf) catheter for atherosclerotic plaque detection in rabbits. *Biomedical optics express*, 6(10):3989–3999, 2015.

[170] Christian Mätzler. Matlab functions for mie scattering and absorption, version 2. *IAP Res. Rep*, 8(1):9, 2002.

[171] Vadim Backman and Hemant K Roy. Advances in biophotonics detection of field carcinogenesis for colon cancer risk stratification. *Journal of Cancer*, 4(3):251, 2013.